TECHNICAL UNIVERSITY OF CRETE
SCHOOL OF ELECTRICAL AND COMPUTER ENGINEERING

Diploma Thesis

«Energy Management System of Vehicles for Space Missions»

Nikolaos Kontonikolis

THESIS COMMITTEE

Professor Koutroulis Eftychios (Supervisor)

Associate Professor Gyftakis Konstantinos

Professor Oungrinis Konstantinos – Alketas

Chania, January 2025

Acknowledgements

I would like to extend my heartfelt gratitude to my family—my parents and dear sister—whose constant support and encouragement have been instrumental in my journey. Their unwavering belief in my ambitions, trust in my capabilities, and motivation to pursue my goals have empowered me to aspire to the highest standards.

I am deeply grateful to Professor Eftychios Koutroulis for his guidance, openness, and willingness to embark on this thesis journey with me. He believed in the project's potential and supported me every step of the way. His ability to keep my ideas grounded in practical and realistic terms pushed me to achieve the best possible outcomes, making his mentorship invaluable throughout this process.

Special thanks to Professor Konstantinos-Alketas Oungrinis for his early belief in this project. His enthusiasm and encouragement inspired me to trust in my boldest ideas and to recognize that there are truly no limits in science and space exploration.

To Professor Konstantinos Gyftakis, I extend my sincere appreciation for his unwavering dedication to his students. His passion for sharing knowledge and expertise has had a significant impact on my academic journey, inspiring me to grow and excel.

This thesis represents the culmination of my dedication, commitment, and persistent effort in applying my expertise in electrical engineering to the field of space applications. It embodies my deep curiosity for exploring uncharted territories and my continuous drive to seek innovation and advance knowledge.

“Earth is the cradle of humanity, but one cannot live in a cradle forever.”

Konstantin Tsiolkovsky

Περίληψη

Η εξερεύνηση του νότιου πόλου της Σελήνης έχει αναδειχθεί ως προτεραιότητα για διαστημικές υπηρεσίες και ιδιωτικούς φορείς παγκοσμίως, καθοδηγούμενη από την ανάγκη για εγκαθίδρυση μιας βιώσιμης ανθρώπινης παρουσίας στη Σελήνη. Ένα κρίσιμο στοιχείο αυτής της προσπάθειας είναι η αποτελεσματική αξιοποίηση των σεληνιακών πόρων, ιδιαίτερα των πτητικών υλικών και του νερού, τα οποία μπορούν να υποστηρίξουν την παραγωγή καυσίμων καθώς και οξυγόνου. Οι μόνιμα σκιασμένες περιοχές (PSRs), γνωστές για τις εξαιρετικά χαμηλές θερμοκρασίες τους, είναι τοποθεσίες με πιθανώς υψηλή συγκέντρωση πτητικών υλικών και χρήζουν περεταίρω εξερεύνησης και μελέτης με τη χρήση ρομποτικών οχημάτων (rovers). Ωστόσο, αυτές οι περιοχές παρουσιάζουν σημαντικές λειτουργικές προκλήσεις λόγω της έλλειψης ηλιοφάνειας και των ακραίων περιβαλλοντικών συνθηκών. Τα συμβατικά συστήματα που περιλαμβάνουν φωτοβολταϊκές διατάξεις και μπαταρίες συχνά δεν επαρκούν, απαιτώντας δυσανάλογα μεγέθη μπαταριών ή συχνές διακοπές της αποστολής για επαναφόρτιση, ενώ τα συστήματα που βασίζονται σε ραδιοϊσότοπα ενέχουν περιβαλλοντικούς και τεχνικούς κινδύνους. Στη παρούσα διπλωματική εργασία αναπτύχθηκε το SELAS (Solar Energy Lightweight Adjustable Station), ένα rover που λειτουργεί σαν κινητός φορτιστής αξιοποιώντας την ηλιακή ενέργεια περιοχών του νότιου πόλου της Σελήνης με υψηλή ηλιοφάνεια για να επαναφορτίσει rovers που βρίσκονται στις μόνιμα σκιασμένες περιοχές. Για την βέλτιστη λειτουργία του SELAS αναπτύχθηκε ένα προηγμένο σύστημα διαχείρισης ενέργειας (EMS) ενώ η αρχιτεκτονική του έχει βελτιστοποιηθεί με τη χρήση του αλγορίθμου σμήνους σωματιδίων (PSO), μειώνοντας τη συνολική μάζα του συστήματος. Η σχεδίαση του SELAS υιοθετεί μια ρεαλιστική προσέγγιση χρησιμοποιώντας αποκλειστικά εξαρτήματα υψηλής τεχνολογικής ωριμότητας (TRL). Επιπρόσθετα, προκειμένου να βελτιστοποιηθούν οι χρόνοι φόρτισης που ακολουθεί το SELAS σχεδιάστηκε ένας αλγόριθμος καθορισμού της πορείας του. Οι δυνατότητες του SELAS δοκιμάστηκαν μέσω προσομοιώσεων στο MATLAB, λαμβάνοντας υπόψη διάφορα σενάρια κατανάλωσης ενέργειας ρομποτικών αποστολών στον κρατήρα Henson. Τέλος, δύο ξεχωριστές διατάξεις αξιολογήθηκαν: μία διάταξη 1:1, όπου ένα SELAS φορτίζει ένα rover, και μία διάταξη 2:1, όπου ένα SELAS φορτίζει δύο rovers. Το SELAS αποδεικνύεται εξαιρετικά αποτελεσματικό σε σύγκριση με συμβατικές λύσεις, ιδιαίτερα σε επιχειρήσεις ρομποτικών σμηνών, όπου έχει την δυνατότητα να υποστηρίζει επαρκώς πολλαπλά rover (διάταξη 2:1) μειώνοντας αισθητά τη συνολική μάζα του συστήματος συνεπώς και το τελικό κόστος της αποστολής.

Abstract

The exploration of the lunar south pole has emerged as a prime objective for space agencies and companies, driven by the need to develop long term operations in the Moon. A critical component of this endeavor is the efficient utilization of lunar resources, particularly volatiles, which can support the production of propellant and oxygen. Permanently shadowed regions (PSRs), known for their extremely low temperatures, are promising locations for volatile deposits. However, these areas present significant operational challenges for robotic missions due to perpetual darkness and harsh environmental conditions. Conventional photovoltaic-battery systems are often inadequate, requiring disproportionally large batteries or frequent mission downtime for recharging, while radioisotope-based systems pose environmental and technical risks. This thesis introduces SELAS (Solar Energy Lightweight Adjustable Station), a solar-powered charging rover designed to operate in illuminated regions of the lunar south pole and recharge prospecting rovers working in PSRs. SELAS features an advanced energy management system (EMS) and an optimized power architecture developed using the particle swarm optimization (PSO) algorithm, minimizing system mass while ensuring reliability. By exclusively employing components of high technology readiness, SELAS adopts a pragmatic approach. A custom algorithm optimizes SELAS's daily traversing and charging schedules. The capabilities of SELAS were tested through MATLAB simulations considering varying power consumption scenarios and operational conditions of missions in Henson Crater. Two configurations were evaluated: a 1:1 setup, where one SELAS charges a single rover, and a 2:1 setup, where one SELAS charges two rovers. Results demonstrated SELAS's superior performance compared to conventional power solutions, particularly in robotic swarm operations, where it effectively supports multiple rovers.

Contents

List of Abbreviations

ALSEP ..... Apollo's Lunar Surface Experiment Package

BS ..... Battery Stack

CLEP ..... Chinese Lunar Exploration Program

EMS ..... Energy Management System

FPGA ..... Field Programmable Gate Arrays

GA ..... Genetic Algorithms

GPHS ..... General Purpose Heating Source

GNC ..... Guidance Navigation and Control

ISRO ..... Indian Space Research Organization

ISRU ..... In-Situ Resource Utilization

LPR ..... Lunar Penetrating Radar

LRO ..... Lunar Reconnaissance Orbiter

LTO ..... Lithium Titanate Oxide

MMRTG . ..... Multi-Mission Radioisotope Thermoelectric Generator

MSolo ..... Mass Spectrometer Observing Lunar Operations

NASA ..... National Aeronautics and Space Administration

NRVSS .... Near Infrared Volatiles Spectrometer

OBDH ..... On-Board Data Handling

PCAM ..... Panoramic Camera

PSO ..... Particle Swarm Optimization

PSR ..... Permanently Shadowed Region

PV ..... Photovoltaic

RTG ..... Radioisotope Thermoelectric Generator

SELAS ..... Solar Energy Lightweight Station

SoC ..... State of Charge

SPA ------- South Pole-Aitken

SRG ..... Stirling Radioisotope Generator

STC .....Standard Test Conditions

TCS .....Thermal Control System

TMTC .....Telecommunications

TRIDENT ..... Regolith and Ice Drill for Exploration of New Terrains

VIPER .....Volatiles Investigating Polar Exploration Rover

VNIS .....Visible and Near-Infrared Imaging Spectrometer

1

Introduction

Space agencies around the globe are in a renewed race to send crewed missions on the lunar surface by 2030. The Artemis program, developed by the National Aeronautics and Space Administration (NASA), is poised to lead this effort, aiming to secure a prolonged activity on the Moon and lay the groundwork for the next major leap: human exploration of Mars. It has been almost five decades since the last lunar landing by astronauts during the Apollo program, a period during which robotic missions have pushed the boundaries of deep space exploration with significant technological advancements and scientific discoveries [1].

In parallel, the Chinese Lunar Exploration Program (CLEP) has accomplished significant milestones, showcasing its engineering prowess to conduct roundtrip missions to the Moon. A notable achievement is the Chang'e Project's pioneering exploration of the Moon's far side, marking a historical first. Furthermore, it successfully collected volcanic specimens from the early phases of Procellarum KREEP Terrane. [2]. China has also unveiled an ambitious strategy for crewed lunar missions, focusing first on a human landing and subsequent scientific exploration. This initiative envisions a large-scale geological survey, involving a traverse spanning a thousand-kilometer to create a thorough cross-section of Moon.

In the coming decade, a diverse range of compact payloads, including small rovers, advanced scientific equipment, and independent surface systems, will play a critical role in paving the way for future phases of human exploration. Among the most crucial missions on the lunar

surface are those focused on prospecting for volatiles. These extraterrestrial prospecting missions are fundamental in the preparatory stages for resource harvesting and extraction in space, providing essential knowledge to facilitate efficient and effective mining operations.

Given the high risks and significant costs associated with human spaceflight, these prospecting missions are predominantly robotic. This approach allows stakeholders to carefully assess the risks and potential returns of resource extraction. In many cases, In-Situ Resource Utilization (ISRU) missions are designed to locate water ice or hydrated minerals and extract water for electrolysis into hydrogen and oxygen, or to reduce oxides in regolith for oxygen production. These extracted materials can be liquefied, stored, and utilized as rocket propellants [3] in cislunar space or repurposed for life support systems, such as oxygen and water generation [4].

However, the greatest challenge for these systems will be surviving and operating during the extreme cold of the lunar night. Most of these payloads will rely solely on battery power and will lack the benefit of radioisotope heaters for thermal management [5]. The harsh lunar environment presents significant challenges for all surface missions, including exposure to dust, radiation, vacuum conditions, and extreme temperature fluctuations. Due to the absence of a moderating atmosphere, surface temperatures are influenced by the time of day, latitude, and local topography and can vary between -223.15°C to 116.85°C. While daytime temperature extremes are somewhat milder in polar regions, the low solar elevation results in substantial shadowing from surrounding topography, drastically affecting surface temperatures [5].

The extended period of the lunar night, which spans an average of 354 hours due to the 29.531-day synodic lunar month, further complicates operations. During this period the lack of sunlight and the significantly cold environment, induced by the low temperatures in both space and on the lunar surface, eliminate external energy sources, creating a formidable challenge for energy storage. Ensuring consistent functionality or survival through this extended night is arguably "The most complex energy storage problem encountered in solar system exploration." [6].

1.2 Thesis Contribution

This thesis presents the conceptualization and design of a specialized rover’s power system, SELAS (Solar Energy Light Adjustable Station), intended to function as a mobile charging platform for rovers operating in the permanently shadowed regions of the lunar south pole.

SELAS, employs an energy system that integrates photovoltaics and Li-Ion batteries, managed by an advanced Energy Management System (EMS) to meet its own power demands and guarantee the seamless continuation of the rover's exploration activities in the PSR.

Furthermore, an optimization algorithm has been utilized to determine the appropriate sizing of the photovoltaic arrays and battery system, as well as to optimize the daily charging schedule by optimizing the frequency of the charging sessions through an Earth day. Based on this frequency, a traverse algorithm that has been developed for the purpose of this thesis, facilitates SELAS' navigation to the nearest illuminated areas and the daily charging schedule thereby reducing travel times. A comprehensive case study in Henson crater has been conducted to evaluate system performance under simulated scenarios, varying in the instrumentation of the prospecting rover and therefore its power consumption.

Innovative contributions of this thesis include a power delivery system that operates independently of the prospecting rover, eliminating the need for integrated photovoltaic panels or oversized batteries. This enables seamless rover operations within PSRs for at least a year while significantly reducing the overall weight of the required power system. Furthermore, SELAS avoids the use of environmentally controversial solutions such as Radioisotope Thermoelectric Generators (RTGs).

Moreover, SELAS offers a flexible charging solution across the lunar landscape, provided that adequate charging points are available in close distance. The introduced algorithm further enhances operational efficiency by dynamically selecting the nearest charging location to the target exploration area and optimizing the travel schedule accordingly. Lastly, the devices selected for the developed system are off-the shelf products making the system realistic and cost efficient.

1.3 Thesis Outline

This thesis is structured into eight chapters, in line with the logical progression of steps undertaken during the development of this work:

Chapter 1 - Introduction: provides the general context in which the current thesis is based on, outlines its objectives and defines its scope.

Chapter 2 - Theoretical Background: covers essential theoretical concepts relevant to the work, including the lunar environment and its challenges, the significance of PSRs and prospecting, relevant robotic missions, and commonly used power systems for such missions. It also introduces fundamental optimization algorithms.

Chapter 3 - SELAS' Concept Description: introduces SELAS, detailing its fundamental functions, system characteristics, and power consumption requirements.

Chapter 4 - Modelling of SELAS: offers an in-depth explanation of the models and equations used to simulate SELAS, including photovoltaic systems, horizontal and vertical tracking mechanisms, batteries, and the algorithm for calculating SELAS' traverse schedule.

Chapter 5 - Simulation of SELAS: describes the case studies designed to evaluate SELAS' capabilities. It includes an analysis of the selected site for the case studies and details each scenario, where the charged rover varies in instrumentation, scheduling, and power consumption to test SELAS under diverse conditions.

Chapter 6 - Optimization of the System: defines the primary decision variables used in the optimization process.

Chapter 7 - Results: presents the outcomes of the simulations and optimization process, accompanied by a detailed analysis of the state of charge (SoC) for all battery stacks.

Chapter 8 - Conclusions and Discussion of the Results: discusses the findings from Chapter 7, evaluates SELAS' capabilities based on these results, and identifies future steps for further system optimization.

To streamline the writing process, the following conventions will be adopted:

- The term **"**day**"** will refer to a typical 24-hour Earth day. When referring to a lunar day, this will be explicitly stated.
- The time format used in the simulations conducted for this thesis is Coordinated Universal Time (UTC).
- The term "year" will refer to a typical 365 Earth days year. When referring to a lunar year, this will be explicitly stated.
- The term **"**rover**"** will specifically denote the vehicle engaged in research, excavation, or prospecting activities, which SELAS is responsible for recharging.
- The term **"**system**"** will collectively encompass the power architecture of SELAS—comprising its batteries, photovoltaics, and chargers—as well as the batteries within the rover.

2

Theoretical Background

Designing an energy management system for a lunar rover is a complex process that requires careful consideration of numerous factors. This chapter outlines the key aspects that affected the design of SELAS and influenced the optimization process. The first section focuses on the critical characteristics of the lunar environment that directly affect the operation and power consumption of the systems developed in this thesis, thereby shaping the optimization results. It includes an analysis of potential PSRs rich in volatile resources, emphasizing their terrain slopes and illumination, which are essential for determining SELAS' power allocation strategy.

The second part of this chapter reviews past robotic missions on the lunar surface, examining their instrumentation, power requirements, and traverse planning to act as a benchmark for the design of SELAS' energy management system. Additionally, it evaluates various power generation and storage options, comparing their capabilities with SELAS' potentials. Lastly, it gives a brief overview of the main power consuming systems of a lunar rover, such as the thermal management system, on-board data handling and telecommunications. Given the significance of payload weight as the primary cost-driving factor in space exploration, the chapter is completed with a literature review on the mass ratios required for a lunar surface launch vehicle and the associated costs.

The third section of this chapter presents a review of optimization processes and algorithms, exploring their capabilities and ultimately identifying the algorithm used in this thesis.

2.1 Environmental Conditions at the Lunar Surface and Implications on Rovers & Power Systems

Insights from the Apollo lunar exploration program and various robotic lunar missions have underscored the significant challenges posed by the lunar environment for hardware operations. These include extreme temperature variations during the lunar day-night cycle, vacuum conditions that restrict material selection, intense radiation exposure, and the pervasive issue of lunar dust and regolith.

The primary environmental factors influencing system design are thermal, radiation, and dust conditions, while terrain considerations are secondary but still addressed. The micrometeorite environment, posing minimal risk to rover missions, is excluded from this thesis.

Despite these challenges, the rigorous environment of the lunar south pole also presents valuable opportunities, particularly the availability of volatiles and water ice within permanently shadowed regions. These resources play a vital role in future lunar habitation, offering potential for propellant production, oxygen and water. A concise analysis will be provided of high-potential resource-rich areas, emphasizing their general characteristics and feasibility for exploration, considering factors such as terrain trafficability, telecommunications, and illumination conditions.

2.1.1 Orbital Parameters

The sidereal rotation period of the Moon is 27.321661 days, while the span of a single synodic lunar day is 29.530589 days [7]. Moon's rotational axis is tilted at an angle of 6.581° relative to its orbital plane, inclined at 5.141° to the ecliptic. The well-known Cassini's laws are applicable to the Moon with a high level of precision:

1. The Moon exhibits a 1:1 orbital resonance, meaning its rotation and orbit are synchronized so that one hemisphere constantly remains facing Earth.
2. The Moon's rotational axis maintains a consistent angle of inclination relative to the ecliptic plane. As a result, the axis traces a cone whose intersection with the ecliptic plane forms a circle.
3. The Moon's rotational axis lies within a plane defined by the normal to the ecliptic plane and the normal to its orbital plane. The rotational axis deviates 1.5431° from the North ecliptic pole, with the normal to the orbital plane and the rotational axis positioned on opposite sides of the normal to the ecliptic. Consequently, the normal to

the orbital plane and the Moon's rotational axis precess around the ecliptic pole with an identical retrograde period of approximately 18 years [7].

As a result, except for polar landing sites, surface systems on the Moon that require extended operation must endure lunar nights that can last up to 16 days or 384 hours.

Solar radiation on the Moon fluctuates according to its proximity to the Sun ranging from 1316 W/m² to 1421 W/m² [8]. The radiation from the Earth when fully visible is approximately 0.095 W/m² [9] which is negligible for thermal design considerations of lunar surface systems. The typical Bond albedo of the lunar surface, significant for its temperature regulations, is 0.11 and the average visual geometric albedo is 0.12. Albedo is influenced by the solar zenith angle and varies across different areas of the Moon.

2.1.2 Lunar Atmospheric Conditions

For much of modern scientific history, it was widely believed that the Moon lacked an atmosphere entirely. This notion persisted until 1973 when instruments from the Apollo missions began detecting signs of a tenuous lunar atmosphere. The presence of helium and argon isotopes was detected by a mass spectrometer at lunar dawn and dusk [10],[11]. The Moon's atmosphere consists of a sparse layer of gases, with surface pressure around 3×10^{-15}atm (compared to Earth's surface pressure of approximately 1 atm) and an atmospheric mass of roughly 25,000 kg (Earth's atmospheric mass is approximately 5.1×10^{18} kg) [10].

The Moon's atmosphere is exceedingly tenuous, effectively an exosphere. Key components include neutral gases, plasma, and ejected dust particles generated by the interaction between the lunar surface and the space environment. While these elements are scientifically intriguing, they have gained engineering relevance due to their impact on proposed human and robotic activities on the Moon.

The Moon's atmospheric conditions resemble those of interplanetary space. Its neutral "atmosphere" contains 10^4 kg of gaseous species, equating to particle densities of 10^5 to 10^7 particles/cm³—14 times less dense by orders of magnitude compared to Earth's atmosphere [12]. Additionally, the Moon's environment features energetic particles, such as those from the solar wind, solar flares, and galactic cosmic rays. The absence of a substantial atmosphere and global magnetic field allows this radiation to interact directly with the surface inducing detectable changes in the topmost layer and generating secondary radiation [12].

2.1.3 Radiation on the Lunar Surface

The lunar surface is exposed to electromagnetic radiation, primarily originating from the Sun, with an average energy density of 1362 W/m² at 1 AU, as well as ionizing radiation, which consists mostly of protons, electrons, and some nuclei of greater masses [13]. Ionizing radiation is generally categorized into three primary sources [14]:

- Solar Wind Particles (SWP): low-energy particles
- Galactic Cosmic Rays (GCR): high-energy particles
- Solar Energetic Protons (SEP): high-energy protons

Additionally, interactions between these radiation sources and the lunar surface or subsurface can generate secondary radiation, including helium and heavier ions as well as electrons [16]. Radioactive isotopes within the lunar regolith, also contribute approximately 1% of the total radiation through natural decay [14].

Insight into the radiation conditions at the Moon remain limited, as most measurements have been conducted in orbit rather than directly on the surface. Some models and simulations, such as those by Reitz et al. [17], have been used to estimate radiation exposure. These studies indicate that there is a higher concentration of hydrogen and helium nuclei and carry higher energy compared to oxygen and iron ions.

Data derived from missions like Chandrayaan-1 (C1) and the Lunar Reconnaissance Orbiter (LRO) have provided measurements at three different orbital altitudes, contributing valuable information to this field of study. These results are presented in Table 2-1 [17].

Table 2-1. Lunar radiation levels (mean dose) relative to orbital altitude [17].

Orbit Altitude	Average Dose	Mission
50 km	0.22 – 0.27 mGy/d	LRO
100 km	0.227 mGy/d	C1
200 km	0.257 mGy/d	C1

There are three different potential effects of radiation on electronics and rover systems in general. The total Ionizing Dose (TID), the displacement effects (DE), and the Single Event Effects (SEE) which is a generic term encompassing all possible effects [18].

The Total Ionizing Dose effect can impact all types of electronics, as ionization generates charge within semiconductor materials. While most of this charge can be collected and

removed without harm, in semiconductor dioxide/silicon interface devices, such as modern CMOS-based circuits, charge trapped at the interface can cause long-term effects [18].
TID effects are typically mitigated through shielding, which reduces the energy or population of the radiation environment. However, shielding introduces tradeoffs, as increasing its thickness adds weight and cost, particularly for lunar missions. Additionally, the effectiveness of shielding is not linear, and beyond a certain point, further additions provide minimal benefit [18]. In such cases, replacing components with radiation-hardened versions becomes the most reliable solution.

Displacement effects in electronics cause diodes to lose effectiveness, allowing easier two-way current flow, and reduce the amplification capabilities of transistors. These effects, like the TID, are cumulative, with minor impacts initially that worsen over time with increased radiation exposure. Solar cells are particularly affected, experiencing reduced efficiency as diodes degrade under radiation, potentially losing up to 50% of their power output depending on construction and environmental conditions.

While shielding can mitigate displacement effects, implementing it for solar arrays is challenging [18]. The shielding, or "cover glass" must be transparent to optical photons and minimize refractive losses, but increased thickness results in higher transmission losses. Thus, a balance is required between tolerable radiation degradation and maintaining power production efficiency.

2.1.4 Lunar Surface Temperature

The absence of a substantial atmosphere leads to extreme temperature fluctuations depending on solar exposure. Without an insulating layer to retain heat, temperature fluctuations span from extremely hot to frigidly cold. Through the lunar day, when sunlight illuminates the surface, temperatures can reach up to 106.67°C. Conversely, during the lunar night, areas without sunlight, experience temperatures as low as - 183.33°C. Due to the axial tilt of the Moon, certain regions near the lunar poles remain in perpetual shadow. NASA's Lunar Reconnaissance Orbiter (LRO) documented temperatures of -237.78°C at the south pole and -247.22°C° at the north pole, marking the coldest measurements in the solar system to date [10]

The lunar day-night cycle, characterized by approximately fourteen consecutive Earth days of sunlight succeeded by fourteen days of uninterrupted darkness and extremely low temperatures, represents one of the most formidable environmental challenges in solar system

exploration. Temperatures in PSRs can be even lower [6]. PSRs are significantly colder than the average lunar surface, with maximum temperatures below −173.15°C [1]. These extremely low temperatures create conditions suitable for trapping and accumulating water ice and other frozen volatiles [19], potentially preserving them for hundreds to millions of years.

The surface temperatures within PSRs are primarily influenced by reflected sunlight and infrared radiation originating from nearby topographical features [19]. It is worth noting that close to the lunar south pole, an area can be found without temperature fluctuations throughout both day and night. This phenomenon is attributed to the so-called peaks of eternal light, as discussed in Chapter 2.1.3. An annual mean temperature map of the south pole, is illustrated in Figure 2-1.

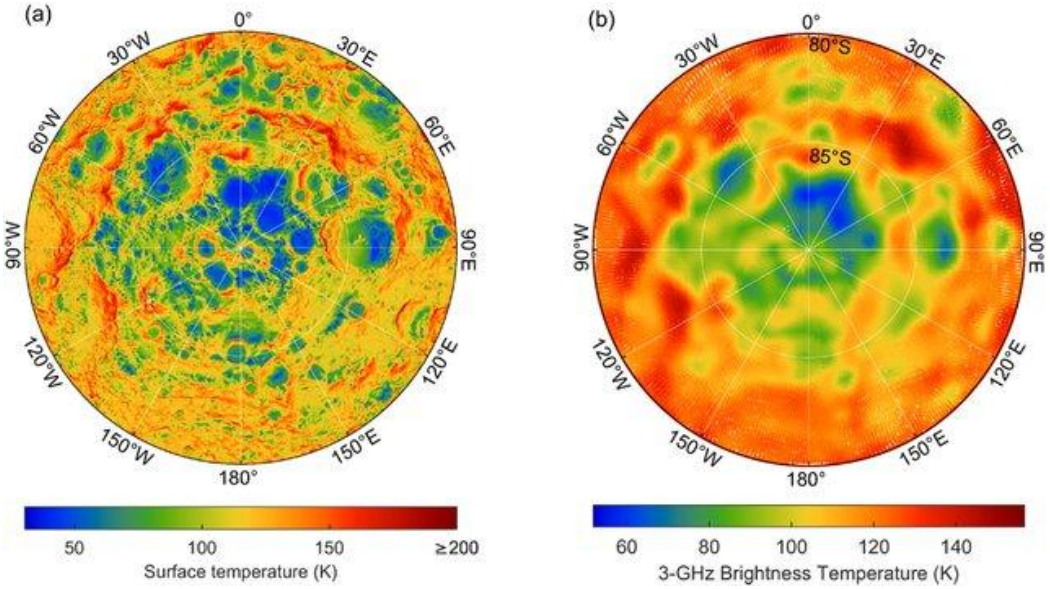

Figure 2-1. (a)Annual average surface temperature map of the lunar south pole" (b) "A polar stereographic projection displaying CE-2 Microwave Radiometer 3-GHz data points in the lunar south pole [20].

Various thermal regulation designs and insulation methods have been developed to ensure the operational functionality of rovers amidst extreme temperature fluctuations. Electronic components, being highly sensitive, impose the most stringent temperature requirements and must be maintained from -40°C to 50°C. Thermal assessments are performed with a variety of hardware options, mainly with several static radiator surfaces, heat switches, deployable panels, louvres and radioisotope thermoelectric generators (RTG's) [21].

Heat pipes, are also commonly used in rover systems for maintaining electronics at operational temperatures that are closed in metal containers lined with a capillary wicking material [22]. Upon heating any specific point of the pipe, the liquid at that location vaporizes, rapidly transferring heat energy throughout the interior of the pipe while drawing additional liquid to the heated area via capillary action. The heat is subsequently dissipated to the colder side of the pipe, resulting in exceptionally high thermal conductance [22].

Additionally, paints and coatings with tailored emittance and absorptance properties are effective for thermal regulation through radiative effects. High emittance facilitates the efficient radiation of internally generated heat, while low absorptivity minimizes the impact of solar heating variations [22]. Furthermore, multilayer reflective insulation and aerogels are highly effective insulating materials for space applications. By leveraging their distinct principles, these materials can complement each other. Multilayer insulation is ideal for large, flat, smooth surfaces, while aerogels are best suited for seams, corners, and other intricate features. This dual approach is commonly employed in lunar rover insulation strategies.

2.1.5 Illumination Conditions

As highlighted in numerous studies, the morphometric characteristics of the lunar south pole—such as slopes, crater density, and surface roughness— do not vary greatly from other lunar locations. However, the polar areas are unique due to their low solar elevation angles compared to the equatorial areas previously explored by the Apollo, Luna, and Lunokhod missions. These low Sun angles create isolated locations with extended periods of illumination throughout much of a terrestrial year, as well as areas that receive little to no sunlight over the same period. These conditions, characterized by temporally variable lighting, offer both operational advantages (such as access to solar power and volatile resources) and challenges for mission planners aiming to ensure safety during polar missions [23].

Aligned close to perpendicular with the ecliptic plane, the lunar poles have an inclination of roughly 1.5° from the vertical. This results in the Sun consistently appearing near the horizon at the poles as the Moon completes its slow rotation every 708 hours, equivalent to approximately 29 Earth days. Consequently, topographical variations, such as elevated ridges or depressions, can create areas that are either permanently illuminated or permanently shadowed [26].

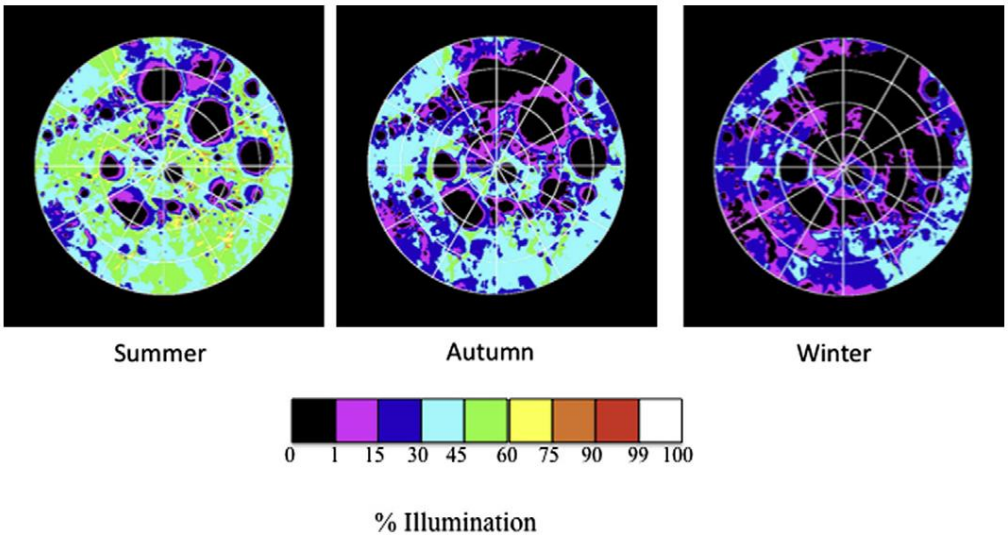

Figure 2-2. Maps displaying quantitative illumination data for lunar days in summer, autumn, and winter, covering latitudes from 86°S to the pole, with the 0° longitude line at the top [14].

From a power generation and thermal control perspective, the 14-day lunar night or operating within PSRs poses a substantial challenge for long duration missions. Therefore, it becomes crucial to explore lunar regions where, due to topographical features, illumination is less restricted. Mountains exceeding heights of 600 meters, such as high crater rims [15]in the polar regions may rise above the horizontal line and receive continuous solar illumination. In some cases, achieving adequate illumination for solar power generation may require systems to be positioned at a specific height [16]. A steady supply of solar energy is essential to ensure constant power generation, regulate thermal conditions, and enable advanced exploration activities for extended in situ missions focused on impact craters near the lunar South Pole. Previous research has shown that elevated crater rims near the poles typically have more favorable illumination conditions compared to other areas [24].

Lastly, [25] examines the illumination profile at suggested locations near the lunar North and South Poles with favorable lighting, both at the surface level and at an altitude of 10 meters. The study highlights that even a small elevation of 10 meters can significantly improve average illumination. Further notable improvements, however, are only observed at substantially greater altitudes. At 10 meters, occurrences of prolonged multi-day night events can be completely circumvented. Notably, while the longest continuous night at the surface lasts 5.88 days, this duration is reduced to just 2.75 days at a 10-meter elevation.

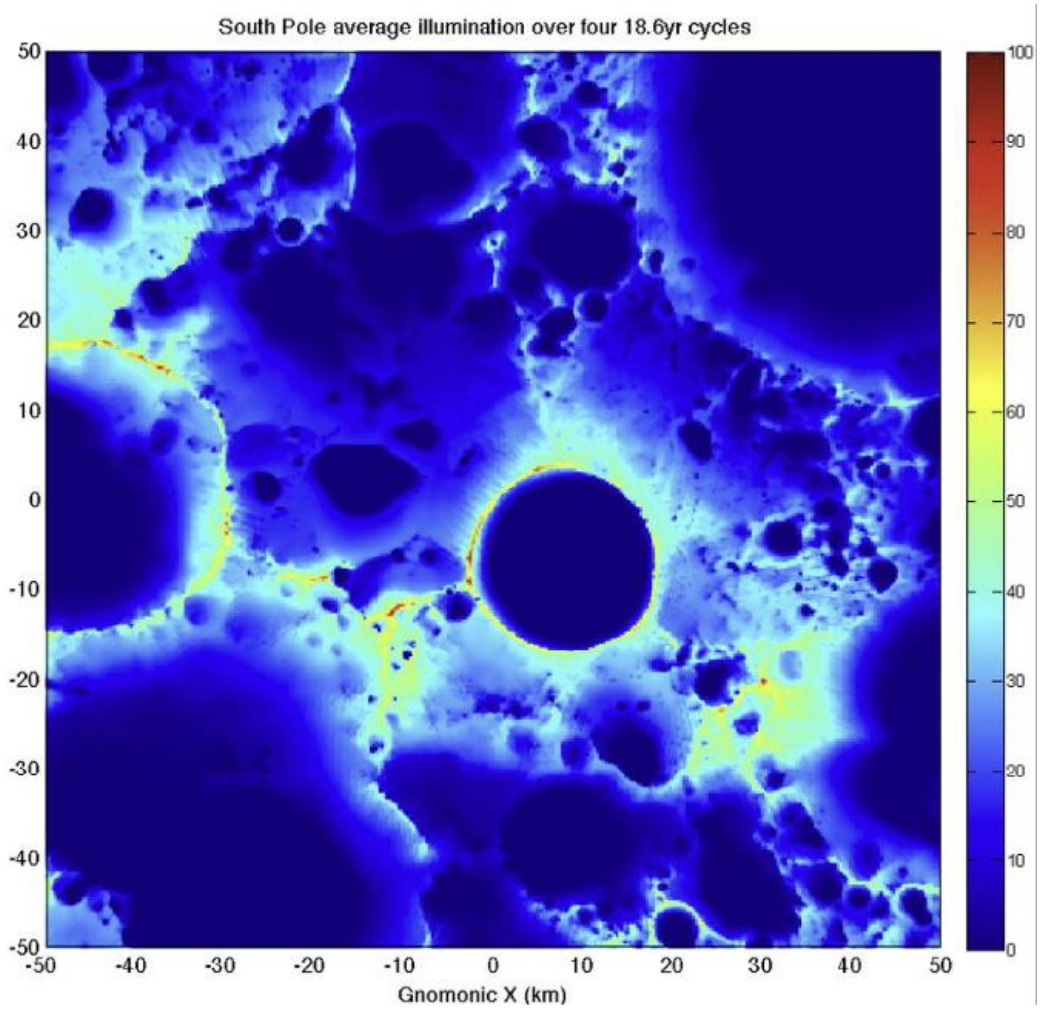

Figure 2-3. Average illumination (in percent) in the lunar South polar region [14].

2.1.6 Lunar South Pole Topography

The South Pole-Aitken (SPA) Basin, located in the Moon's south pole, it ranks among the largest and most ancient impact basins on the Moon's surface. With a diameter of 2,600 km and a depth of approximately 12 km, it is centered at approximately 56º S, 180º N. Formed after the Moon's crust solidified, the basin is believed to be almost 4.3 billion years. The south pole itself lies just within the SPA basin's main rim, a rough, elevated highlands region characterized by numerous craters of various ages and extreme elevation changes. The region's roughness is influenced by the SPA basin's rim and plenty of secondary craters, many formed by the Orientale Basin impact to the north.

Wheeled systems, such as NASA’s Sojourner, Mars Exploration Rovers, Curiosity, Perseverance, and China’s Yutu and Yutu-2, will generally offer greater energy efficiency compared to other types of advanced robotic mobility on relatively flat and gentle terrain due

to their six-wheel rocker-bogey suspension systems. However, much of the Moon's surface is challenging for purely wheeled systems [26]. Rugged, steep, and obstacle-filled terrains near crater rims, with slopes often exceeding 20-30 degrees, pose significant navigation challenges but hold high scientific value due to the exposure of ancient rocks that offer insights into the solar system's history [26]. Similarly, lunar lava tubes, with their stable temperatures and natural radiation shielding, are of great interest for human habitats and geological studies, but their largely unexplored and unpredictable environments necessitate innovative mobility solutions [26].

Current and future lunar missions are exploring alternative locomotion technologies. Legged robotic systems, such as Boston Dynamics' Spot and ANYbotics' ANYmal, have demonstrated exceptional navigational skills across challenging terrains and are increasingly used for demanding exploration missions [27], [28], as highlighted in projects like NASA's BRAILLE, that analyzes methods for exploring lunar lava tubes, underscoring the potential of legged robots for overcoming the challenges posed by the Moon's rugged terrain [26].

2.1.7 Lunar Dust

The lunar regolith constitutes a layer of loose, fine-grained soil that blankets nearly the entire surface of the Moon. Only certain steep crater walls and lava channels where bedrock might be visible, lack of regolith. This layer, with a density of approximately 1.5 g/cm³, consists largely of fine soil mixed with larger rock fragments and breccia. The thickness of regolith differs among the lunar sites, measuring about 4-5 meters on the lunar mare and 10-15 meters in the highland regions [10].

This gray, sand-like material is a heterogeneous mixture of rock fragments, minerals, glass, and glass-bonded aggregates known as agglutinates [29]. The lunar soil is comprised of exceptionally small grains, described as "dust." The median size of the particles is between 40 μm and 130 μm, while particles that are no bigger than 20 μm comprising 10% to 20% of the weight [29].

Lunar dust poses a major obstacle for upcoming exploration efforts introducing risks of contamination and health issues for astronauts. Mechanical systems could face significant issues due the angular and interlocking nature of regolith, along with the varying grain size. Dust-related issues were encountered in all Apollo missions, with equipment failures and dust deposition on exposed materials proving inevitable and challenging to address [30].

Dust can damage hardware in several ways. It can infiltrate the gaps between components in rigid-body mechanisms, increasing friction and potentially jamming kinematic pairs. Traditional sealing methods, such as joint seals, are often ineffective against the abrasive nature of lunar dust, as observed during the Apollo missions. This abrasion damages smooth surfaces, such as solar panels, thermal coatings, and sensors.

Additionally, the electrically charged nature of lunar dust can lead to destructive dielectric discharges, damaging sensitive microelectronics, causing short circuits, or resulting in insulating failures [31]. Grounding and shielding strategies should be prioritized at the early stages of the design phase, with measures implemented, to seal sensitive electronics and prevent lunar dust intrusion [32]. Exposure to charged dust can result in catastrophic failures of active components, including but not limited to field-programmable gate arrays (FPGAs), power amplifiers, low-noise amplifiers, and mixers [32].

To address the dust mitigation issue in coupling between rovers or when exterior sockets are needed, Honeybee Robotics Spacecraft Mechanisms Corporation, in collaboration with NASA, has developed quick-disconnect utility connectors developed to endure and minimize the effects of lunar dust deposition [33], [34]. These connectors, intended for battery recharging and coupling between rovers, may present a viable solution for SELAS as well.

2.1.8 PSRs & Candidate Locations for Future Robotic Missions

The lunar polar regions host permanently shadowed regions that have no exposure to the sun at any phase for the lunar day. These ultra-cold environments ($< -163.15°C$) are capable of cold-trapping volatile materials such as water or CO_2 in ice form, which are critical for developing a steady human presence at the moon and potentially develop a cislunar economy. Since 1998, four lunar orbiters—Lunar Prospector, Chandrayaan-1, Kaguya, and Lunar Reconnaissance Orbiter —have provided an insight on characterizing hydrogen (H), hydroxyl (OH^-), and other volatiles through techniques such as thermal infrared, neutron spectroscopy, radar backscatter, visible reflectance, and near-infrared absorption [35].

However, these results, while useful for inferring the existence of surface or subsurface volatile deposits, are not always consistent across datasets in confirming water ice at specific locations [35]. Among the identified PSRs, Faustini, Cabeus, de Gerlache, Shoemaker, Haworth, Sverdrup, Slater, and Amundsen are considered to have the highest potential concentration of resources. Shackleton crater is highlighted for its strategic importance due to

its morphology, alignment with the lunar south pole and its vicinity to the the South Pole-Aitken basin.

A robust ranking of volatile resources from 65 PSRs provided by *Brown et. al* [35], indicates that de Gerlache, Sverdrup, Slater, and smaller PSRs near the south polar ridge, provide an advantageous environment for in-situ exploration of volatile concentrations. While PSRs such as Faustini, Shoemaker, Haworth, Cabeus, and Amundsen are the most promising for high volatiles concentrations, their accessibility remains challenging. Faustini is particularly noted for having the highest potentials to contain abundant water ice.

These regions are characterized based on the framework proposed by *Brown et al.* [35], which categorizes their accessibility in relation to potential mission profiles as follows:

1. Traversable Path: regions with slopes of less than 10° over a 25 m baseline, enabling access from the rim to floor, to robotic systems that have landed outside of the crater.
2. Partially Illuminated Floor: unreachable regions due to harsh terrains but a partially sunlit floor, enabling the landings in sunlight with available paths into the PSRs.
3. Challenging Access: regions with neither traversable walls, nor an illuminated floor, necessitating missions that operate entirely in darkness or utilize remotely deployed instrument packages.

This analysis and the above-mentioned classifications evaluate the significance and key characteristics of specific regions that will inform the selection of a site for the SELAS case study.

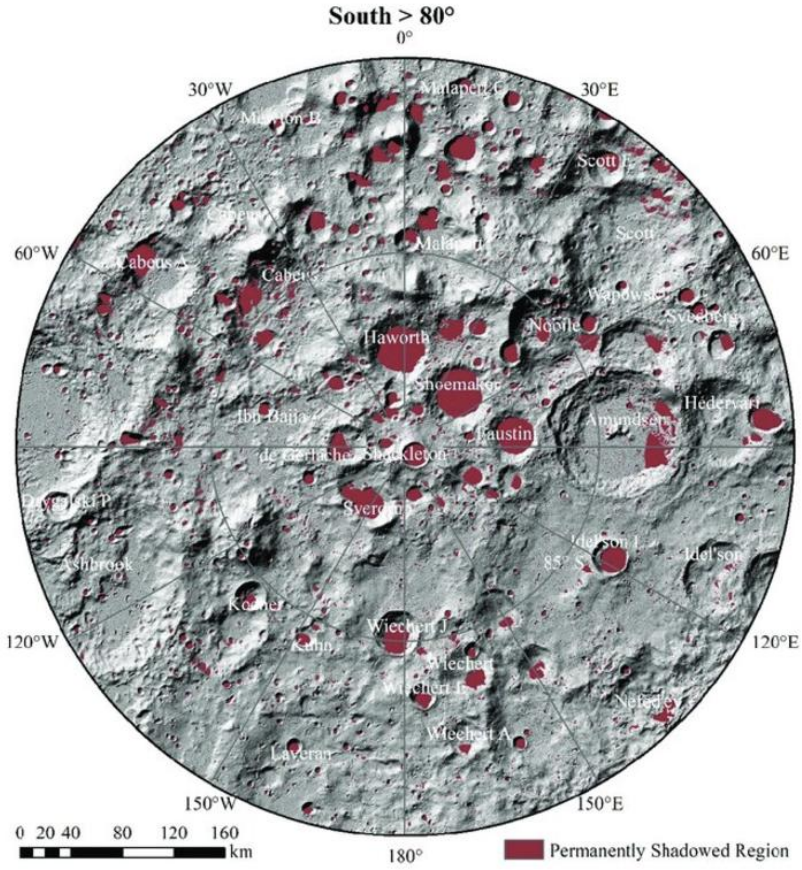

Figure 2-4. The lunar south pole's PSR, spanning 16,055 square kilometers [36].

Shackleton Crater (longitude: 128.2, latitude: 89.6) is a prominent site for potential missions due to the vicinity of the South Pole-Aitken basin and its alignment with the lunar south pole. The crater has a simple bowl-shaped structure and is almost axisymmetric. It has a rim diameter of 21 km and a depth of 4.2 km [37], [38], [39] featuring a higher depth-to-diameter (d/D) ratio of 0.195 ± 0.025 relative to other craters, similar in structure, in the south pole. Shackleton crater has significantly intact walls and rim crest [37], [39] while the peaks along its rim receive near-continuous sunlight, with approximately 80–90% of each lunar orbit illuminated [38]. Shackleton is considered a key mission area (rich in volatiles) and is classified as an accessibility class-1 crater, with relatively accessible paths from floor to rim, favorable illumination conditions and line-of-sight Earth communication, although the majority of the volatiles are most likely located at the walls of the crater increasing the difficulty of the missions.

Faustini Crater, a candidate landing site for Artemis III, includes portions of its rim and proximal ejecta as potential landing zones. With a diameter of 41 km, Faustini hosts a substantial PSR spanning 664 km² and is considered among the most resource-rich PSRs at

the lunar South Pole [35]. It features the second-largest expected areal frost coverage (129 km²) and the third-highest potential mass of subsurface ice (4×10^6 tons), necessitating advanced prospecting tools, such as drills, which would increase power demands in this low-illumination region. Mapping studies have identified three distinct floor units (Figure 2-5 (b)) based on elevation, slope, and surface roughness, correlating with temperature variations influenced by volatile sublimation [40].

The Upper Floor (elevations −2600 to −2710 m) slopes poleward and dominates the equator-facing side, while the Middle Floor (−2710 to −2740 m) is mostly flat, except for craters and a central mound. The Lower Floor (below −2740 m), separated by a broad ridge, is relatively flat but challenging due to rough terrain, featuring crater ray areas likely from Tycho and Jackson craters [40], posing extra difficulty to robotic missions and increasing power demands due to the terrain complexity. Illumination from the equator-facing wall modulates floor temperatures, with diurnal and seasonal changes affecting exploration conditions. While temperature-driven volatile trapping may explain surface property asymmetry, further prospecting is required to confirm these findings. Faustini is a key mission area, although it is classified as an accessibility class-3 crater, as it is entirely shadowed, posing additional challenges for robotic exploration.

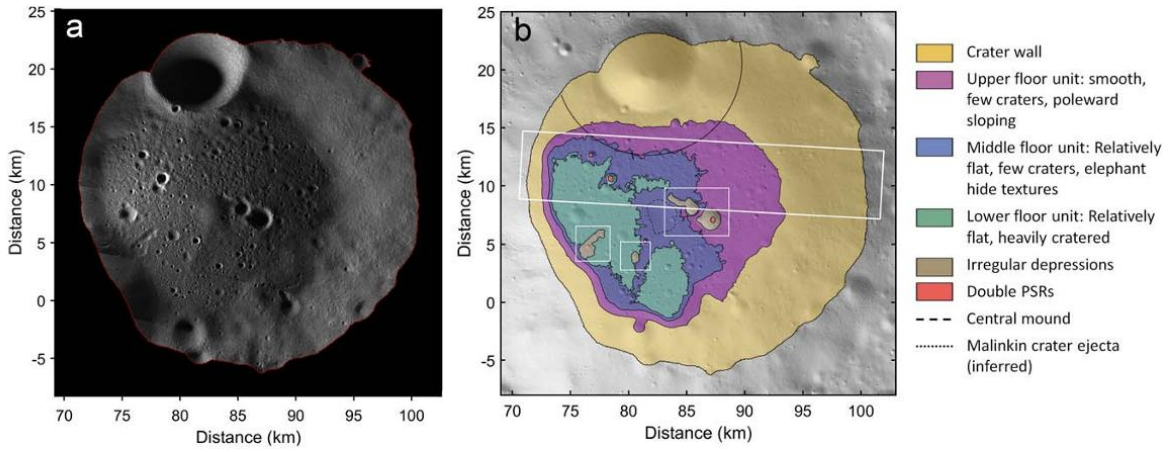

Figure 2-5. (a) Mosaic of the Faustini PSR taken by ShadowCam, with the Sun's direction facing right. (b) A geomorphic map of terrain features within the PSR [40].

Cabeus Crater, featuring a truncated cone shape with a 98 km diameter, is an area in close proximity to the lunar South Pole. Its average depth is 4 km, wall slopes of 10-15°, and a flat bottom with a diameter of 60 km [41]. A smaller crater, with a diameter of approximately 10-11 km, is situated on the western side of Cabeus. In the northern region of the crater (Figure 2-6), a large area exhibits average temperatures not exceeding -163.15°C, which is the upper

limit for the stable existence of water as a volatile compound [41]. However, maximum temperatures in this area can significantly exceed this threshold, reaching up to -123°C. Given these factors, it is necessary to consider the potential presence of volatiles beneath the regolith layer, as this layer may substantially mitigate temperature variations [41]. Cabeus is considered a key-mission area, classified as accessibility class-2 crater (illuminated landing site within crater near PSR).

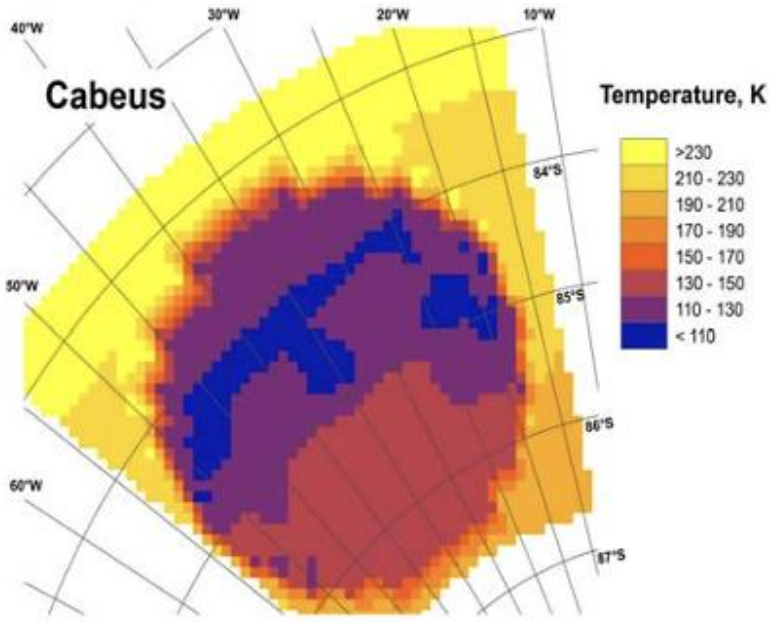

Figure 2-6. The distribution of average temperatures in Cabeus [41].

Henson Crater, a 45 km diameter region, is the oldest among those analyzed in this study, as evidenced by overlapping craters such as de Gerlache, Sverdrup, and several craters of smaller diameters, breaking its rim [42]. Other parts of Henson's rim exhibit a rim-to-floor height ranging from 1.0 to 3.5 km. Sverdrup Crater, with a diameter of 33 km, features a slightly greater rim-to-floor elevation difference of 2 to 4 km, with its highest elevated points located on the side opposite Henson [42].

A significant characteristic is that the rim between Henson and de Gerlache features illuminated sites for the majority of the lunar year. Another key consideration is the availability of mineral deposits, a potential source for infrastructures and engineering applications, such as those used in ISRU. Iron and titanium oxides are part of these resources, as well as rare earth elements (Figure 2-7) While previous studies have considered Henson-Sverdrup as a potential site, [42] identifies the Sverdrup-Henson area as significantly more

advantageous due to its resource availability, ease of access, favorable crater slopes, reliable Earth communication and access to sunlit regions.

Its primary advantage lies in its proximity to water resources (Figure 2-8) within the PSR and the easily accessed sunlit locations of adjacent craters, such as de Gerlache and Shackleton. Portions of Henson-Sverdrup Crater fall into accessibility class 1, while others are categorized within accessibility class 2 [35], with the most problems arising in communications and as the line-of sight between the PSR and Earth might not be good, although this problem can be fixed by using of non-teleoperated rovers or by establishing communication through a satellite link or with an antenna mounted on high elevated points.

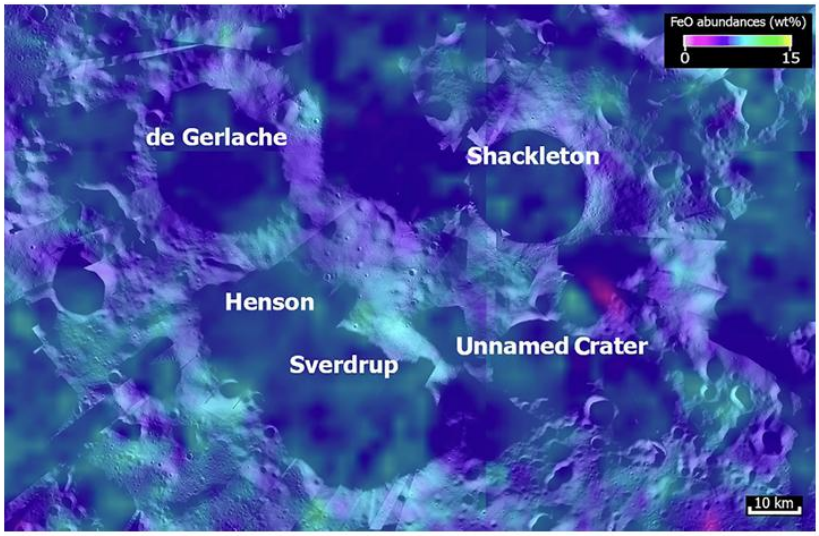

Figure 2-7. A regional map illustrating the distribution of iron oxide (FeO) abundance in the polar region [41].

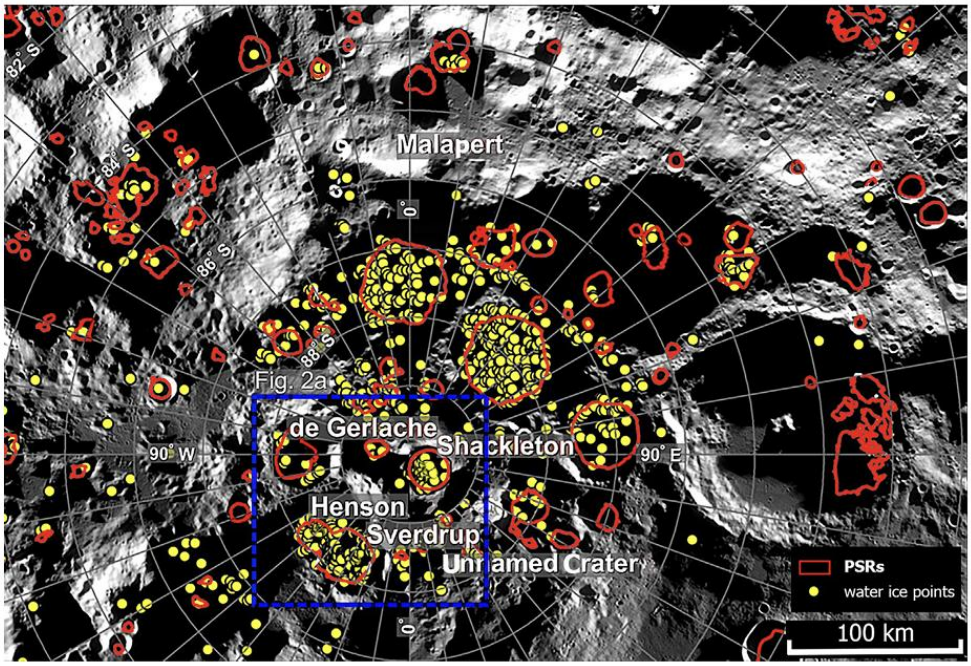

Figure 2-8. A regional map of Sverdrup, Henson, Unnamed Crater, de Gerlache, Shackleton, and the Malapert Massif. Red framed areas delineate the PSRs, yellow points indicate ice exposure areas identified by the Chandrayaan-1 M3 instrument [41].

2.2 Robotic Missions at the Lunar South Pole

In 2009, various satellite missions provided remarkable discoveries, even though none were specifically designed to search for lunar volatiles. The Chandrayaan-1 mission by the Indian Space Research Organization (ISRO), along with NASA's Cassini and Deep Impact missions, detected signs of hydrated minerals in the bright regions of the Moon. These findings indicated the presence of oxygen and hydrogen molecules, though it was not possible to differentiate between hydration due to hydroxyl (OH) and water (H_2O) [42].

Robotic and crewed lunar missions, such as NASA's Apollo program (1969–1972), Lunar Prospector (1998–1999), ESA's SMART-1 (2003–2006), China's Chang'e missions, the Lunar Reconnaissance Orbiter (2009–present), and India's Chandrayaan missions (2008–2023), have offered significant insight on Moon's composition, climate, and evolution [42]. These missions have provided critical outputs, including sample returns, detailed mapping, imaging, and data on lunar topography and surface composition. However, further research is required to refine the understanding of volatile compositions, particularly in PSRs.

While past achievements in lunar exploration are undeniably significant, the advancements and potentials posed by some of the recently introduced rovers are significant. Notable

examples include Ispace Inc.'s Sorato (4 kg) [43] and Polar Ice Explorer (12 kg) rovers [44], Astrobotics' Cuberover (4 kg) [45], and the stationary Robex Remote Unit concept (3 kg and 10 kg) [46]. Collectively, these robotic systems suggest a novel, lightweight and compact approach to explore the lunar surface, with a substantially reduced mass than those deployed in previous missions.

This chapter will examine these past lunar missions, emphasizing those with scientific relevance. Insights gained will serve as a reference for SELAS simulations, particularly in subjects such as traverse planning, instrumentation, and power allocation.

2.2.1 VIPER Mission

NASA's Volatiles Investigating Polar Exploration Rover (VIPER) mission was originally planned for lunar deployment in late 2023 [47], but after quite some delays the missions has been cancelled by NASA due to budgetary reasons. Despite its cancellation, the mission remains noteworthy as the first designed to explore PSRs, offering valuable insights into the required instrumentation and power consumption for such explorations.

The mission aimed to 1) analyze the distribution and physical state of lunar polar water and other volatiles in cold traps and regolith to understand their origin and 2) give critical insight to NASA to access the feasibility of ISRU in the lunar polar regions [48]. VIPER's site of operation is approximately a 5 × 5 km region located at 31.6218◦ E, 85.42088◦ S near the western part of Nobile crater where VIPER would land and prospect. NASA has considered various possible sites, including some of the areas examined in Chapter 2.1.8 but ruled out for various reasons (Figure 2-9).

VIPER's data collection strategy was to involve surveying distinct thermal environments, defined by ice stability depths where sublimation rates are negligible over geologic timescales. Science stations, covering at least 3800 m², were planned to be surveyed over approximately 24 hours [47], [48].

The VIPER rover was designed as a solar-powered, consisting of a battery and three approximate 1 m^2 solar arrays (one each on the port, starboard, and aft surfaces), generating 410 W of total power [48], tele-operated, four-wheeled robotic vehicle weighing approximately 450 kg. The rover would be tele-operated via a line-of-sight radio link from Earth and it was planned to traverse flat terrain at speeds of up to 20 cm/s. However, due to delays related to commanding, navigation, localization, and obstacle avoidance, its effective

speed was expected to be closer to 1 cm/s [47]. The mission duration was planned for up to 100 Earth days, covering approximately 20 km of driving.

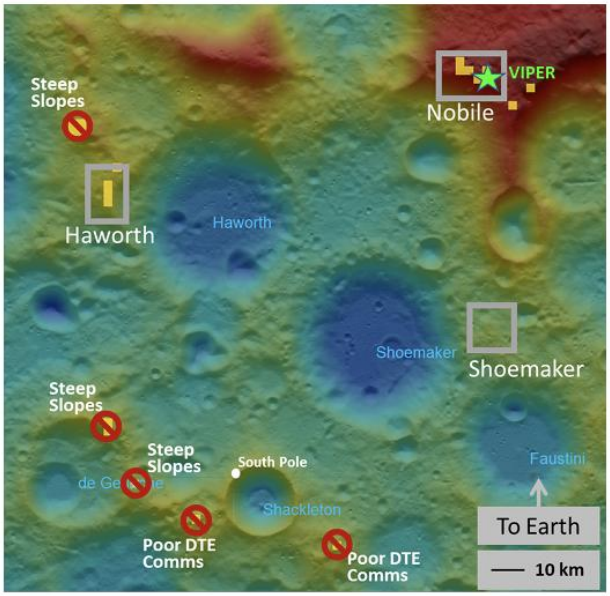

Figure 2-9. Candidate VIPER mission sites, excluded regions, and the selected final location [47].

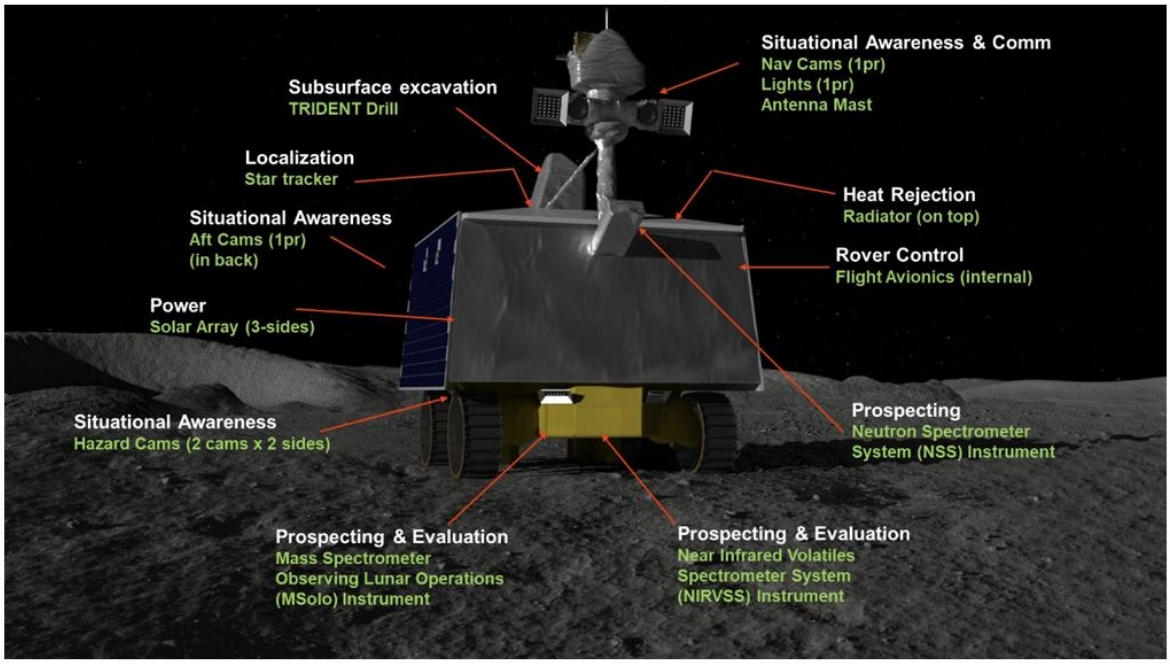

Figure 2-10. VIPER, along with its navigation, prospecting, and surface and subsurface analysis scientific instruments [48].

VIPER was expected to operate continuously, whether stationary or in motion, collecting data sets from its instruments and cameras. Activities included driving 224–335 m, active

spectrometer measurements, and drilling to a depth of 1 m at three locations, one of which included a pause for subsurface temperature measurement [47]. The paths and drill sites were to be selected to sample varying horizontal length scales (5–1000 m) [47] and morphological features. In permanently shadowed regions, surveys were to involve a single drill operation while maintaining the same driving distance.

The VIPER payload included three advanced "prospecting instruments"—the Neutron Spectrometer System (NSS), the Near Infrared Volatiles Spectrometer (NIRVSS), a thermal radiometer, and the Mass Spectrometer Observing Lunar Operations (MSolo)—all designed to operate continuously during rover traverses [60]. Additionally, the rover was equipped with a 1-meter drill, the Regolith and Ice Drill for Exploration of New Terrains (TRIDENT), capable of excavating 10 cm sections ("bites") for analysis by the near-infrared and mass spectrometers [49]. Their operational characteristics are the following:

- Neutron Spectrometer System (NSS): provided estimates of hydrogen concentration using epithermal neutron flux and bulk regolith chemical information [49]. It has a total mass of 1.9 kg and an average power consumption of 1.9 W [50].
- NIRVSS: a versatile instrument for characterizing lunar surface composition, morphology, and thermophysical properties, with a mass of 3.6 kg and an average power of 29.6 W [49], [51].
- MSolo: capable of detecting and differentiating low molecular-weight volatiles in the 1–100 amu range, allowing identification of volatile species, relative intensities, and isotopic ratios. MSolo had a mass of 6 kg and an average power consumption of 35 W [49].
- TRIDENT Drill: a fourth-generation rotary-percussive drill designed and manufactured by Honeybee Robotics, designed to excavate regolith. The drill included several subsystems: a rotary-percussive drill head, sampling auger, brushing station, deployment stage, and feed stage. It had a total mass of 21.3 kg and an average auger power consumption of 87 W [52].

2.2.2 Chang'E-4 Mission & Yutu-2 Rover

Chang’e-4 (CE-4) is a mission by the Chinese National Space Administration, that marked the first rover mission to reach and operate on the far side of the Moon. The mission consisted of a lander, the Yutu-2 rover (Figure 2-11), and the Queqiao relay satellite [53]. Queqiao satellite, launched on May 21, 2018, and entered a halo orbit of the L2 point on June 14. It was the first satellite to establish communication between the Earth and the Moon’s far side

[53]. The CE-4 landing site (177.5991°E, 45.4446°S) is situated on the mare floor of Von Kármán crater within the South Pole-Aitken basin. The Yutu-2 rover deployed onto the lunar surface approximately 12 hours after the landing, on January 3, 2019, at 14:22 UT, and began its scientific operations [54]. The rover's objectives were: 1) to investigate the shallow structure of the selected site of operation, and 2) to study the topography and mineralogical composition of the lunar far side in the same region [55]. Unlike VIPER, its main objective is not targeted on volatiles. Additionally, the selected area of Von Kármán crater is relatively well illuminated [56] that enables the solar powered rover to survive so far.

Yutu-2 initially moved towards a small crater and activated its instruments. The rover followed a planned schedule, entering hibernation during lunar noon to avoid overheating and during lunar night to conserve energy, using radioisotopic heat sources for temperature regulation [54]. It resumed operations on January 29, 2019, and continued this cycle of activity and hibernation as planned. As of January 2025, Yutu-2 remained operational. CE-4 provided invaluable data of the lunar soil properties on the far side and a basis for comparison with data from previous missions like Apollo, Luna, and Chang'e-3, revealing similarities and differences between nearside and far-side regolith [53].

CE-4 shared its design with the previous CE-3 mission. The rovers on both missions weigh 135 kg and feature wheels with a diameter of 30 cm and a width of 15 cm. The rover's body measures 1.1 m ×1.5 m ×1 m, and it is equipped with two solar panels and a dish antenna [54]. Unlike some Apollo and Luna missions, CE-4 and CE-3 lacked dedicated instruments for measuring soil physical properties. However, Yutu-2's Panoramic Camera (PCAM) captured detailed images of the lunar terrain, enabling topographical reconstruction and analysis of soil mechanical characteristics using in situ data [55].

The rover's scientific payloads included the Panoramic Camera (PCAM), the Lunar Penetrating Radar (LPR), and the Visible and Near-Infrared Imaging Spectrometer (VNIS). The PCAM weighs 0.69 kg, has dimensions of 90 × 110 × 120 mm, and consumes 5 W of power [57]. The LPR has a mass of 3.48 kg and a power consumption of 15 W [58]. The VNIS weighs 5.4 kg, consumes 19.8 W of power, and is capable of determining material composition and resource distribution across the rover's operational site on the lunar surface [59].

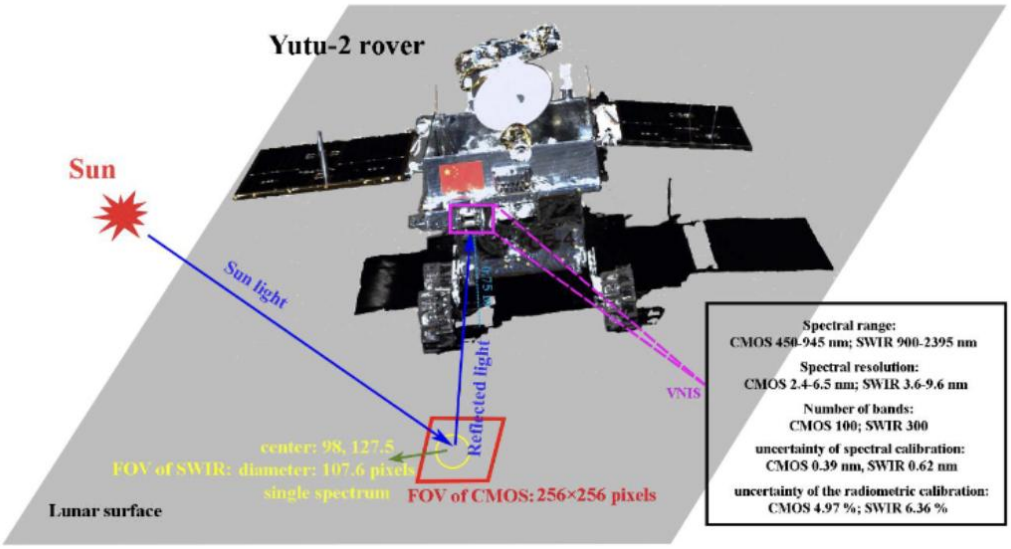

Figure 2-11. Overview of the Yutu-2 rover while operating and the key characteristics of VNIR imaging spectrometer [60].

Payload controllers onboard the rover managed data processing, storage, and task allocation for the scientific instruments [66]. Each payload sensor head featured a dedicated detector circuit board connected to a central payload controller. This controller utilized a high-performance CPU and several field-programmable gate arrays (FPGAs) to meet the processing and control requirements of the scientific instruments. It converted a +28 V bus voltage into secondary voltages (+5 V, +15 V, and +3.3 V) to power the payloads while monitoring voltages and temperatures [55].

The payload controller contained six circuit boards: three for processing, controlling, and storing scientific data and three specifically dedicated to the LPR, VNIS, and PCAM. Data transmission between the payloads and the rover's data manager was facilitated by a 422 bus and LVDS bus. The controller used an 80C32 data processing unit, 256M SDRAM for data storage, and six XQR2V3000-4CCG717 FPGAs to manage and control data from the scientific payloads [55].

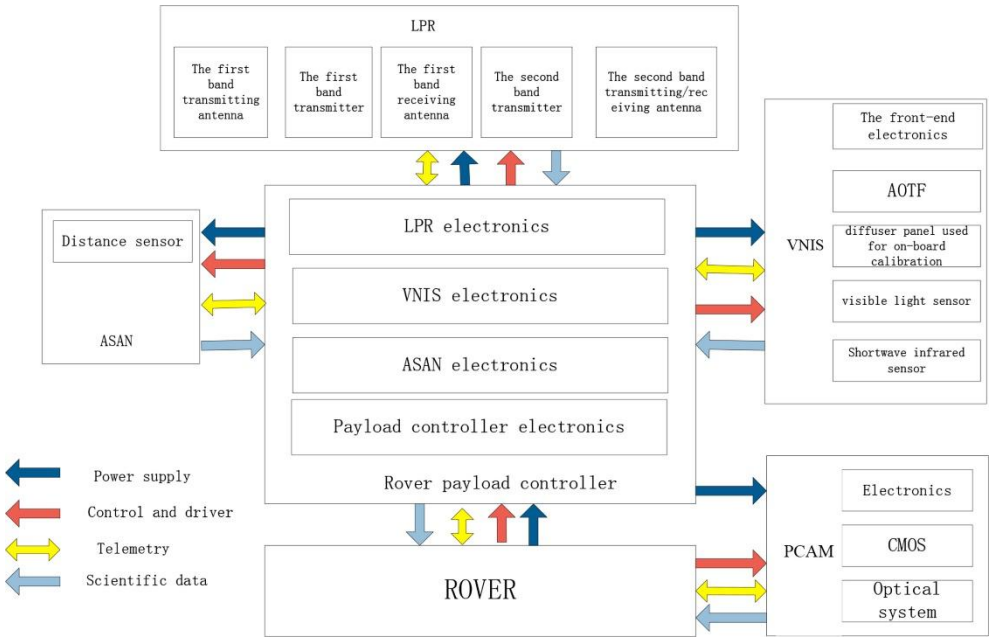

Figure 2-12. Design details of individual instruments of the Yutu-2 rover [55].

2.2.2 Chandrayaan-3 Mission & Pragyan Rover

Chandrayaan-3 was an Indian lunar mission with a primal objective to achieve a soft landing and conducting the first in situ research at a polar region. The mission included a propulsion module, a lander, and a rover, each equipped with payloads designed for in situ scientific experiments [61]. The successful completion of the mission marked India as the fourth country to achieve a soft landing on the Moon and the first to land a spacecraft near the lunar south pole [62]. The landing site was located approximately 350 km from the South Pole-Aitken Basin rim (Figure 2-13) and the total duration of the mission was ten days, concluding on September 2, 2023 [63].

Pragyan's operational lifespan was one lunar day, with a total mass of 27 kg and a power consumption of 50 W [64]. The rover's objectives were: (a) to demonstrate lunar rover technologies and (b) to perform in situ scientific investigations. The Alpha Particle X-ray Spectrometer (APXS) and Laser Induced Breakdown Spectroscope (LIBS) were key payloads on the Pragyan rover (Figure 2-14), designed to identify the elements comprising the lunar surface within the landing site area [65]. The LIBS instrument was compact, lightweight (~1.1 kg), and energy-efficient, consuming no more than 1.2 W of power [65]. A notable feature of the APXS was its use of the radioactive source Cm-244, chosen for its emission of both α-particles (5.8 MeV) and X-rays (14.3 keV and 18.3 keV) as excitation radiation [66]. The rover also featured two Navigational Cameras (Navcam) and one rear camera to support its operations [63].

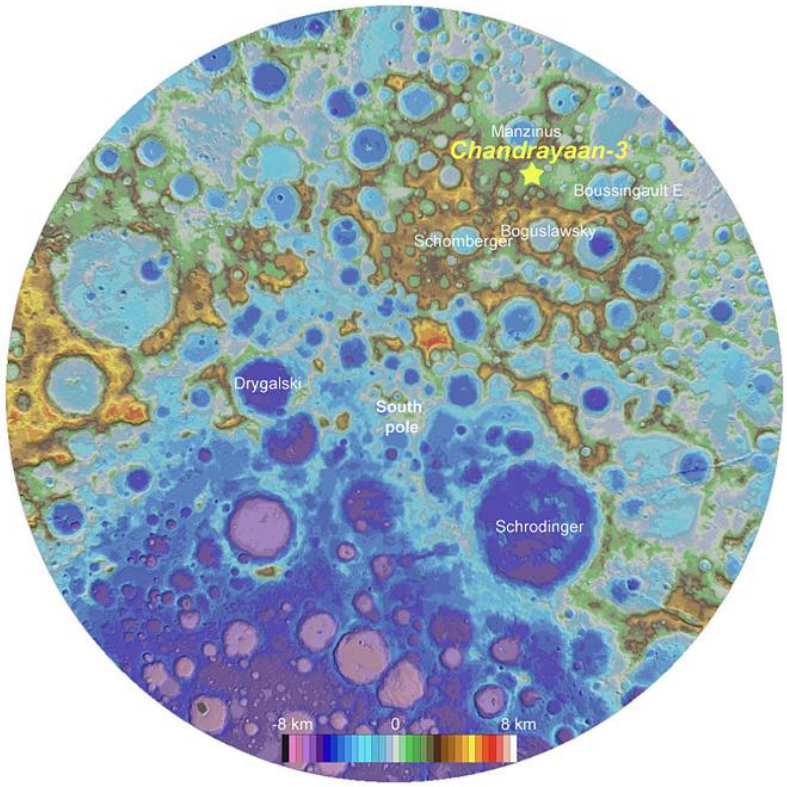

Figure 2-13. The stereographic South Pole Digital Terrain Model (DTM) image from LRO-WAC illustrates the position of the Chandrayaan-3 landing site, which is located in a high elevation area in the South Pole [63].

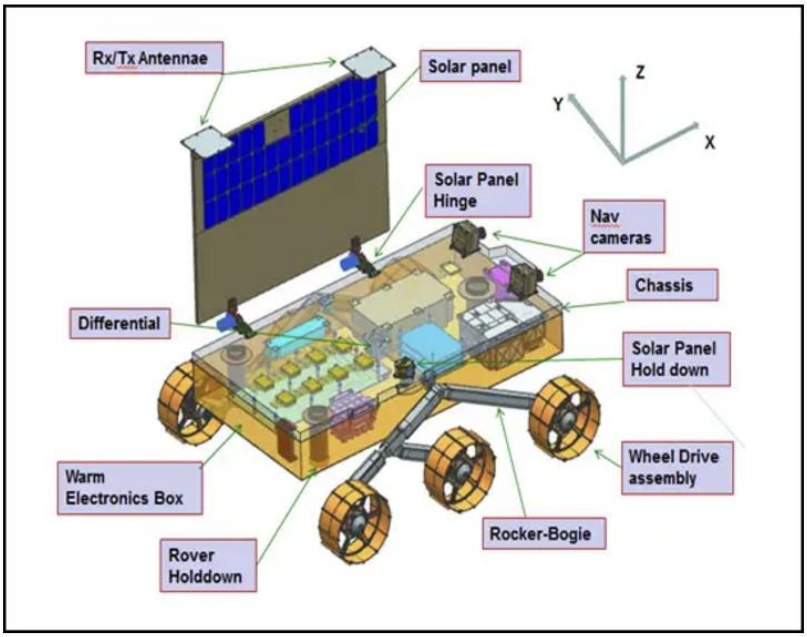

Figure 2-14. Chandrayaan-3 Rover [64].

2.3 Power & Storage Systems for Rover missions

Space power technologies are broadly divided into two primary categories based on their power source. The first category relies on external sources, such as solar power or power beaming, where energy is harvested from the environment. The second category generates power through internal sources, including nuclear fission and radioisotopes, which produce heat that is subsequently converted into electricity [67]. Figure 2-15 provides an overview of these categories. Below, the key power system technologies for rover missions are briefly discussed, including their applications and advantages.

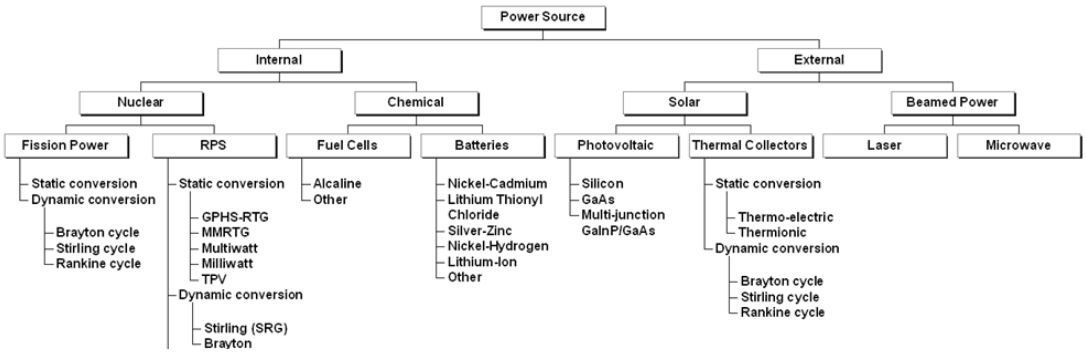

Figure 2-15. Categorization of power sources for rover missions [67].

2.3.1 Photovoltaic Cells

In the 1950s, the advancement of single-crystal photovoltaic solar cells using silicon (Si) and gallium arsenide (GaAs) achieved solar conversion efficiencies close to 6% [68]. By 1958, small-area silicon solar cells had reached a remarkable efficiency of 14% tested in terrestrial conditions, paving the way for the utilization of solar power in spacecraft applications. Photovoltaic arrays, consisting of solar cells for power conversion, became a fundamental technology for space missions.

The size and mass of the photovoltaics increase linearly with power output. Various solar cell technologies are employed, including single-crystal silicon cells, single-junction gallium arsenide cells, and multi-junction solar cells like gallium indium phosphide/gallium arsenide (GaInP/GaAs) [68]. These advanced designs use different parts of the sunlight spectrum, improving conversion efficiency. Typical efficiencies are approximately 14.8–16.6% for silicon, 19–22% for GaAs, and 22–26.8% for GaInP/GaAs [80], with degradation rates of ~3.75%, ~2.75%, and ~0.5%, respectively [69].

Advancements in space solar cell technology continue to prioritize higher efficiency, reduced costs, and improved radiation resistance. Currently, the photoelectric conversion efficiency and enhanced radiation tolerance of triple-junction solar cells, particularly those employing lattice-matched III-V materials, is the primary factor that makes them ideal for space applications [70]. Even though fabrication costs remain high, these cells are widely used across various space missions.

III-V multijunction solar cells are the leading power source for space applications, renowned for their exceptionally high photoelectric conversion efficiency and increased radiation resistance. Regardless their high fabrication costs, they are extensively utilized in various space missions due to their reliability and performance.

Innovations in space solar cell technologies continue to emerge, incorporating advanced materials and novel structures. Crystalline silicon heterojunction solar cells have achieved efficiencies of up to 25.6%, while six-junction inverted metamorphic solar cells hold the world record with a remarkable 47.1% conversion efficiency under 143 suns [70]. Additionally, the production technology for lattice-matched GaInP/GaAs/Ge triple-junction solar cells has significantly matured, enabling large-scale manufacturing while maintaining conversion efficiencies above 30%.

Amongst the key properties of solar cells are their high efficiency, radiation and UV resistance, long operational life, mechanical stress resistance, reliability, and cost-effectiveness. Solar arrays are further evaluated based on specific power, volume, cost, and reliability [69]. Common configurations include body-mounted, rigid, and flexible or deployable arrays, as well as specialized designs such as concentrator, electrostatically clean, and high-temperature arrays. Currently used rover-mounted photovoltaics deliver ~350 W/m^2. For rigid arrays, specific power ranges from 30–60 W/kg with a specific volume of 5–10 kW/m^3, while flexible or deployable arrays achieve 40–80 W/kg and 10–15 kW/m^3, albeit requiring more complex deployment mechanisms [69]

Degradation of solar arrays over time is inevitable, primarily due to temperature fluctuations and radiation exposure. Radiation-induced degradation mechanisms include ionization and atomic displacement, as detailed in Chapter 2.1.3. Traditional mounted photovoltaic systems on rovers, paired with batteries, encounter significant challenges in PSRs. These systems demand disproportionately large battery capacities, which are prone to eventual discharge.

Furthermore, they rely on access to sunlight, potentially stalling missions or limiting site selection to areas with lower scientific returns due to power constraints.

2.3.2 Nuclear Power Generation

Nuclear technologies offer the advantage of an exceptionally high power-to-weight ratio, making them a viable option for long-duration missions, especially on PSRs. For example, [71] suggests the implementation of a radioisotope thermoelectric generator (RTG) for a mission with a potential operational duration of 337 Earth days. Historically, radioactive heaters or RTGs based on polonium-210 (210Po) and plutonium-238 (238Pu) have been utilized. Both isotopes have notable disadvantages, including the high toxicity and short half-life of 210Po, as well as the restricted availability of 238Pu, necessitating the exploration of alternative isotopes.

NASA has developed two Radioisotope Power Systems: the Multi-Mission Radioisotope Thermoelectric Generator (MMRTG) and the Stirling Radioisotope Generator (SRG), both developed to produce approximately 110 W(e) at the beginning of their operational life[71]. The MMRTG, which uses eight General Purpose Heat Source (GPHS) modules with static power conversion, has been used in the 2009 Mars Science Laboratory rover mission. It leverages 30 years of experience in space missions including Voyager, Viking, Galileo, Cassini-Huygens, and Apollo's Lunar Surface Experiment Package (ALSEP) [71].

Improved MMRTG models aim to improve conversion efficiencies from the current ~5.5–6.5% to ~8–10% within the next decade by leveraging advancements in thermoelectric materials. In contrast, SRGs offer significantly higher conversion efficiencies, ranging from the current ~22% to a projected ~32% for next-generation systems [67]. This efficiency allows SRGs to require ~75% less plutonium-238 for the same power output compared to MMRTGs. With a specific power of ~3.3 W/kg, SRGs are lighter than MMRTGs (~2.9 W/kg) but still fall short of the ~5.2 W/kg achieved by the General Purpose Heat Source RTG (GPHS-RTG) [67].

Nevertheless, SRGs are not yet space-qualified, and their long-term reliability remains unproven. They have a g-load tolerance of 30g, compared to the MMRTG's 40g, restricting their use to soft landing missions [71]. Additionally, SRG controller electronics are affected significantly by radiation exposure, necessitating shielding that increases the overall mass. Potential failures, such as the malfunction of one of the two Stirling converters, could unbalance the system and cause complete failure. Electromagnetic interference (EMI) from

SRGs also poses a risk to sensitive scientific measurements, with mitigation strategies like EMI shielding adding both mass and design complexity.

2.3.3 Rechargeable Batteries

Significant advancements have been achieved on rechargeable batteries in the past years, largely influenced by the growth of commercial electronic devices and electric vehicles. Lithium-ion batteries are currently the predominant alternative as they offer high energy density and long cycle life, establishing them the standard for most space systems [72]. Various subtypes of lithium-ion batteries exist, featuring different anode, cathode, and electrolyte chemistries. Key properties for lunar applications include energy density, performance in low and high temperatures, and tolerance to cryogenic conditions when non-operational.

Advanced high-energy-density cells contain lithium nickel cobalt aluminum oxide (NCA) cathodes and graphite or hard carbon anodes, achieving energy densities of up to 260 Wh/kg with operational temperature ranges between -20°C and +60°C. Specialized low-temperature cells, such as those designed by NASA and Yardney/EaglePicher for the exploration of extraterrestrial environments, use ester-based electrolytes and allow discharges at temperatures as low as -65°C [71-74].

Lithium Titanate Oxide (LTO) anodes is a promising alternative for cold environments, which offer advantages in power, safety, and service life. However, LTO batteries typically have lower energy densities than carbon-based anode cells due to their lower voltage. Looking ahead, advancements in lithium metal anodes and sulfur cathodes could achieve an energy density up to 500 Wh/kg and 600 Wh/kg, respectively [72]. While cells of these technologies have been made available commercially, challenges such as limited cycle life, temperature stability, and safety currently prevent their application in space missions.

Passive hibernation is another potential strategy to expand the operational duration of the lunar missions for more than one lunar day. In this approach, the rover would be powered down through the lunar night and reactivated once illumination is available again. This strategy necessitates the system's ability to survive cryogenic temperatures in a non-operational state. While some lithium batteries have demonstrated this capability [72], it remains uncertain whether this applies to other types of battery cells.

2.3.4 Fuel Cells

Fuel cells present a compelling choice for storage by converting hydrogen and oxygen into water, electrical energy, and thermal energy, with a total energy yield of $\Delta G0 = 237.19$ kJ/mol H_2 [72]. Among the various fuel cell designs, polymer electrolyte membrane fuel cells (PEMFCs) are the most viable for compact systems due to their moderate operating temperatures and thin membrane electrode assemblies, which allow for a compact design.

Hydrogen and oxygen stored in a stoichiometric ratio offer an energy content of 13.17 MJ/kg (equivalent to 3660 Wh/kg) [72], which is significantly lower than the 32.4 kWh/kg theoretical energy density of hydrogen when oxygen is freely available from the environment. Storage methods include pressurized gases, cryogenic liquids, or chemically released compounds [88]. Cryogenic storage increases density while reducing pressure, as exemplified by the Space Shuttle's PRSA H2 and O2 tanks [76] which stored hydrogen at 15 bar and 24 K and oxygen at 58 bar and 111 K, yielding a combined theoretical energy density of 2387 Wh/kg. Given that a PEMFC efficiency of 40–50%, the effective electrical energy density drops to 955–1194 Wh/kg [72].

While pressurized gas storage suggests an impractical solution for compact and lightweight rovers, the achievable electrical energy densities are comparable to primary lithium batteries. Also, the released thermal energy generated during operation could prove beneficial for lunar night conditions. The inclusion of peripheral systems such as fluid system, buffer battery, piping, valves, and control mechanisms increases the overall mass [76], [77]. For terrestrial UAV applications, fuel cell energy systems (600–3000 W) typically have mass-to-power ratios of at least 0.5 W/g, though space-grade systems would likely have higher ratios, particularly for smaller setups [72].

Currently, no suitable fuel cell solutions exist for lunar surface applications, leading to their exclusion from this study. However, ongoing developments, especially in regenerative fuel cells, hold promise for future applications in space exploration [78].

2.3 Mass ratio and cost for space missions

Exploring space is inherently costly, requiring high reliability and precise cost estimation. While the specifics of launch systems and landers are beyond the scope of this thesis, a lander is defined here as any vehicle designed to deliver a payload to an extraterrestrial planetary surface, such as the Moon in this case, while a launch vehicle or launch system, as the names imply, is used to carry a spacecraft from the surface of the Earth into space [79].

For the purposes of this research, it is essential to highlight that the primary cost-driving factor in a space mission is the mass of the payload launched and/or landed on a surface (in this case, SELAS). An increase in payload mass necessitates additional fuel, as it raises the final mass of the lander, further amplifying the propellant requirements due to the exponential relationship described by the rocket equation.

Escaping Earth's gravity requires a velocity of 11.2 km/sec (25,000 mph), while a lunar landing demands a total velocity of 13.6 km/sec [80]. Although this increase may seem modest, it dramatically affects the mass ratio, elevating it to 75—almost four times that required for low Earth orbit [80]. This means a launch vehicle designed for missions beyond Earth's gravity, needs to be roughly four times larger than one intended for low Earth orbit.

The estimated mass ratio of the payload to the lander for lunar missions is approximately 200. According to the literature, the cost of accessing space currently ranges from several thousand dollars per kilogram of payload. Delivering a payload to the lunar surface costs an average of $200,000 per kilogram, roughly 25 times the cost of launching a payload to low Earth orbit [80].

2.4 Optimization Algorithms

Optimization is defined as the process of identifying the optimal solution from the set of feasible solutions to a problem, based on the constraints imposed. The problem is typically represented as an objective function, for which the goal is to determine either the global maximum or global minimum, primarily concerning the values of the function's variables that yield the optimal result. Consequently, an optimization algorithm describes a method or a sequence of steps designed to determine the optimal value of the objective function.
The characteristics of an optimization problem, which are considered critical for selecting the most appropriate algorithm, include the following [82]:

- The amount of variables in the objective function.
- The type of variables (continuous or discrete).
- The degree of non-linearity of the objective function.
- The existing constraints.
- The number of extrema (minimum or maximum, based on the characteristics of the problem).
- The number of optimization criteria.

The literature provides a multitude of optimization algorithms and in the subsequent sections, some of the most widely used algorithms will be presented.

2.4.1 Genetic Algorithm (GA)

The Genetic Algorithm (GA) is an evolutionary, stochastic optimization algorithm inspired by Darwin's principles of natural selection and the survival of the fittest. It was first introduced by Holland in 1975 [83].

The algorithm begins by initializing a set of solutions, referred to as chromosomes, represented as strings of symbols. These strings consist of elements called genes, which correspond to values of the parameters in the optimization problem [84]. Each chromosome is evaluated using a fitness function, and those with superior fitness values are selected as parents. The parents exchange the information they have accumulated through a process called crossover, generating new solutions (offspring) in each generation.

While crossover is the primary mechanism for discovering optimal solutions, it is often insufficient because it cannot create new information beyond what exists in the parent chromosomes. To address this limitation, the concept of mutation is introduced, where parameter values in the offspring are randomly altered, enabling the exploration of a broader solution space [85].

The offsprings then replace the parents, initiating another cycle of selection, crossover, and mutation until the termination criterion is met, resulting in the optimal solution, represented by the best chromosome [83].

The performance of a GA depends on several parameters, including the population size of chromosomes, the number of generations (iterations), the crossover rate, and the mutation rate. Increasing the population size and the number of generations enhances the likelihood of finding the optimal solution but also increases computational time [84].

A GA is particularly efficient for applications where the search space is complex or unknown, where mathematical analysis is infeasible, or where the solution space cannot be constrained. However, one limitation of the algorithm is its tendency to converge to local optima rather than global ones. This issue can be mitigated by increasing the diversity of chromosomes [86] or by raising the mutation rate, which is generally much lower than the crossover rate [84]. Finally, the algorithm faces challenges when applied to dynamic datasets [83].

2.4.2 Differential Evolution (DE)

Another algorithm inspired by evolutionary theory was developed by Storn and Price in 1995. It shares similarities with the philosophy of Genetic Algorithms (GA) in that solutions are represented as vectors in a multidimensional space. However, in this algorithm, mutations occur in every gene of the chromosome prior to the crossover process [86]. As the iterations increase, more mutations occur, enhancing the exploration of the search space in pursuit of the optimal solution [87].

The advantages of this algorithm include its simplicity of implementation, as it requires minimal parameter tuning. Additionally, it is generally considered reliable, accurate, and efficient [82].

2.4.3 Firefly (FA)

The Firefly Algorithm, proposed by Yang in 2008, is based on the behavior of fireflies, particularly their bioluminescent light emission. Similar to the Particle Swarm Optimization (PSO) algorithm, fireflies navigate a multidimensional search space, attracted to the optimal solution to the optimization problem so far. This communication is facilitated by the intensity of their light—brighter fireflies represent better solutions.

The fundamental principles of the FA algorithm are as follows [82], [87]:

- Fireflies are not distinguished by gender, so the sole factor driving attraction is the intensity of their light.
- The degree of attraction between fireflies is proportional to the intensity of their light. The light intensity decreases as the distance between two fireflies increases. If two fireflies appear equally bright and attractive, a firefly will randomly choose to move toward one of them.
- The brightness of a firefly depends on the value of the objective function.

As a result, a less bright firefly will always be attracted by a brighter one. This essentially means that it will navigate the solution space toward the optimal region.

2.4.4 Particle Swarm Optimization (PSO)

The philosophy of the Particle Swarm Optimization (PSO) algorithm originates from the study of the behavior of biological communities in their efforts to solve problems, particularly the challenge of locating food. Initially proposed by Kennedy and Eberhart in 1995, PSO follows

the same principles as the collective behavior observed in bird flocks [88]. It serves as the optimization algorithm employed for the problem addressed in this study.

In PSO, each potential solution is considered a point in an N-dimensional search space, referred to as a particle. Each particle is characterized by a fitness value, determined by the objective function. The algorithm begins by initializing a group of random particles, representing random solutions, similar to chromosomes in Genetic Algorithms. However, unlike GAs, each particle is also assigned an initial random velocity, which governs its movement through the solution space [89] as it searches for the optimal solution.
At each iteration, each particle updates its position based on two optimal values:

1. The best value achieved individually so far (personal best, **pbest**).
2. The best value the entire swarm has achieved (global best, **gbest**) [90]

The positions of these best values are defined as follows [91]:

$$pbest(i,t) = arg \min_{k=1,\dots,t} \{f[P_i(k)]\} \tag{2.1}$$

$$\text{while t} \in \{1,2,\dots,N_p\}$$

$$gbest(i,t) = arg \min_{\substack{k=1,\dots,N_p \\ k=1,\dots,t}} \{f[P_i(k)]\} \tag{2.2}$$

where i is the particle index, N_p is the total number of particles, t the iteration number, f the fitness function and P the position of the particle.

After acquiring the optimum values, each particle moves within the multidimensional space by updating its velocity U and position P according to the following equations [91], [92]:

$$U_i(t+1) = \omega \cdot U_i(t) + c_i \cdot r_i \cdot [pbest(i,t) - P_i(t)] + c_2 \cdot r_2.[gbest(t) - P(t)] \tag{2.3}$$

$$P_i(t+1) = P_i(t) + V_i(t+1) \tag{2.4}$$

where ω is the inertia weight, r_1,r_2 are random variables uniformly distributed in the interval $[0,1]$, c_1, c_2 are positive constants known as acceleration coefficients.
The process outlined above is repeated until the termination criterion is satisfied. This criterion is typically defined as either the maximum number of iterations or the attainment of a sufficiently satisfactory value of the fitness function (objective function).

The advantages of Particle Swarm Optimization (PSO) compared to Genetic Algorithms (GAs) are as follows:

- Ease of implementation: PSO requires fewer parameters to be tuned, simplifying its application [93].
- Superior memory capability: PSO retains information about the best solutions found by particles, allowing efficient refinement of positions.
- Effective maintenance of diversity: unlike GAs, where less desirable solutions are replaced by optimal ones, all particles in PSO utilize the positions of the most "successful" particles to improve their own positions [88].

Additionally, PSO is versatile and has a diverse applicability to various optimization problems, making it advantageous compared to other optimization algorithms [94].

3

SELAS Concept Description

As outlined in Chapter 2, the lunar environment—particularly the permanently shadowed regions —presents a formidable challenge for robotic exploration. These areas test the limits of power systems due to their extreme conditions. While nuclear power systems could be a viable solution, they pose potential environmental risks and safety concerns, particularly for rover electronics and during landing procedures. On the other hand, traditional photovoltaic and battery systems, when integrated directly into a rover operating within PSRs, would result in disproportionately large and heavy batteries. These batteries would eventually discharge, necessitating interruptions to the mission for recharging, thereby reducing efficiency and scientific output.

To address these challenges, SELAS is proposed in this diploma thesis as an alternative solution, offering a mobile and sustainable lunar power supply system. SELAS is a solar-powered rover equipped with Li-Ion batteries, designed to harvest energy from areas of perpetual light (described in Chapter 2.1.3) and deliver power to a rover conducting research within PSRs, all without relying on the assistance from a lander. At this stage of the thesis, the specific weight and dimensions of SELAS are yet to be defined, as they will depend on the power requirements determined in Chapter 4 and the optimization process outlined in Chapter 6.

This chapter offers a comprehensive review of the primary functions and characteristics of SELAS, focusing on the key subsystems identified as the most power-intensive contributors to its overall power allocation and budget.

3.1 SELAS Overview

The SELAS system features a four-wheeled traditional rover design, selected for its technological maturity and proven performance in lunar missions, similar to VIPER. This configuration reflects the intent to leverage existing, reliable technologies. SELAS is designed with a top speed of 10 km/h, aligning with capabilities such as the HL-MAPP rover developed by Lunar Outpost [95], [96]. It is also assumed that SELAS navigates autonomously and is not teleoperated. However, a SELAS-lander communication link is established to ensure adequate inspection of its systems by the support crew on Earth or the Gateway, in case of an emergency. Lastly, the charging of SELAS and the rover is achieved through a coupling mechanism, where SELAS connects to the rover using a standard male-female connector design for recharging. This approach was chosen over alternative, untested methods like wireless charging, as suggested in [97]. To avoid any lunar dust deposition and potential malfunctions in the charging process SELAS incorporates the dust tolerant, quick utility connector by Honeybee Robotics [33], [34].

Two distinct configurations will be examined in later chapters: one where SELAS charges a single rover and another where SELAS charges two rovers. SELAS is equipped with a dedicated photovoltaic array and battery stack for its own operational needs (DC BUS 1). Depending on the number of rovers being charged, an additional photovoltaic array and battery stack are allocated for each rover. Further details will be analyzed in the following chapters. The nominal voltage across all buses is maintained at 48 V. DC BUS 1 distributes power to various SELAS payloads and subsystems via a switchboard, which also provides monitoring and line protection. The power architecture of the two configurations is presented in Figures 3-1 and 3-2.

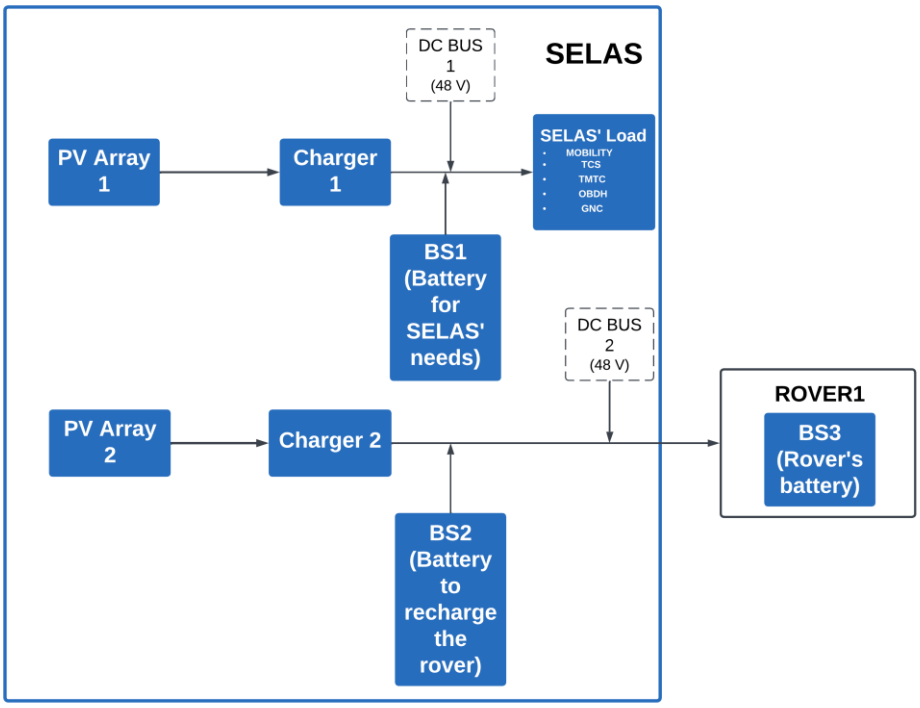

Figure 3-1. Power architecture of the single-rover charging configuration.

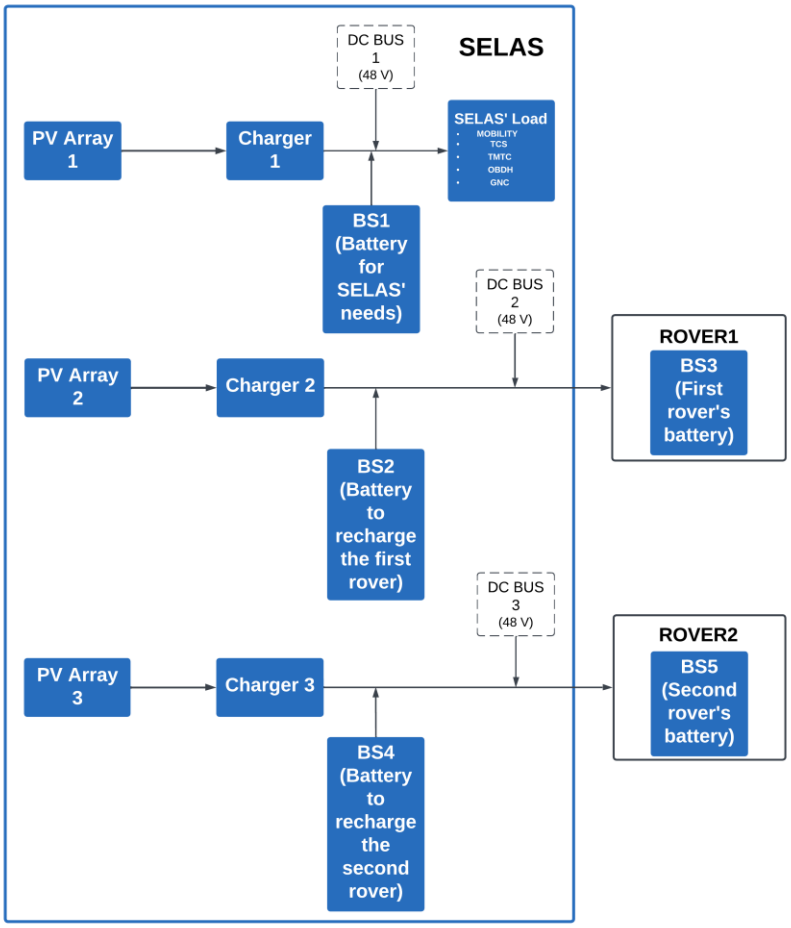

Figure 3-2. Power architecture of the two-rovers charging configuration.

3.1.1 Power Requirements & Power Budget of SELAS

The subsystems of SELAS taken into consideration in the power budget, are Mobility, Guidance Navigation and Control (GNC), On-Board Data Handling (OBDH), Telecommunications (TMTC) and Thermal Control System (TCS). The power requirements analysis for SELAS is grounded in existing literature and insights from lunar and Martian rover missions.

Mobility power consumption has been determined based on the assumption that the specific energy needed for traversing the lunar surface is 0.15 Wh/kg/km, in line with the data obtained from the Apollo lunar rover operations [98], [99]. Assuming a rover with an approximate mass of 60 kg, it would require 90 Wh to traverse 10 km in one hour under normal conditions. An additional margin of 50 Wh is considered for traversing challenging terrains (slopes >15°), bringing the total energy requirement for such conditions to 140 Wh.

Sojourner and the earlier version, Rocky VII [99], provided insight on the power consumption of a simple GNC subsystem approximately with a power consumption of 6 W. MarsFast [100] an ESA Martian rover design provided a modest power consumption of the OBDH system of 25 W.

Regarding the Thermal Control System (TCS), as detailed in [101] and modeled after NASA's VIPER thermal system, the rover is insulated to minimize heat loss to the environment and incorporates mechanisms for controlled heat rejection when internal heat production exceeds the required levels to maintain the desired operating temperature.

To address design uncertainties, the inclusion of a small 2W heater on each wheel during operation was considered, adding a total of 15W to the thermal system's requirements. Additionally, a rover of VIPER's size generates approximately 221.5W of heat from its electronic systems. Although SELAS is anticipated to be smaller, this level of heat generation is expected to be sufficient to maintain its systems within the required temperature range.

The core elements of the thermal system are the following:

- Radiator Panel with Louvers: facilitates the removal of heat generated by the electronics.
- Heat Pipes and Cold Plates: transfers heat from the electronic packages to the radiator for dissipation.

- Multi-Layer Insulation (MLI): provides thermal insulation for the electronics and acts as a barrier, preventing the excessive heat from the DRPS (Dynamic Radioisotope Power System) from reaching the surface ahead of the rover.
- Heaters: maintains temperatures when external conditions are too cold.
- Temperature Sensors, Controllers, Switches, and Data Acquisition Systems: monitors and regulates the thermal system to ensure efficient operation. Lastly, [102] provides an approximation of the power consumption of the TMTC system for simple rover-to-lander telecommunications, around 9 W.

The breakdown of the estimated power allocation, accounting for a rover with a total mass of 60 kg, operating at a speed of 10 km/h during both nominal and demanding traverses, is outlined in Tables 3-1 and 3-2, respectively.

Table 3-1. SELAS' projected electric power budget breakdown on nominal traversing.

System	Power (W)
Mobility	90
TCS	15
TMTC	9
OBDH	25
GNC	6
Total	145

Table 3-2. SELAS' projected electric power budget breakdown on peak traversing.

System	Power (W)
Mobility	140
TCS	15
TMTC	9
OBDH	25
GNC	6
Total	195

In subsequent chapters, it will be detailed that SELAS enters a hibernation mode to survive potential periods of complete darkness. During this mode, only essential systems remain operational, including the Thermal Control System (TCS) to maintain necessary internal temperatures and the On-Board Data Handling (OBDH) system to run critical algorithms and prepare SELAS for resumption of activity when favorable illumination conditions return. Additionally, while SELAS is charging the rover, it is assumed to consume power equivalent to its hibernation mode since the OBDH system remains the primary power consumer. The power budget for SELAS during both hibernation and charging modes is outlined in Table 3-3.

Table 3-3. SELAS' projected electric power budget breakdown on hibernation & charging mode.

Utility	Power (W)
Mobility	0
TCS	15
TMTC	0
OBDH	2
GNC	0
Total	17 W

4

Modelling of SELAS

The solution proposed in this thesis is based on the premise that, unlike Earth, building a grid spanning several kilometers to support charging stations for robotic and pressurized rovers is unfeasible on the lunar surface. Instead, the proposed concept introduces a system of mobile charging stations designed to deliver electric energy to any location on the Moon. This approach significantly enhances the operational capabilities of robotic rovers, particularly those functioning in PSRs, where traditional charging methods are either impractical or limit the mission's success.

SELAS relies entirely on environmentally sustainable and proven technologies that have been tested extensively in both terrestrial and space environments. Its power generation utilizes triple-junction solar cells, energy storage is managed with Li-Ion batteries, and battery chargers. All components are commercially available and specifically engineered for space applications, ensuring reliability while performing in the Moon's harsh environment along with a realistic design.

To assess the functionality of SELAS and optimize its performance, a comprehensive simulation was conducted using MATLAB. This process required the development of mathematical models to represent each subsystem accurately. The following sections detail the modeling approach, starting with the sun-tracking system and the calculation of solar illumination received by the photovoltaics at each charging point, along with the ambient temperature of the lunar environment. Next, the modeling of the photovoltaics and batteries is explained, followed by an overview of the traverse calculation algorithm.

4.1 Angle of Incidence, Tilt Angle & Collected Irradiance

The intensity of solar irradiance is heavily affected by local time of a lunar day and the geographical location [104]. For example, during sunrise and sunset, the sun appears at the horizon. Understanding the sun's position at any given time during the lunar day is, therefore, critical for accurately assessing solar irradiance intensity and planning energy generation systems.

Two critical parameters for determining the illumination incident on photovoltaic panels are the solar elevation and azimuth angles. The solar elevation angle measures the height of the sun above the local horizon directly beneath its position in the sky. It is determined by factors such as the local latitude, time of day, and the declination angle. Similarly, the solar azimuth angle describes the sun's position in the sky projected onto the horizontal plane, measured relative to either the north or south direction. This angle also depends on the local latitude, time of day, and declination angle. At each iteration of the simulation, which is explained further in subsequent chapters, the values for both the solar elevation and azimuth angles are obtained from NASA's moon map. [103].

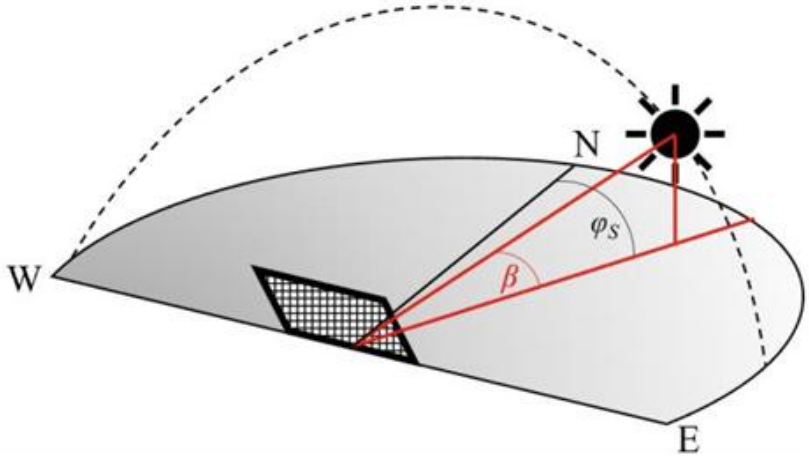

Figure 4-1. The solar elevation and azimuth angles, determined by the sun's position in the sky [104].

The horizontal irradiance, calculated for a surface tilted at 0°, depends on the angle of incidence of the incoming solar radiation. This angle of incidence is influenced by various factors related to the sun's position and the orientation of the surface under consideration. Mathematically, the angle of incidence can be determined using a specific expression, which accounts for these parameters [104]:

$$\theta = cos^{-1}[\cos\beta\cos(\varphi_s - \varphi_C)\sin\Sigma + \sin\beta\cos\Sigma] \quad (4.1)$$

where Σ represents the tilt angle of the surface, ϕ_C the azimuth of the surface in horizontal orientation, β is the solar elevation angle and φ_s the solar azimuth angle.

The intensity of net irradiance received by a horizontal surface is influenced by the angle of incidence θ [104]:

$$I_{BH} = I_B\cos\theta = I_B\sin\beta \quad (4.2)$$

where I_B is the total solar radiation received on the lunar surface which is equivalent to the intensity of the solar radiation just outside Earth's atmosphere, measured at 1361 W/m^2.

For the purposes of this thesis, both horizontal and vertical tracking mechanisms were implemented for the solar collector surface. Horizontal tracking entails adjusting the collector azimuth angle ϕ_C to optimize the angle of incidence (θ) at every time interval. Analyzing equation (4.1), it becomes evident that to minimize θ by controlling ϕ_C, the collector azimuth angle must match the solar azimuth angle ϕ_S during all time intervals. This ensures the horizontal projection of the sun's position in the sky is perfectly aligned with the surface. Assuming ideal horizontal tracking, where ϕ_C equals ϕ_S, equation (4.1) simplifies to the following expression [104]:

$$\theta = cos^{-1}[\cos\beta\sin\Sigma + \sin\beta\cos\Sigma] \quad (4.3)$$

Using trigonometric identities, this expression can be simplified to the following form:

$$\theta = cos^{-1}[\sin(\beta + \Sigma)] \quad (4.4)$$

Considering the vertical tracking, inspection of (4.3) indicates that to further optimize θ, the tilt Σ should complement the solar altitude angle β, meaning that,

$$\Sigma = 90° - \beta \quad (4.5)$$

As described in (4.1), the angle of incidence on a surface depends not only on the sun's position in the sky but also on the surface's horizontal and vertical angular orientation. Furthermore, for a tilted surface (where the tilt angle $\Sigma \neq 0$), the total irradiance I_C received includes both direct sunlight I_{BC} and irradiance I_{RC} reflected from surrounding surfaces, in this instance, the lunar ground. All irradiance values are in W/m^2. The collected irradiance can be expressed as follows [104]:

$$I_C = I_{BC} + I_{RC} \quad (4.6)$$

with $$I_{BC} = I_B \cos\theta \quad (4.7)$$

$$I_{RC} = \rho I_{BH} \frac{1-\cos\Sigma}{2} \quad (4.8)$$

where ρ corresponds to the ground reflectance, which based on the followed model it is assumed to be equal to 0.2.

4.2 Ambient Temperature of the Lunar Environment and the Photovoltaic Cell Temperature

The energy production curves of photovoltaics on the lunar surface are influenced by the levels of solar irradiance and ambient temperature at specific sites. Unique lunar surface conditions create a direct correlation between ground temperature and solar radiation intensity [105]. As a result, accurately characterizing ground irradiance profiles is essential for estimating ambient temperature variations and corresponding PV power generation capacities. The energy absorbed by materials is directly linked to their temperature increase. While only some of the absorbed energy on the lunar surface originates from solar radiation, the temperature is predominantly influenced by it. This is largely due to the absence of an atmosphere, which eliminates mechanisms like convection and conduction with surrounding gases or winds. This lack of atmospheric heat exchange means the lunar surface's thermal response is primarily dictated by direct solar irradiance and the material properties of the regolith, including its thermal conductivity, specific heat, and albedo [106].

The following formula establishes the relationship between lunar ambient temperature and horizontal irradiance [104]:

$$T_a = (T_{a,max} - T_{a,min}) \cdot \left(\frac{I_{BH} - I_{BH,min}}{I_{BH,max} - I_{BH,min}}\right) \quad (4.9)$$

where $I_{BH,min}$ and $I_{BH,max}$ are the values of the minimum and maximum horizontal irradiance in W/m^2 and $T_{a,min}$ and $T_{a,max}$ are the minimum and maximum ground temperatures of the location in K.

While ambient temperature influences PV cell temperatures, these two are not equivalent. In many cases, PV cell temperatures can significantly exceed ambient temperatures, especially in configurations designed to maximize solar irradiance exposure. This effect is particularly pronounced in polar regions, where the ground may receive solar radiation at less direct angles, leading to a notable temperature difference between the PV panels and the surrounding ground.

Based on the model presented at [104], the temperature of the photovoltaic cells is given by a fourth-degree function expressed as follows:

$$0 = A_\sigma \left[\left(\frac{1-\cos\Sigma}{2}\right)\varepsilon_\alpha {T^4}_\alpha - \varepsilon_{cell}{T^4}_{cell}\right] + \alpha_{cell} I_C A - \frac{I_C}{I_{Cref}} \cdot \left[1 - \gamma_{ref}\left(T_{cell} - T_{ref}\right)\left(T_{cell} - T_{ref}\right)\right] \quad (4.10)$$

where α_{cell} is the PV cell absorptivity, A is the PV cell surface area in m^2, σ is the Stefan-Boltzmann constant (5.669 x 10^{-8} W/(m^2K^4)), ε_α is the emissivity of the surroundings (i.e., the lunar ground), T_a is the temperature of the surroundings (i.e., ambient temperature) in K and ε_{cell} is the PV cell emissivity. In our case, for the 32.2% XTE-SF (Standard Fluence) Space Qualified Triple Junction Solar Cell by SpectroLab, α_{cell} and ε_{cell} equal 0.9 and 0.85, respectively [107].

4.2 Modelling of the Photovoltaic Module

Given the customization required for many mission-specific products, finding a readily available photovoltaic panel designed for space applications presented a challenge. Therefore, a photovoltaic panel has been opted utilizing the SpectroLab 32.2% XTE-SF Space Qualified Triple Junction Solar Cell [107]. Assuming we have 108 cells per photovoltaic module ($N_{ser} = 18\ cells$ and $N_{par} = 6\ cells$). Based on the datasheet, 1 cell is 2.27 g ($84\ ^{mg}/_{cm^2}$) and 27 cm^2. The value of $I_{sc,cell}$ tested in AM0 conditions, equals to $18.6\ ^{mA}/_{cm^2}$ corresponding to $I_{sc,cell} = 0.502\ A$ and similarly $I_{mp,cell} = 0.483\ A$. Based on these, each panel would have a total area of 0.2916 m^2, while the weight of the photovoltaic cells alone would be 0.245 kg. Based on the areal density of commercially available photovoltaic panels for space applications [108], [109] which utilize similar cells in size and mass to those employed in this thesis, an average value of 4 kg/m² can be assumed for the total mass of the panel. This estimation accounts for the inclusion of mounting frames and deployment mechanisms. Consequently, for a panel with an area of 0.2916 m², the total mass is calculated to be approximately 1.16 kg, Based on Figure 4-2 and the aforementioned analysis, the panel exhibits the following values in AM0 conditions:

$$I_{mp} = 2.89\ A \quad (4.11)$$

$$I_{SC} = 3\ A \quad (4.12)$$

$$V_{OC} = 48\ V \quad (4.13)$$

$$V_{mp} = 43.83\ V \quad (4.14)$$

where I_{mp} and V_{mp} is the current and the voltage of the panel at maximum power, I_{SC} is the short-circuit current and V_{OC} is the open-circuit voltage.

XTE-SF Post 1 MeV e- Retention (European standard-ECSS)**

Parameters*	BOL	1e14 (10-yr LEO)	5e14	1e15 (15-yr GEO)	1e16
$Efficiency_{mp}$	32.2%	0.93	0.89	0.87	0.72
V_{oc} (V)	2.750	0.93	0.90	0.88	0.80
J_{sc} (mA/cm^2)	18.6	1.00	1.00	0.99	0.96
V_{mp} (V)	2.435	0.93	0.90	0.87	0.79
J_{mp} (mA/cm^2)	17.9	1.00	1.00	0.99	0.91

Figure 4-2. SpectroLab 32.2% XTE-SF (Standard Fluence) Space Qualified Triple Junction Solar Cell specifications tested in AM0 (135.3 mW/cm^2, 28ºC), for 27 cm^2 cell size [107].

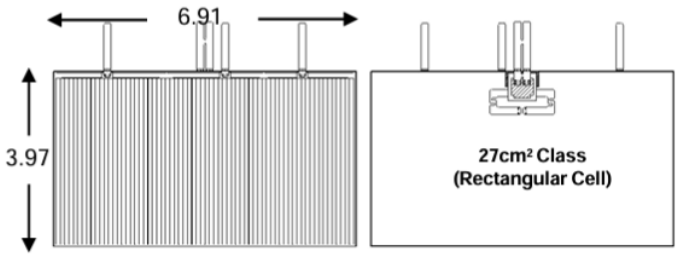

Figure 4-3. SpectroLab 32.2% XTE-SF (Standard Fluence) Space Qualified Triple Junction solar cell dimensions [107].

According to the model outlined in [110], determining the output power of the photovoltaic generator requires calculating additional parameters of the cell within the generator under standard test conditions (STC). The generated power of an individual cell is determined by the established relationship between the fill factor and the open-circuit voltage. The normalized voltage and resistance are defined as follows:

$$v_{oc} = \frac{V_{OC}}{V_t} \tag{4.15}$$

$$r_s = \frac{R_s}{V_{OC}/I_{SC}} \tag{4.16}$$

where V_t (V) stands for the thermal voltage and is given by the following expression:

$$V_t = \frac{kT}{q} \tag{4.17}$$

Also, k is the Boltzman constant $(1.38 \times 10^{-23}\ J/K)$, T is the absolute temperature in Kelvins and q is the charge of the electron $(1.602 \times 10^{-19}\ C)$. For $T = 300\ K$, $V_t = 25\ mV$. A satisfactory empirical expression for the relationship is:

$$FF = \frac{V_M I_M}{V_{OC} I_{SC}} = FF_O(1 - r_s) \tag{4.18}$$

The value of FF_O is given from the following expression:

$$FF_O = \frac{v_{oc} - ln(v_{oc} + 0.72)}{v_{oc} + 1} \tag{4.19}$$

Using the previously outlined calculations, the series resistance of the solar cells, which is a property independent of operating conditions, can be determined as follows:

$$R_S = \left(1 - \frac{F}{FF_o}\right)\frac{V_{OC}}{I_{SC}} \tag{4.20}$$

From equations (4.17) and (4.18), the maximum output power of each panel, based on the maximum output power of an individual cell, can be determined as follows:

$$P_{max,cell} = \frac{P_{max,panel}}{N_{SM} N_{PM}} \tag{4.21}$$

$$V_{OC,cell} = \frac{V_{OC,panel}}{N_{SM}} \tag{4.22}$$

$$I_{SC,cell} = \frac{I_{SC,panel}}{N_{PM}} \tag{4.23}$$

Given the various operation conditions met at the lunar surface, we follow the assumptions from the model outlined in [110] considering the relationship between I_{SC} and V_{OC} of the solar cell and the solar irradiance G and solar cell temperature T_C respectively:

$$I_{SC} = C_1 G \tag{4.24}$$

where the constant C_1 has the value:

$$C_1 = \frac{I_{SC}(100\ mW/cm^2)}{100\ mW/cm^2} \tag{4.25}$$

The value of V_{OC} of the photovoltaic module is influenced by the temperature of the solar cell T_c. In our case, this value is given by (4.10).

In the range of operating conditions encountered it holds that:

$$\frac{dV_{OC}}{dT_c} = -2.3\ mV/°C \tag{4.26}$$

During the simulation of SELAS operation, R_S is determined under STC using the values derived from equations (4.15) through (4.19). Subsequently, for each operating instance defined by G and T_c, the values of I_{SC} and V_{OC} are computed using (4.24) and (4.26), alongside

the parameters from equations (4.15) - (4.19). These calculations ultimately lead to determining the module's maximum power output as specified by equation (4.21).

Each photovoltaic module of SELAS consist of N_s photovoltaic panels connected in series and N_p photovoltaic panels connected in parallel. To ensure safe battery charging and to optimize the power output, a photovoltaic battery charger is integrated with the module. This charger employs the Maximum Power Point Tracking (MPPT) technique to maximize power production. The value of N_p is determined using the following equation:

$$N_p = floor\left(\frac{P_{CH}}{N_s \cdot V_{M,STC} \cdot I_{M,STC}}\right) \tag{4.27}$$

where $P_{CH}(W)$ represents the nominal power of the photovoltaic battery charger, and $V_{M,STC}\ (V)$, $I_{M,STC}(A)$ are the voltage and current of each photovoltaic panel at the MPP under STC. These parameters are typically provided in the datasheets supplied by the manufacturers of the battery charger and photovoltaic panels.

Additionally, for the photovoltaic charger to function correctly, it is essential that the input voltage from the photovoltaic module $V_{MPPT,PV}(t)$ for any given moment t, falls within the operational voltage range specified by the charger:

$$V_{MPPTmin,charger} \leq N_s \cdot V_{MPPT,PV} < V_{MPPTmax,charger} \tag{4.28}$$

Also, if $V_{MPPT,PV}(t) < V_{MPPTmin,charger}$ then the output power of the photovoltaic source is set to zero for that given t.

4.3 Battery Model

In all configuration scenarios, whether SELAS is designed to charge a single prospecting rover or multiple rovers, all battery stacks in both SELAS and the rover adhere to the model outlined in this section. Let r represent the total number of rovers being charged by SELAS and i represent the index of the rover ($i = 1,2,3, \ldots . r$). The battery stack on SELAS meant to charge the i-th rover is BS_{2i} while the battery stack on the i-th rover being charged by SELAS is BS_{2i+1}. SELAS' operational needs are always supported by a dedicated battery stack, referred to as BS_1. A photovoltaic array of $N_{s,PVsBS1}$ panels in series and $N_{p,PVsBS1}$ panels in parallel, is charging BS_1 and a number of r photovoltaic arrays, each one with $N_{s,PVsProsp}$ number of photovoltaics in series and $N_{p,PVsProsp}$ number of photovoltaics in parallel, are charging the BS_{2i} batteries. Each photovoltaic array i is connected to one BS_{2i} and one charger. Lastly, it is assumed that all BS_{2i} battery stacks are of equal size, as are all BS_{2i+1}.

In the most basic configuration, SELAS is equipped with two distinct battery stacks, BS1, which is specifically dedicated to meeting SELAS' operational requirements such as heating, communication, and traversal, and the other, referred to as BS_2, designed specifically to store energy for charging the rover and its battery stack (BS_3). On SELAS, each battery stack is paired with a photovoltaic module, consisting of Ns and Np photovoltaic panels as described in Chapter 4.2. A dedicated charger is connected to each module, managing the charging process for its respective battery stack. The maximum discharging current and therefore the discharging power of each BS is dictated by the maximum discharge current that the charger can handle and the power demands of the rover r. The energy produced by each photovoltaic module $E_{TOTAL,PVs}$ is directed entirely to the respective battery stack. The power architecture of SELAS is depicted in Figure 4-4.

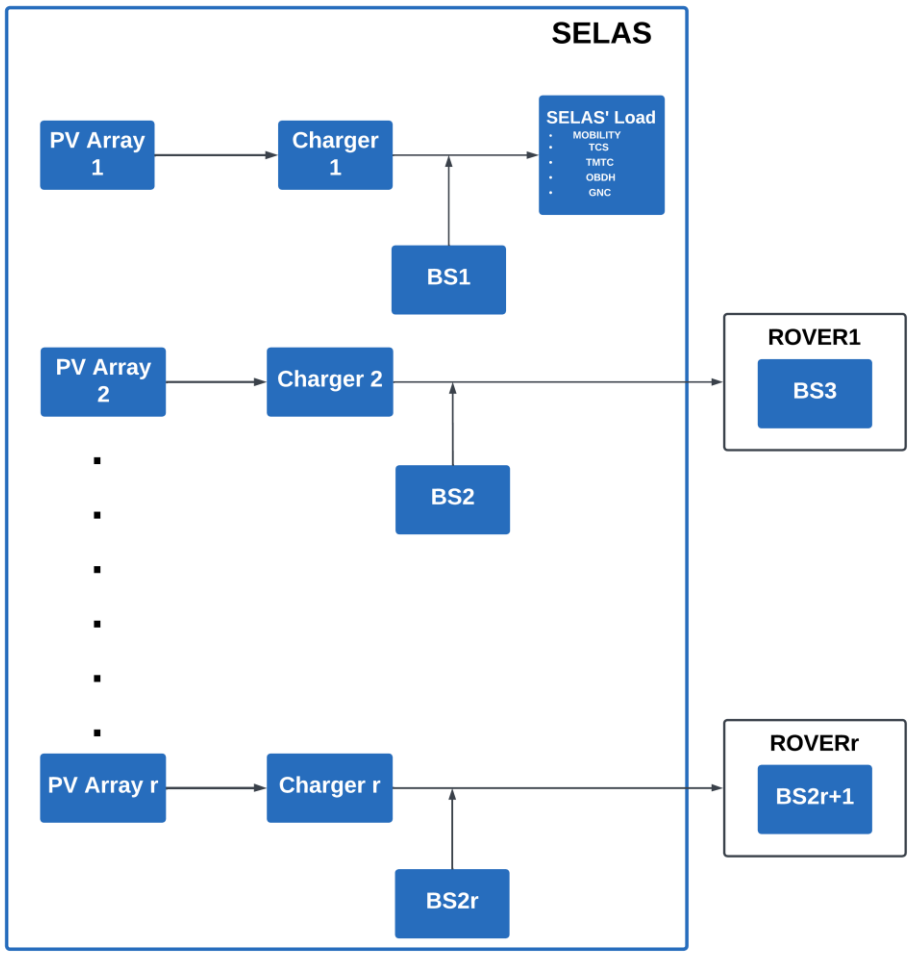

Figure 4-4. Power architecture of SELAS.

The batteries utilized in all the battery stacks discussed in this thesis are assumed to be the EaglePitcher 43 Ah high-energy, long-cycle-life, low-maintenance Li-Ion cells, designed for space applications. The nominal cell weight is 1.27 kg and its specific energy is 154 Wh/kg. Its maximum constant current is 200 A and the nominal voltage of each cell is 3.6 V [111].

The same rules were followed for all BS, meaning that, each battery stack contains multiple battery elements connected in parallel, $N_{s,p}$ and each element contains $N_{s,b}$ batteries in series. Their values are calculated as follows:

$$N_{s,b} = ceil\left(\frac{V_{BUS}}{V_B}\right) \tag{4.29}$$

$$N_{s,p} = floor\left(\frac{N_{BAT}}{N_{s,b}}\right) \tag{4.30}$$

where V_{BUS} (V) is the voltage level of the output of the photovoltaic charger, V_B (V) denotes the nominal voltage of each individual battery and N_{BAT} represents the total number of batteries, determined as an outcome of the optimization algorithm.

All battery stacks are restricted to being discharged only to a limited extent, ensuring that the output voltage of the batteries remains largely unaffected, as depicted in Figure 4-5:

$$SoC_{min} = 20\ \% \tag{4.31}$$

$$SoC_{max} = 100\ \% \tag{4.32}$$

It is assumed that all battery stacks are fully charged at the commencement of the operation, with the initial SoC set to 100%.

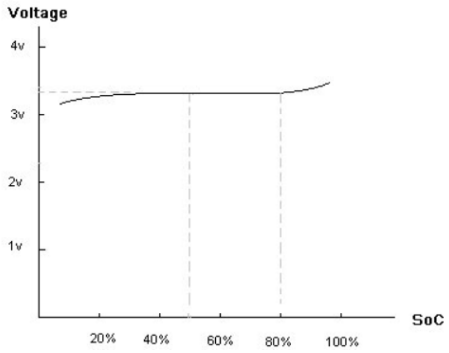

Figure 4-5. Voltage vs. State of Charge in Li-ion batteries [113].

Consequently, the minimum and maximum energy level, E_{min} and E_{full}, respectively, in Wh for each of the battery stacks is calculated as:

$$E_{min} = SoC_{min} \cdot E_{full} \tag{4.33}$$

$$E_{full} = N_{bat} \cdot C \tag{4.34}$$

with C being the nominal capacity of each battery in Wh.

The remaining energy of the battery stacks at any given moment, $E_{lev}\ (t)\ (Wh)$ is calculated using the following equation:

$$E_{lev,t} = SoC(t) \cdot E_{full} \tag{4.35}$$

Here, $SOC(t)$, represents the state of charge of the battery in time instant t.

It is also assumed that the energy needed, $E_{need}(t)(Wh)$, for a discharged battery, fully or partially, with an energy level $E_{lev}(t)$ at any given time t, to reach SOC_{max} is:

$$E_{need}(t) = E_{full} - E_{lev}(t) \tag{4.36}$$

If a BS is in charging mode then the incoming energy $E_{in}(t) = E_{TOTAL,PVs}$ has a positive value, leading to the following two scenarios.

If $E_{in}(t) \geq E_{need}(t)$ then:

$$E_{lev}(t+1) = E_{lev}(t) + E_{need} \tag{4.37}$$

In this case, the calculation of $\mathrm{E_{need}(t)}$ makes sure that there is no overcharge of the BS.

If $E_{in}(t) < E_{need}$ then

$$E_{lev}(t+1) = E_{lev}(t) + E_{in}(t) \tag{4.38}$$

In this case, the $\mathrm{SoC_{max}}$ is not achieved, and the battery stack absorbs any given energy available from the photovoltaics.

If BS is in discharging mode, $E_{req}(t)$ represents the energy required from the stack and $E_{out}(t)$ denotes the energy the battery is capable of supplying based on its available reserves.

If $E_{lev}(t) - E_{req}(t) < E_{min}$ then:

$$E_{lev}(t+1) = E_{min} \tag{4.39}$$

$$E_{out}(t) = E_{lev}(t) - E_{min} \tag{4.40}$$

In this case, the battery stack ensures energy provision until it reaches the minimum threshold SOC_{min}, meaning the required energy $E_{req}(t)$ is not fully supplied.

If $E_{lev}(t) - E_{out}(t) \geq E_{min}$ then:

$$E_{lev}(t+1) = E_{lev}(t) - E_{req} \tag{4.41}$$

$$E_{out}(t) = E_{req}(t) \tag{4.42}$$

In this case, the battery stack ensures full energy provision, meaning that $E_{req}(t)$ is fully supplied.

4.4 Traverse Algorithm

As mentioned before, SELAS takes advantage of the illuminated points around the area of interest in order to recharge and then re-supply the rover with energy. Along with the power flow, there is an additional traverse algorithm that is designed to determine the daily charging schedule prior to the initiation of the simulation. During the simulation, it identifies the next charging point for SELAS and selects the corresponding illumination time-series necessary for charging the photovoltaic modules. In turn, the power flow models the energy transfer between the photovoltaic modules and the battery stacks, as outlined in previous sections, and calculates the SoC of each battery stack at every simulation time step. This SoC data is subsequently provided to the optimization algorithm to verify whether the optimized values satisfy the SoC constraints, as will be elaborated in Chapter 6. The simulation framework for SELAS is presented in Figure 4-6.

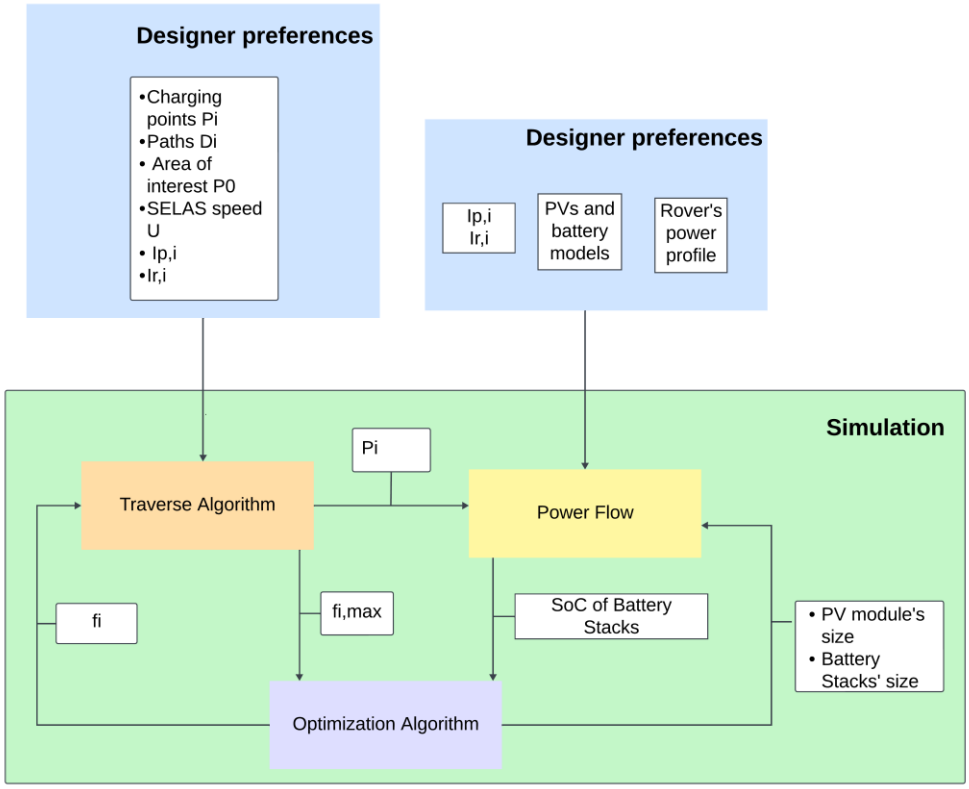

Figure 4-6. Simulation framework for SELAS.

Specific inputs are required for this traverse algorithm, in order to function effectively. These include the charging point P_0, which is the designated area where SELAS must travel to recharge the prospecting rover and the place where the latest conducts its activities (the PSR in our case). Additionally, as an input the algorithm must know the nearest n illuminated

points $P_i, \forall i \in N,\ 0 < i < n$ along with the illumination $I_{p,i}(t)$ received by the PV arrays at each point which is calculated from the elevation angle $\beta_p(t)$ and azimuth angle $\varphi_{s,p}(t)$ for any given moment $t \in N \cap [1,8760]$, , as described in paragraph 4.1. Furthermore, the traverse algorithm details about the paths R_i and their lengths D_i (km), which connect P_0 to each P_i as well as the illumination $I_{r,i}(t)$ of each path, calculated by the elevation angle $\beta_r(t)$ and the azimuth angle $\varphi_{s,r}(t)$. Lastly, the rover's speed U is also required.

Based on the aforementioned inputs, for each point P_i, the algorithm calculates the maximum daily charging frequency $f_{i,max}$ based on its unique travel time $t_{traverse,i}$, and the minimum interval $l_{i,min}$ required between two consecutive charging sessions:

$$t_{traverse,i} = \frac{2D_i}{U} \tag{4.43}$$

$$l_{i,min} = t_{traverse,i} + d + 1 \tag{4.44}$$

$$f_{i,max} = floor\ (\frac{24}{l_{i,min}}) \tag{4.45}$$

The duration d of each charging session is an essential input, representing the time SELAS spends at P_0 to recharge the rover. In all scenarios simulated in this thesis, d is set to 1 hour, which is considered the minimum required time. Additionally, the "+1" term in (4.44) represents the minimum duration of one hour that SELAS must spend at P_i to recharge its own batteries fully or partially. The final values of f_i are an output of the optimization algorithm having a maximum value equal to $f_{i,max}$.

For each f_i the algorithm calculates different hours of charging throughout the day, accounting for the varying traverse times due to the differences in distance of P_i from P_0. Each $h_{i,j}$ represents the specific hour of the day when SELAS must be at P_0 to recharge the rover. This timing depends on the particular P_i being used for SELAS' recharging, resulting in a unique schedule of $h_{i,j}$ hours for each P_i where $i \in \{1,2, \dots n\},\ j \in \{1,2, \dots f_i\}$.

Once the charging schedule is finalized by the traverse algorithm, then the simulation is initiated. When SELAS is at P_0 and the charging session is complete, the traverse algorithm determines the next point for SELAS to travel to for recharging. To make this decision, the algorithm evaluates the illumination conditions at all available points P_i. For a point P_i to be considered a valid charging location, its illumination $I_{p,i}(t)$ must be greater than zero:

$$I_{p,i}(t) > 0 \tag{4.46}$$

Among all points P_i that satisfy the illumination condition, the point with the minimum distance D_i from P_0 should be selected first:

$$P_{selected} \in \{P_1, P_2, \dots, P_n\} \tag{4.47}$$

$$P_{selected} = \text{argmini}\{D_i \mid \mathrm{I}_{p,i}\,(\mathrm{t}) > 0\} \tag{4.48}$$

It is worth mentioning that the selection of the illuminated point focuses on minimizing the distance rather than choosing the point with the most favorable illumination conditions. This prioritization is made to expedite the charging process and reduce SELAS' exposure to potentially extreme conditions for extended durations.

While travelling a distance D_i to reach $P_{selected}$ on the R_i path, SELAS also recharges its PVs through $I_{p,i}(t)$. SELAS reaches the selected point $P_{selected}$ and recharges its batteries (fully or partially according to paragraph 4.3). According to the charging schedule, if SELAS is required to return to P_0 at hour $h_{i,j}$ it must depart from $P_{selected} = P_i$ at the time calculated as:

$$k_{i,j} = mod\{h_{i,j} - 1 - U \cdot Di, 24\} \tag{4.49}$$

This ensures that SELAS arrives at P_0 precisely as scheduled, avoiding unnecessary delays or early arrivals. If SELAS fully recharges its batteries before the scheduled hour $k_{i,j}$ it remains at $P_{selected}$ and awaits until $k_{i,j}$ arrives.

Upon returning to P_0, SELAS recharges the prospecting rover for a duration of d hours (1 hour in our case). Once this charging session is complete, the algorithm cycles through its process again, ensuring continuous operation and adherence to the charging schedule.

If there is no illumination at any of the designated points, meaning that $\forall i, I_{p,i}(t) = 0$, SELAS activates hibernation mode. During this mode, SELAS remains at the charging point P_0 and continues to charge the prospecting rover using the remaining energy from BS_{2i} as long as $SOC_{BS2i}\,(t) \geq SOC_{min}$. After that, the battery stack at the prospecting rover will keep discharging with no assistance from SELAS. Both SELAS and the prospecting rovers operate in hibernation mode, supplying energy only to the essential systems required for survival.

While in hibernation mode, SELAS constantly checks the illumination conditions at every P_i. Once SELAS detects illumination at one of the designated points it immediately begins

traveling to that location, overriding the standard charging schedule. Upon arrival, SELAS remains at the illuminated point until it fully recharges its batteries. It then returns to P_0 to fully recharge the prospecting rover. After completing this task, the regular charging schedule resumes. The flowchart of the simulation process for SELAS is depicted in Figure 4-7.

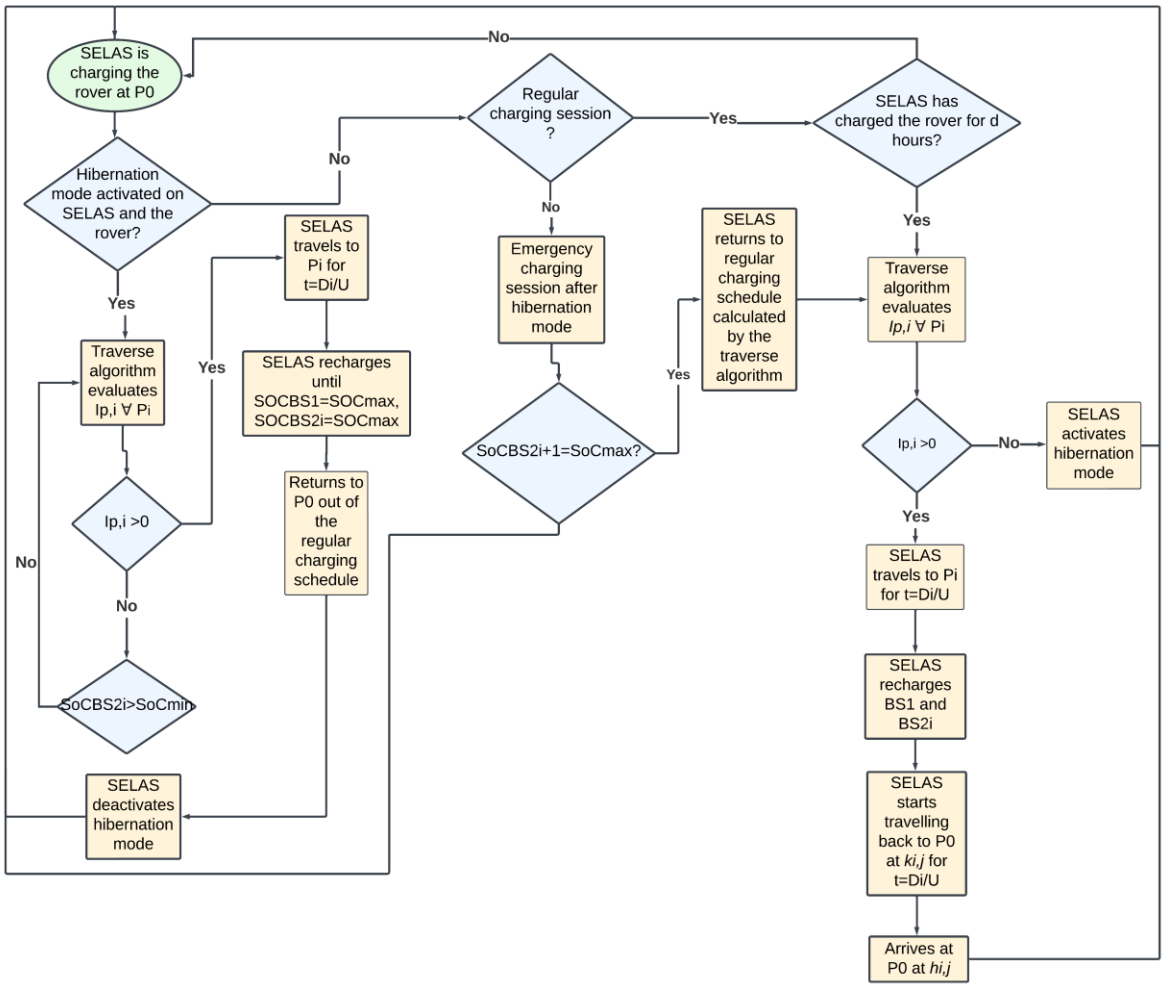

Figure 4-7. Flowchart of the simulation for SELAS.

5

Simulation of SELAS

To assess the operational capabilities of SELAS, a MATLAB simulation program was developed. A specific area of interest (P_0) selected from those discussed in paragraph 2.1.8, was used as the simulation setting. Based on literature, the nearest illuminated points P_i and the corresponding illuminated paths D_i leading to them were identified. Multiple scenarios were designed to evaluate SELAS's performance, each varying in rover instrumentation, mission schedules, scientific output, and consequently, power consumption. These scenarios are detailed in the subsequent chapters.

5.1 Selected Site of the Mission

Among the proposed locations discussed in paragraph 2.1.8, Henson Crater was selected due to several favorable attributes. Its proximity to well-illuminated points, relatively flat terrain—facilitating accessibility for simple and technologically mature robotic systems—scientific significance, and resource-rich environment make it an ideal site for a prospecting mission with clear objectives. The mission duration is set to one year, providing ample time for a single rover or a swarm to explore, conduct research, and prospect or excavate a substantial area.

The area of interest, is centered at (P_0, 88.65289, 137.51367), has a perimeter of 21.46 km and an area of 28.78 km2. As seen in the model exported from the Lunar QuickMap [112] in Figure 5-1 the area of interest has an easily traversable terrain. The maximum slope of the area is 5.697 °, which favors the movement of the rover and minimizes the power consumption due to trafficability reasons. Lunar QuickMap is a tool offering seamless access to numerical data layers for lunar terrain, featuring a range of global and regional terrain products, including

LOLA, SLDEM2015, and NAC DTMs, as well as data from the Clementine, Chandrayaan-1, and Kaguya missions.

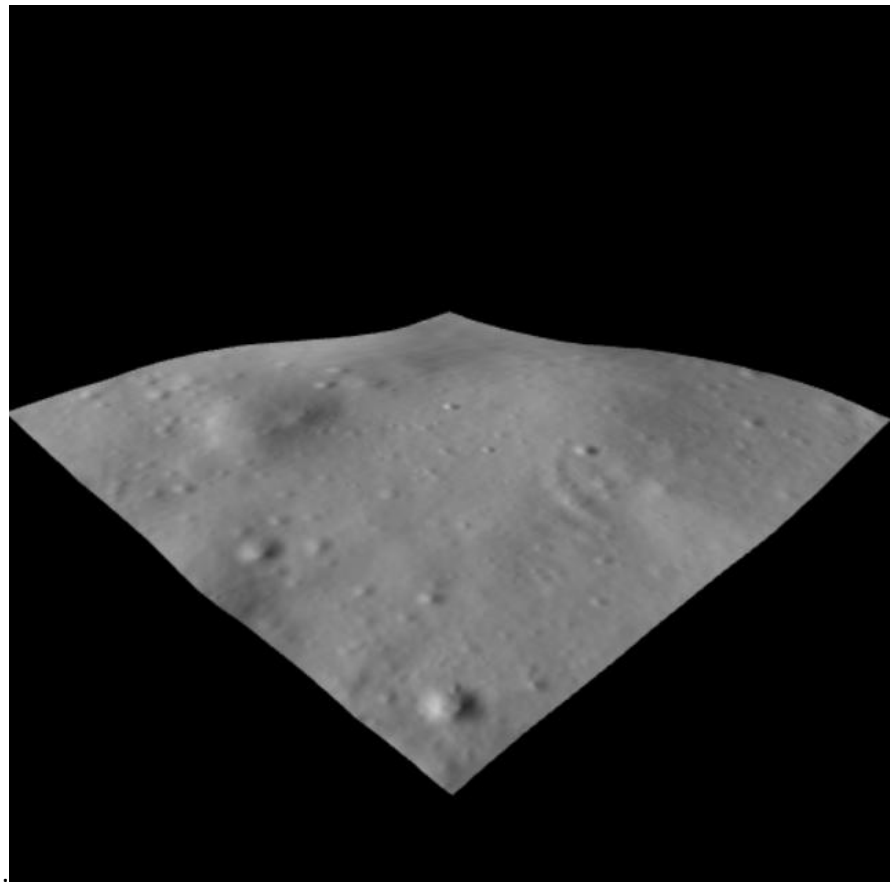

Figure 5-1. Terrain model of the area of interest, generated by Lunar QuickMap.

5.2 Illuminated Points

According to the literature, the most favorable illuminated points near the prospecting area were identified in [114]. This study utilized Kaguya topography data to perform a detailed yearly illumination analysis for 2020. The findings revealed four illuminated points around the area of interest (P_0) with not only optimal illumination conditions but also complementary characteristics. This is crucial for SELAS, which requires at least one illuminated point to function effectively.

Based on the outcomes of the analysis, multiple key areas were highlighted for their consistent illumination. These include a location on the rim of Shackleton crater (P_1, 89.68°S, 166.0°W), a peak near Shackleton crater (P_2, 89.44°S, 141.8°W), a point on the perimeter of De Gerlache crater (P_3, 88.71°S, 68.7°W), and a small elevated area extending along the 120°E longitude from the rim of Shackleton crater (P_4, 89.79°S, 124.5°E). The area of interest (P_0) is situated

7 km inside of Henson crater (88.76°S, 134.72°E) as illustrated in Figure 5-2. The study period spans from January 1, 2020, to January 1, 2021, encompassing a 1-year mission and of illumination data. The period from February 11, 2020, to August 3, 2020, corresponding to days 41 through 215 of the study period, is considered as the summer season, with negative sub-solar latitude. Conversely, the winter period lasts from August 4, 2020, to January 1, 2021, covering days 215 through 365 of the study period. January 1,2020 till the 11th of February 2020, is also considered a winter season.

The illumination time series for these points were derived from the referenced study, providing detailed illumination histories for 2020. Due to solar symmetry, it was sufficient to analyze six months of data, spanning from mid-summer to mid-winter, to determine the illumination profile for the entire year. The outcomes of the analysis are presented in Figures 5-3,5-4,5-5, which depict which days of the year each location is illuminated or in darkness. The polar plots represent sub-solar longitude as the angle and sub-solar latitude as the radius. Summer is depicted by data points near the center of the plot, representing the most negative sub-solar latitudes. Each sub-solar longitude includes six data points, representing half of a lunar year.

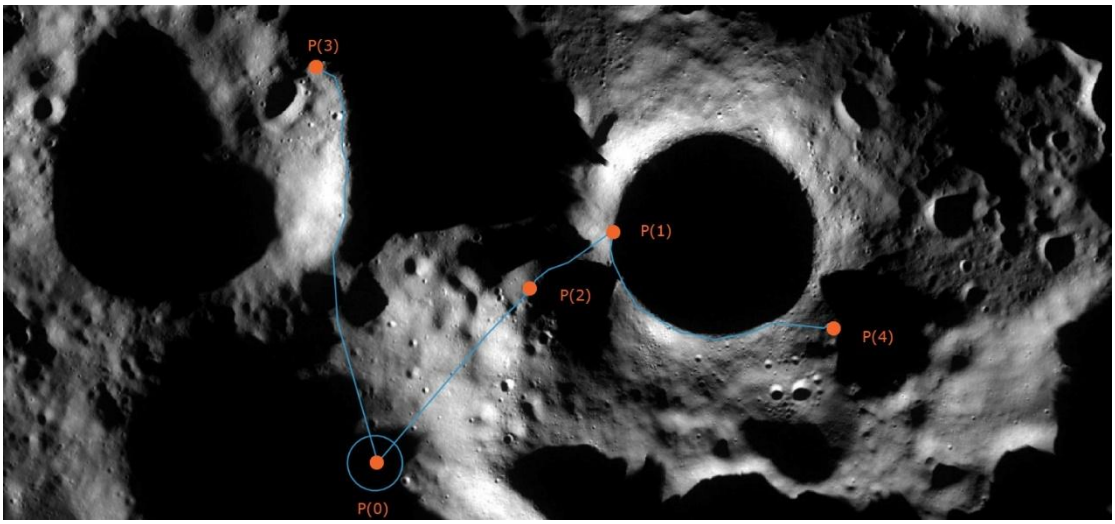

Figure 5-2. Point of interest P_0 in Henson Crater and illumination points P_1, P_2, P_3, P_4 (in orange) and the illuminated paths for each point (in blue), generated by Lunar QuickMap.

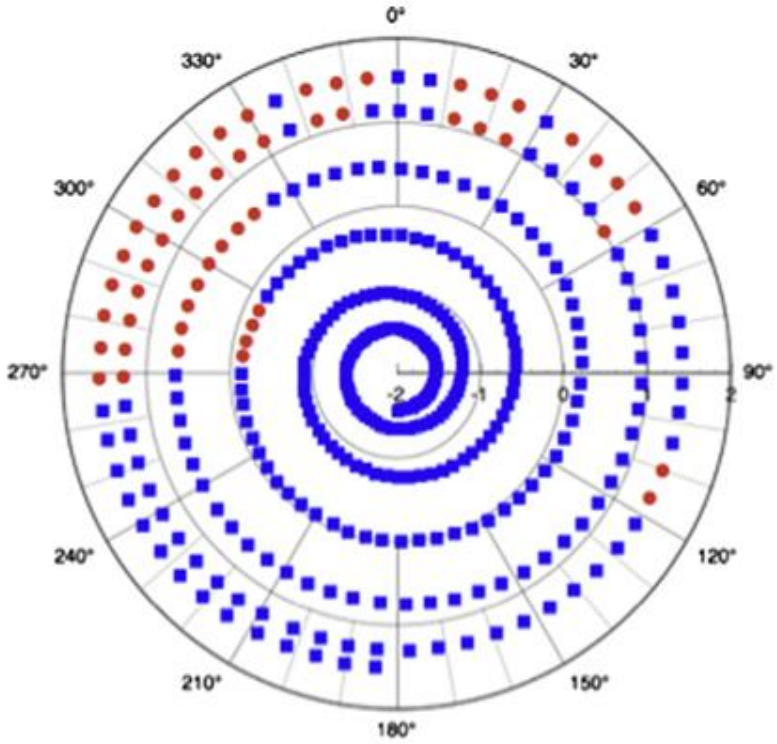

Figure 5-3. Illumination conditions for Point P_4 from mid-summer to mid-winter. Blue color dictates an illuminated day, red dictates a dark day. This point is lit for a period of more than 5 months on summer season [114].

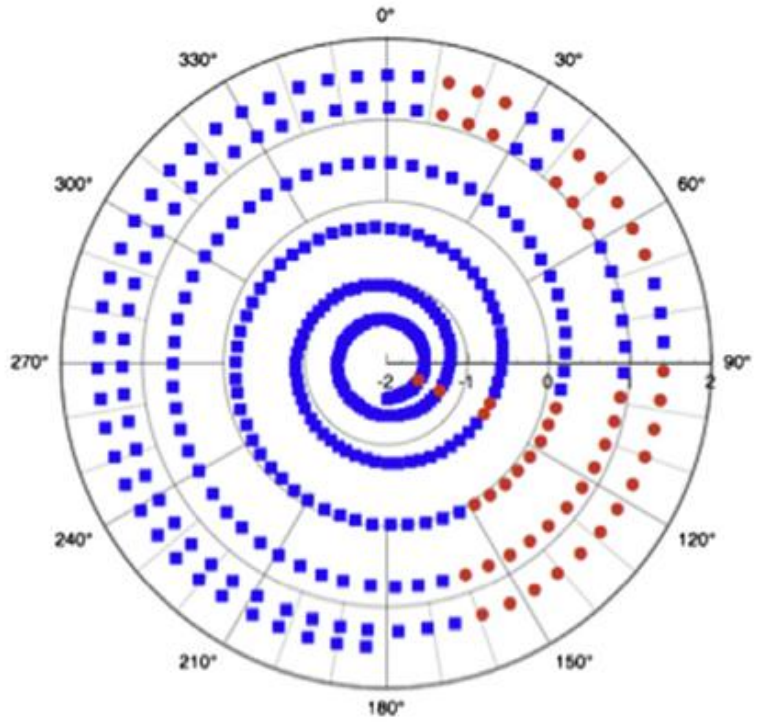

Figure 5-4. Illumination conditions for Point P_3 on the rim of De Gerlache crater from mid-summer to mid-winter. Blue color dictates an illuminated day, red dictates a dark day [114].

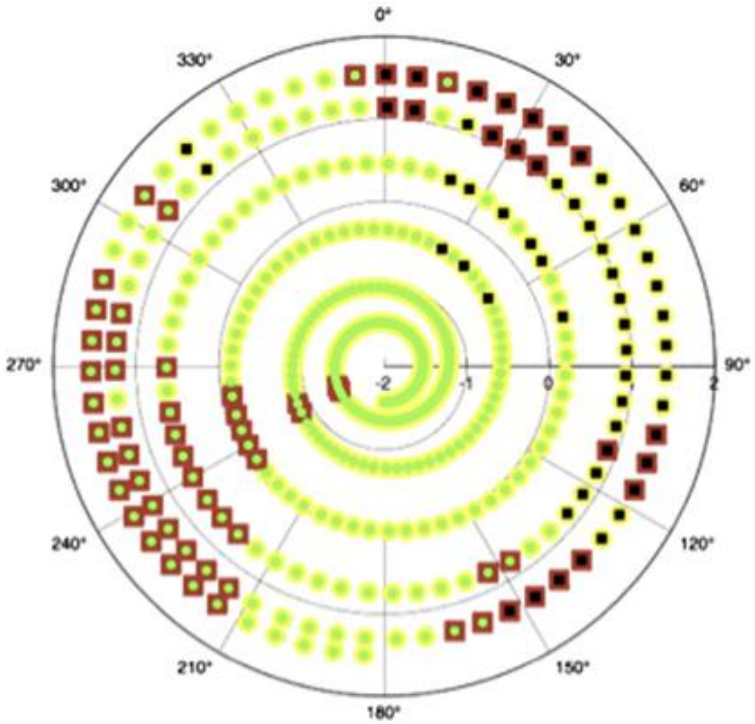

Figure 5-5. Illumination conditions for Points 1 and 2 from mid-summer to mid-winter (Point 1 is lit at yellow and dark at red. Point 2 is lit at green and dark at black). Point 2 is illuminated for more than 4.5 months in the summer while it remains dark for 4.5 days within an 8-month span. Overall Points P_1 and P_2 experience lighting for 94% of the time [114].

Point P_2 features a yearly average illumination of 82% and receives continuous sunlight for more than 4.5 months. In the course of the 8-month period around mid-summer, it experiences only brief eclipses lasting between 12 and 24 hours, with a total eclipse duration of 4.5 days within that timeframe [114]. Additionally, P_2 complements P_1, as one site is often illuminated when the other is in darkness. Together, P_1 and P_2 are illuminated for an uninterrupted 8-month period and more than 94% of the total 6 months period (Figure 5-5). Meanwhile, P_3 stands out for having the shortest maximum eclipse period among the analyzed sites, lasting just 6 days.

Using the data from [114] and Figure 5-3, 5-4 and 5-5 the daily illumination conditions of the points of interest were determined. Additionally, the NASA Lunar Trek platform (an online, browser-based tool that enables visualization, exploration, and analysis of the lunar surface using real spacecraft data) provided the azimuth and elevation angles for the specified dates [115]. These angles were used to calculate the exact solar irradiance (W/m²) received by a photovoltaic panel, following the equations outlined in paragraph 4.1.

5.3 Traverse Paths

E. Mazarico et al. [23] proposes four paths with favorable illumination conditions relevant to this study. The first path (Path 1, Figure 5-6) connects the Connecting Ridge plateau and the eastern rim of de Gerlache, linking P_0 and P_3. The suggested path in the referenced study measures approximately 56 km, whereas in this thesis, only about 46 km are utilized. Path 2 includes P_2, P_1, and extends to P_4, traversing the far section of Shackleton crater with a total length of approximately 47 km.

Henceforth, Path 1, which connects P_0 to P_3, will be referred to as D_{03} spanning for almost 46 km (Figure 5-7). Path 2 will be divided into three segments: D_{01}, D_{02}, and D_{04}. Notably, D_{01} includes D_{02}, while D_{04} encompasses D_{01}, D_{12}, and D_{24} (Figure 5-8). The numbering order is significant, as it indicates the direction of SELAS movement. For instance, D_{03} represents travel from P_0 to P_3, whereas D_{30} indicates the reverse direction.

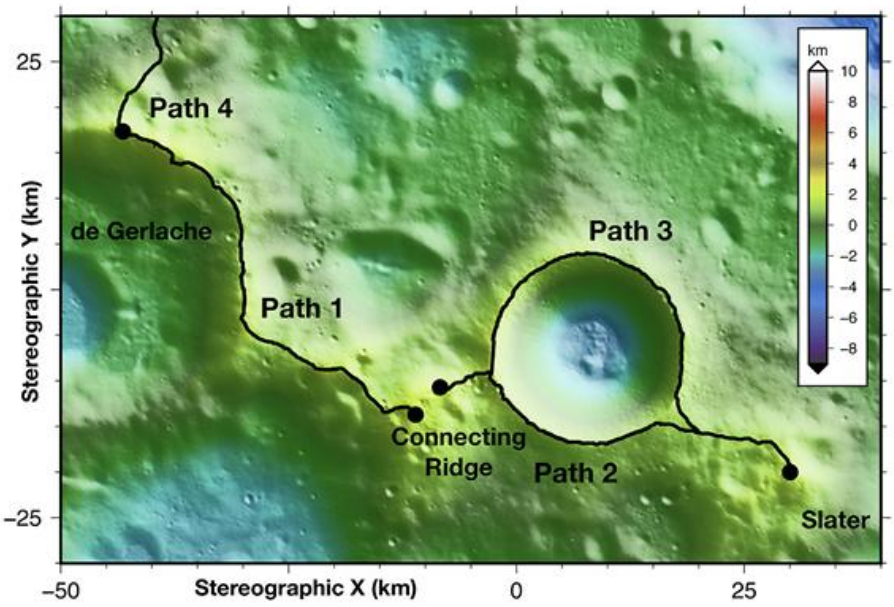

Figure 5-6. LOLA topographic maps of the south pole area presented in polar stereographic projection; the South Pole positioned at (0,0). The color coding represents elevation relative to the 1737.4-km reference sphere. The paths are displayed in black [23].

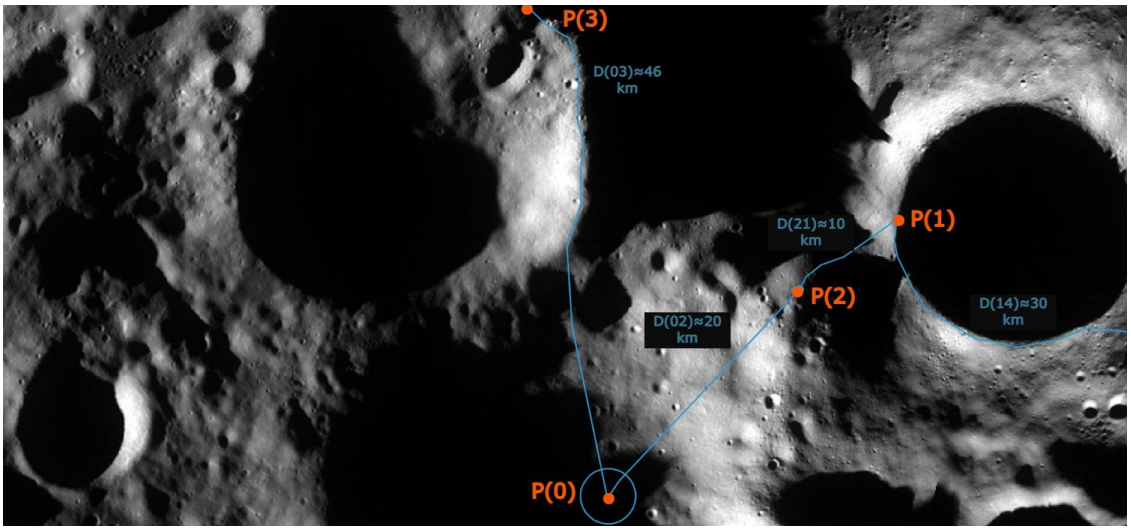

Figure 5-7. Area of interest centered at P_0 inside Henson Crater and illumination points P_1, P_2, P_3, P_4 (in orange) and the illuminated paths D03, D02, D21 & D14 (in blue). Image generated by Lunar QuickMap.

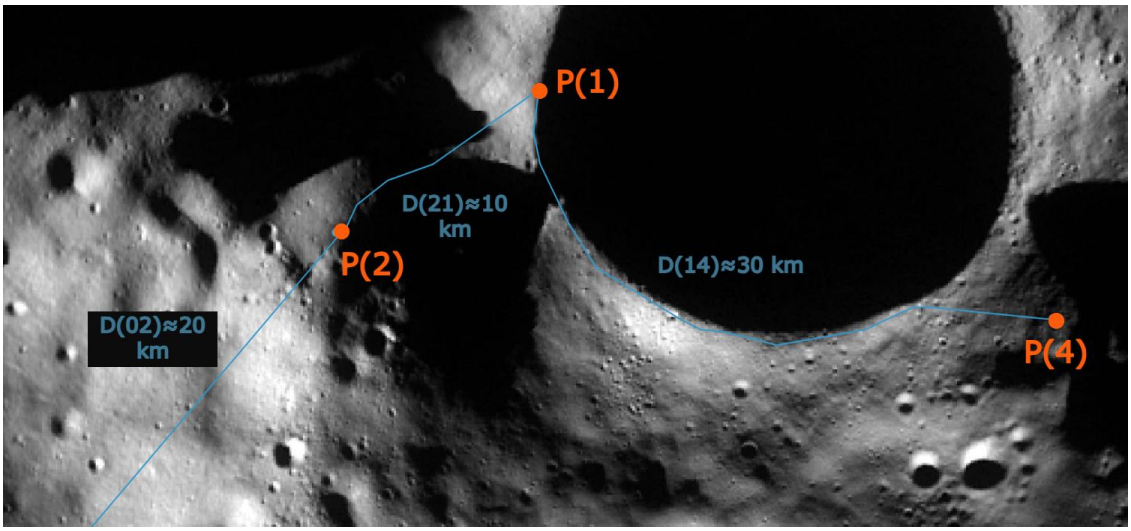

Figure 5-8. Area of interest centered at illumination points P_1, P_2, P_4 (in orange) and the illuminated paths D02, D21 & D14 (in blue). Image generated by Lunar QuickMap.

Considering the illumination conditions of the paths described in [23], traverses during the winter season present significant challenges, as only 60% of the time a path is illuminated, in contrast with the summer months that paths are sunlit for 90% of the given period. Since daily illumination data for such long traverses and specific points were unavailable, the simulation introduces a degree of randomness to account for the photovoltaic illumination during SELAS traversal, based on the aforementioned percentages.

Due to the complexity of simulating the illumination conditions for multiple points along the path for an entire year, a single time series of illumination values was generated to represent every moment t for each path.

The proposed paths were selected not only for their illumination conditions but also for their relatively favorable slopes, ensuring that a standard four-wheel rover like SELAS can traverse them safely at the required speed while minimizing energy consumption during travel. The ACT Lunar QuickMap was employed to extract detailed information about the paths, such as exact distances and terrain slopes (Figures 5-9,5-10,5-11,5-12).

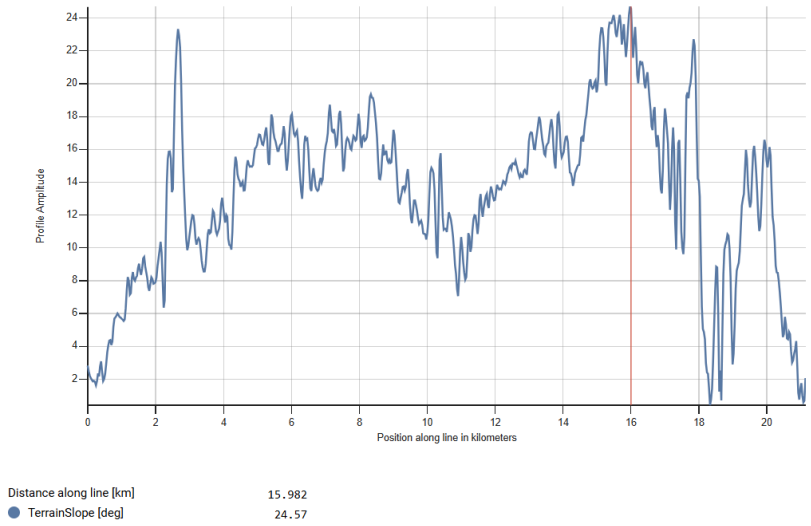

Figure 5-9. D_{02} path terrain slope, plot extracted by ACT QuickMap.

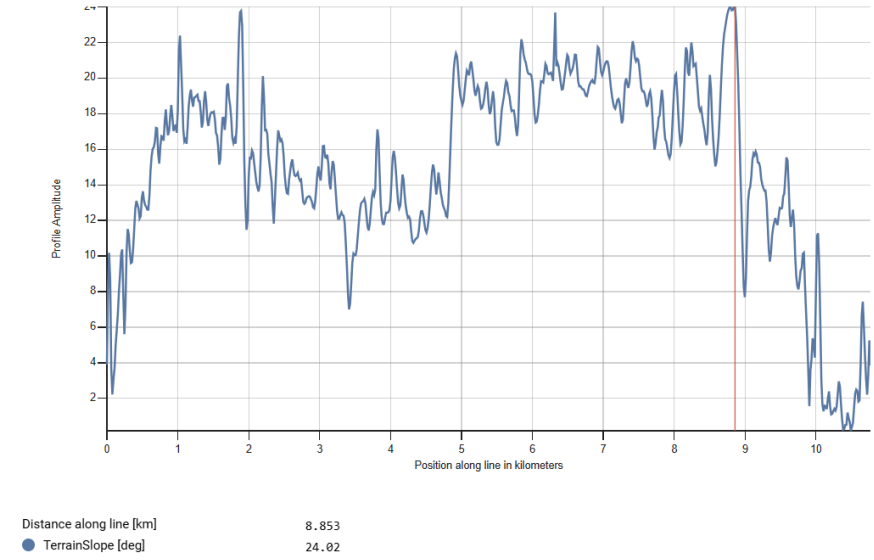

Figure 5-10. D_{12} path terrain slope, plot extracted by ACT QuickMap

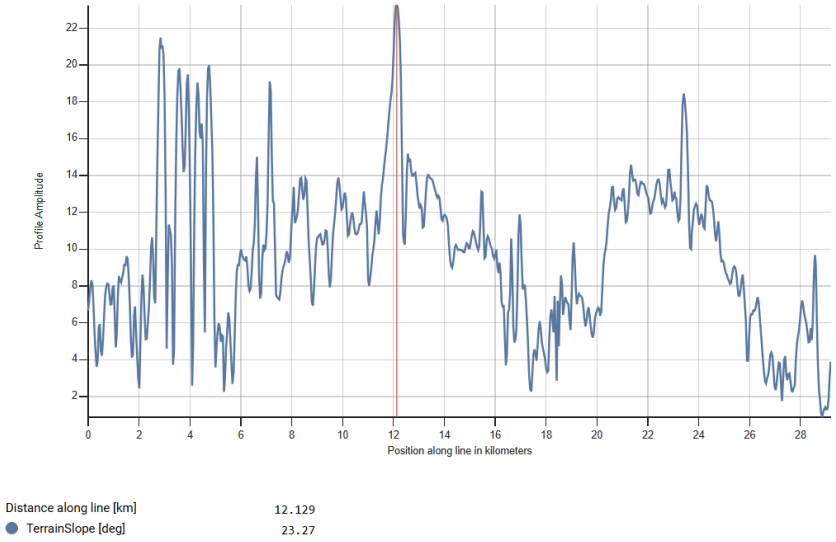

Figure 5-11. D_{14} path terrain slope, plot extracted by ACT QuickMap.

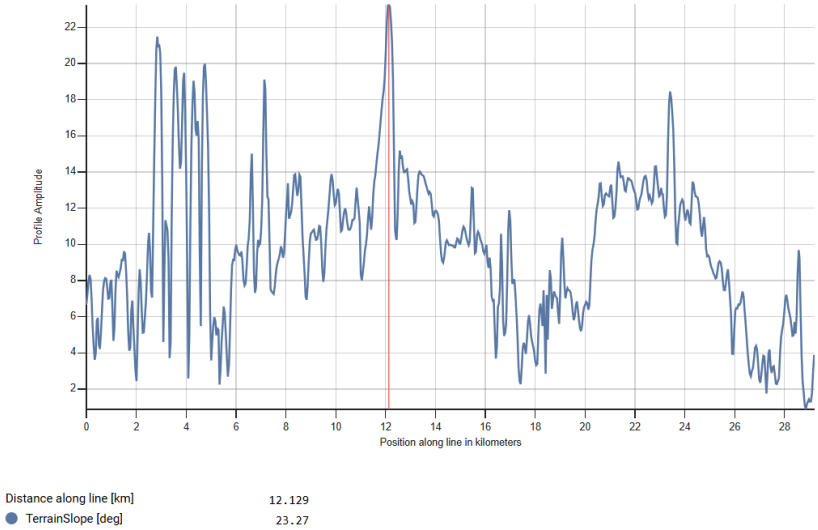

Figure 5-12. D_{03} path terrain slope, plot extracted by ACT QuickMap.

As illustrated in the figures above, the maximum terrain slope for all selected paths remains below the 25-degree threshold, as established by the literature reviewed in Chapter 2. The red vertical line in the plots indicates the point along the path with the highest terrain slope and the value of the slope.

In the run simulation, SELAS is assumed to have a speed of 10 km/h while the prospecting rover can move up to 0.72 km/h, similar to VIPER [116]. As discussed in paragraph 3.1.1 SELAS power consumption will differ amongst the various slopes, switching from nominal to peak traversing.

5.4 Simulated Scenarios

The eight selected scenarios are designed to demonstrate the versatility of SELAS in supporting a prospecting mission in the PSR of the Henson area, focusing on volatile exploration. The VIPER mission was chosen as a reference due to its similarity in purpose, the availability of data on instrumentation and power consumption, and its scientific significance. The rover in these scenarios is equipped with instruments identical to those used in VIPER (NSS, NIRVSS, and MSolo), with the addition of the TRIDENT drill in Scenarios 3, 4, 5, and 8. Furthermore, the capability of SELAS to charge more than one rover per charging session is analyzed in Scenarios 6, 7, and 8.

The power consumption of the rover's systems, aside from its instrumentation, is detailed in each scenario. The rover's basic power-consuming subsystems are similar to those of SELAS, including TMTC, OBDH, GNC, and mobility. However, the mobility system consumes less power due to the rover's lower speed and operation in a relatively flat terrain.

5.4.1 Outline of Scenario 1

In this case, it is assumed that the rover alternates between traversing for one hour (with instruments turned off) and stopping for one hour to conduct research, during which its instruments (NSS, NIRVSS, and MSolo) are activated. There is also the hibernation mode, in which rover's and SELAS systems consume the minimum possible power to survive the dark phases. According to this schedule and the rover's speed, assuming that SELAS charges the rover during the science phase, eliminating the need for additional charging time, the rover can traverse 8.64 km per day. This equates to approximately 3,150 km per year, allowing it to collect data from a total of 4,380 points. Table 5-1 provides a detailed breakdown of the power consumption for each instrument.

Table 5-1. Mass, volume and power consumption of instruments on rover in Scenario 1.

Instrument	Power, (W)
MSolo	35
NIRVSS	Spectrometer: 12 Bracket Assembly: 5.3 Lamp: 12.3
NSS	1.5
Total	66.1

The following tables provide a detailed breakdown of the rover's power consumption, depending on whether it is traversing, engaged in research activities, or in hibernation.
During the rover's mobility phase, the majority of power is consumed by the OBDH and heating systems, while the power required for mobility remains minimal due to the low slopes of the terrain and the rover's relatively low speed. During the science phase, as anticipated, the instruments account for the majority of the power consumption. Finally, in hibernation mode, only essential systems remain active, including heating and a few minor functions required to maintain operational readiness. The power consumption through the hibernation phase is the same for all the following Scenarios.

Table 5-2. Rover's projected electric power budget breakdown on science and charging phase in Scenario 1.

System	Power (W)
Mobility	0
TCS	15
TMTC	9
OBDH	20
GNC	6
Instruments	66.1
Total	118.1

Table 5-3. Rover's projected electric power budget breakdown on mobility phase in Scenario 1.

System	Power (W)
Mobility	4
TCS	15
TMTC	9
OBDH	25
GNC	6
Instruments	0
Total	59

Table 5-4. Rover's projected electric power budget breakdown on hibernation phase in Scenario 1.

System	Power (W)
Mobility	0
TCS	15
TMTC	0
OBDH	2
GNC	0
Instruments	0
Total	17 W

5.4.2 Outline of Scenario 2

In the second scenario, unlike the first, the rover operates continuously, with its instruments remaining active at all times. The rover only halts for recharging by SELAS, during which the instruments continue to function without interruption. So, in this case, the mobility phase is also science phase. According to this schedule and the rover's speed, as well as the charging frequency of 3–4 times per day determined by the optimization algorithm (details provided later), the rover operates for approximately 21 hours daily, covering 15.12 km per day. This results in a total of 5,518 km fully mapped by a single rover in a year.

Table 5-5. Rover's projected electric power budget breakdown on science/mobility phase in Scenario 2.

System	Power (W)
Mobility	4
TCS	15
TMTC	9
OBDH	25
GNC	6
Instruments	66.1
Total	119.1

Table 5-6. **Rover's projected electric power budget breakdown on charging/science phase in Scenario 2.**

System	Power (W)
Mobility	0
TCS	15
TMTC	9
OBDH	25
GNC	6
Instruments	66.1
Total	115.1

5.4.3 Outline of Scenario 3

In this scenario, the rover's activities closely resemble those in the first scenario, with the key difference being that the rover is additionally equipped with TRIDENT. When the rover halts every hour, it also performs drilling operations and analyzes underground samples. The analysis of the power consumption of the instruments that the rover is equipped with is shown. in Table 5-7 while the total power analysis of all the systems during the science phase of the rover is in Table 5-8. The power consumption during mobility and hibernation phases is the same as in Scenario 1.

Table 5-7. Mass, volume and power consumption of instruments on rover in Scenario 3.

Instrument	Power (W)
MSolo	35
NIRVSS	Spectrometer: 12 Bracket Assembly: 5.3 Lamp: 12.3
NSS	1.5
TRIDENT	Auger: 87
Total	66.1

Table 5-8. Rover's projected electric power budget breakdown on science phase in Scenario 3.

System	Power (W)
Mobility	0
TCS	15
TMTC	9
OBDH	20
GNC	6
Instruments	153.1
Total	203.1

5.4.4 Outline of Scenario 4

This scenario is identical to Scenario 3, with the addition of a 40 W heater integrated into the drill to measure downhole temperature and determine thermal conductivity. All other parameters remain consistent with those outlined in Scenario 3.

Table 5-9. Rover's projected electric power budget breakdown on science phase in Scenario 4.

System	Power (W)
Mobility	0
TCS	15
TMTC	9
OBDH	20
GNC	6
Instruments	193.1
Total	248.1

5.4.5 Outline of Scenario 5

In this scenario, the rover alternates between one hour of traversing, with the NSS, NIRVSS, and MSolo instruments activated to map the route, and one hour of drilling while all

instruments are operational, without the addition of the extra heater. Based on this schedule and the rover's speed, and assuming SELAS recharges the rover during the drilling phase, thereby removing the need for additional charging stops, the rover can traverse and map 8.64 km daily. Over the course of a year, this results in approximately 3,150 km traveled and data collected from drilling at 4,380 points.

Table 5-10. Rover's projected electric power budget breakdown on science/traverse phase in Scenario 5.

System	Power (W)
Mobility	4
TCS	15
TMTC	9
OBDH	25
GNC	6
Instruments	66.1
Total	119.1

Table 5-11. Rover's projected electric power budget breakdown on science/drilling phase in Scenario 5.

System	Power (W)
Mobility	0
TCS	15
TMTC	9
OBDH	20
GNC	6
Instruments	153.1
Total	203.1

5.4.6 Outline of Scenario 6

In this scenario, SELAS has the capability to charge two rovers simultaneously. It is assumed that the power consumption, instrumentation, and scheduling for each rover and SELAS are identical to those outlined in Scenario 1. To facilitate simultaneous charging, the rovers may

need to make slight adjustments to their planned paths during their missions to align with SELAS for recharging.

5.4.7 Outline of Scenario 7

In this scenario, SELAS is designed to charge two rovers as well. However, it is presumed that the power consumption, instrumentation, and scheduling for each rover and SELAS are the same as those outlined in Scenario 2. This implies that each rover operates with its instruments continuously active during traverses, pausing only to recharge with SELAS. The total traverse travelled is 15.12 km per day per rover. This results in a total of 11,036 km fully mapped by both rovers per year.

5.4.8 Outline of Scenario 8

In the last scenario examined in this thesis, SELAS charges two rovers with the power consumption, instrumentation, and scheduling similar to Scenario 5. Each rover alternates between one hour of traversing, with the NSS, NIRVSS, and MSolo instruments activated to map the route, and one hour of drilling, without the addition of the extra heater, while all instruments are operational. Based on this schedule and each rover's speed, each rover can traverse and map 8.64 km daily. In the span of a year, this results in approximately 6,300 km traveled and data collected from drilling at 8760 points.

6

Optimization of the System

In space missions, the primary cost-driving factor for a launch is the total payload mass, as discussed in paragraph 2.3. Consequently, the optimization process focuses on minimizing the system's total mass, thereby reducing the required propellant and overall mission cost.

The optimal sizing of the system can be determined through multiple approaches, including the balanced generation and load demand method, genetic algorithms (GA), linear programming, particle swarm optimization (PSO), and others. Although, as analyzed in 2.4.4, PSO demonstrates a reduced dependency on the initial set of points relative to other methods, indicating its robustness in algorithmic convergence. Therefore, the proposed optimal system sizing is achieved and implemented using the PSO method.

6.1 Calculation of the Total System Weight

As detailed in paragraph 4.3, SELAS is capable of charging multiple rovers. It should be noted that the optimization process utilized in this thesis is consistent across all configurations and can effectively size the system based on the number r of rovers.

The primary decision variables for the proposed design include the total number of batteries on SELAS for BS_1, $N_{bat,BS1}$, the total number of batteries in each of the r BS_{2i}, $N_{bat,Prosp}$, and the total number of batteries $N_{bat,Rover}$ on each of the BS_{2i+1}. Also, the number of the photovoltaic panels in series $N_{s,PVsBS1}$ and in parallel $N_{p,PVsBS1}$ of the array designated for the

charging of BS_1 and the number of photovoltaic panels in series $N_{s,PVsProsp}$ and in parallel $N_{p,PVsProsp}$ of the r arrays designated for the charging each one of the BS_{2i}. Lastly, the frequencies f_i for every P_i are also an output of the optimization process. These parameters have been thoroughly detailed in Chapter 4 and collectively form the vector of decision variables as follows:

$$X=[\ N_{s,PVsBS1}|N_{p,PVsBS1}\ |$$
$$|\ N_{s,PVsProsp}\ |\ N_{p,PVsProsp}\ |N_{bat,BS1}\ N_{bat,Prosp}|\ N_{bat,Rover}\ |\ f_1|\ f_2|\ \dots|\ f_n\ ] \quad (6.1)$$

The aim of the optimization process is to minimize the value of X and therefore minimize the total system weight $W_{total}\ (kg)$:

$$\min_X\{\ W_{total}(X)\ \}$$

The constraints for the variables are the following:

$$0 \le N_{s,PVsBS1,}N_{s,PVsProsp} \le floor\ \left(\frac{V_{MPP,max}}{\max[V_{MPP}(t)]}\right) \quad (6.2)$$

where $1 \le t \le 8760$

and $N_{p,PVs} > 0$, $N_{bat,SELAS} > 0$, $N_{bat,Prosp} > 0$, $N_{bat,Rover} > 0$, $0 < f_i \le f_{i,max}$.

$V_{MPP,max}\ (V)$ is the maximum voltage level at the maximum power point of the battery charger.

The total weight of the system, including the entire power system of SELAS, the batteries on the rovers and the necessary chargers, is:

$$W_{total}(X) = w_{pv} \cdot N_{p,PVsBS1}\ \cdot N_{s,PVsBS1}\ + N_{bat,BS1}\ \cdot w_{bat} + w_{chBS1} + r \cdot (N_{p,PVs}\ \cdot N_{s,PVs}\ ) \cdot w_{pv} + r \cdot (N_{bat,Prosp}) \cdot w_{bat} + r \cdot w_{chProsp} + r \cdot N_{bat,Rover} \cdot w_{bat} \quad (6.3)$$

- $w_{pv}\ (kg)$ is the weight of each photovoltaic panel as calculated in paragraph 4.2.
- $w_{bat}\ (kg)$ is the weight of each battery as provided by the product's datasheet.
- $w_{chBS1}\ (kg)$ is the weight of the charger for the BS_1 and
- $w_{chProsp}\ (kg)$ is the weight of each charger for each BS_2.

6.2 Optimization Process

During the simulation, the PSO algorithm generates multiple candidate solutions represented by the vector **X**. For each candidate, the simulation runs over an entire operational year (8,760 hours), as detailed in Chapter 4. Additionally, the total weight, $W_{total}(X)$, is computed based on equation (6.3). The vector $\boldsymbol{X}$ is considered the optimal solution if it satisfies two conditions: (1) the SoC of all battery stacks (BS_1, BS_2, and BS_3) remains above the minimum threshold specified in paragraph 4.3.1 throughout the simulation, and (2) it minimizes $W_{total}(X)$. The swarm consists of 30 particles, and the algorithm is configured to run for 220 iterations.

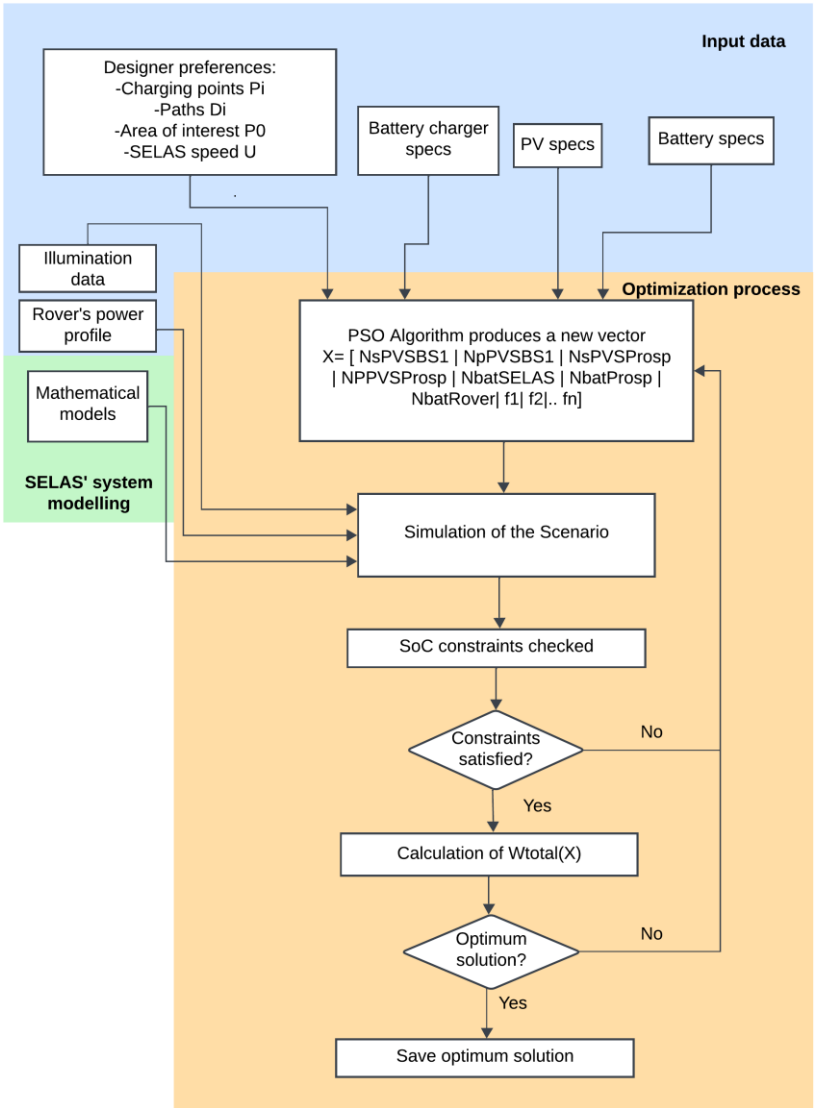

Figure 6-1. Flowchart of the optimization process.

7

Optimization Results

The optimization process aims to determine the optimum sizing of the SELAS system and rover's batteries, as well as the optimum charging schedule, while the simulation is designed to validate the system's performance under these optimal conditions.

For each scenario detailed in Chapter 5, this chapter presents the optimized sizes of the photovoltaic panels, battery stacks, and chargers, as well as the total system weight and daily charging schedule, as determined by the optimization process. The ratio of the total power system mass to the mean power consumption of the rovers has been calculated as a reference to compare the outcomes of the scenarios and evaluate SELAS's suitability for each case. Additionally, the required launch vehicle mass for each scenario is estimated based on the analysis of paragraph 2.3 along with an evaluation of its associated economic cost. Finally, a comprehensive analysis of the state of charge for all battery stacks is provided, covering both annual performance and hibernation mode, to highlight SELAS' operational effectiveness.

7.1 Scenario 1 Results

During the first scenario, the rover's power consumption is relatively mild, with the only power consuming instruments to be the Neutron Spectrometer and the Near Infrared Spectrometer. The results of the optimization algorithm are presented in Table 7-1 while the sizes of all the devices as a result of the PSO algorithm and their mass are presented in Table 7-2. The battery chargers used in all scenarios are commercially available off-the-shelf products from Crane Aerospace & Electronics.

Table 7-1. Results of the optimization algorithm for Scenario 1.

Parameter	Optimal value
$N_{s,PVsBS1}$	3
$N_{p,PVsBS1}$	8
$N_{s,PVsProsp}$	3
$N_{p,PVsProsp}$	6
$N_{bat,BS1}$	85
$N_{bat,Prosp}$	13
$N_{bat,Rover}$	24
f_1	3
f_2	3
f_3	3
f_4	1

Table 7-2. Optimized values of all the devices and their respective mass for Scenario 1.

Device	Optimized value	Weight (kg)
Battery Stack 1	85	107.95
Battery Stack 2	13	16.51
Photovoltaic Array 1	24 (N_s= 3, N_p=8)	27.84
Photovoltaic Array 2	18 (N_s= 3, N_p=6)	20.88
Battery Stack 3	24	30.48

For this scenario, the maximum energy requested $E_{req}(t)$ from BS_2 during a single-hour charging session as defined in paragraph 4.3, is set to 1800 Wh. Consequently, the maximum discharge current of BS_2 is 37.5 A. In Figure 7-1 the power architecture of the system is presented.

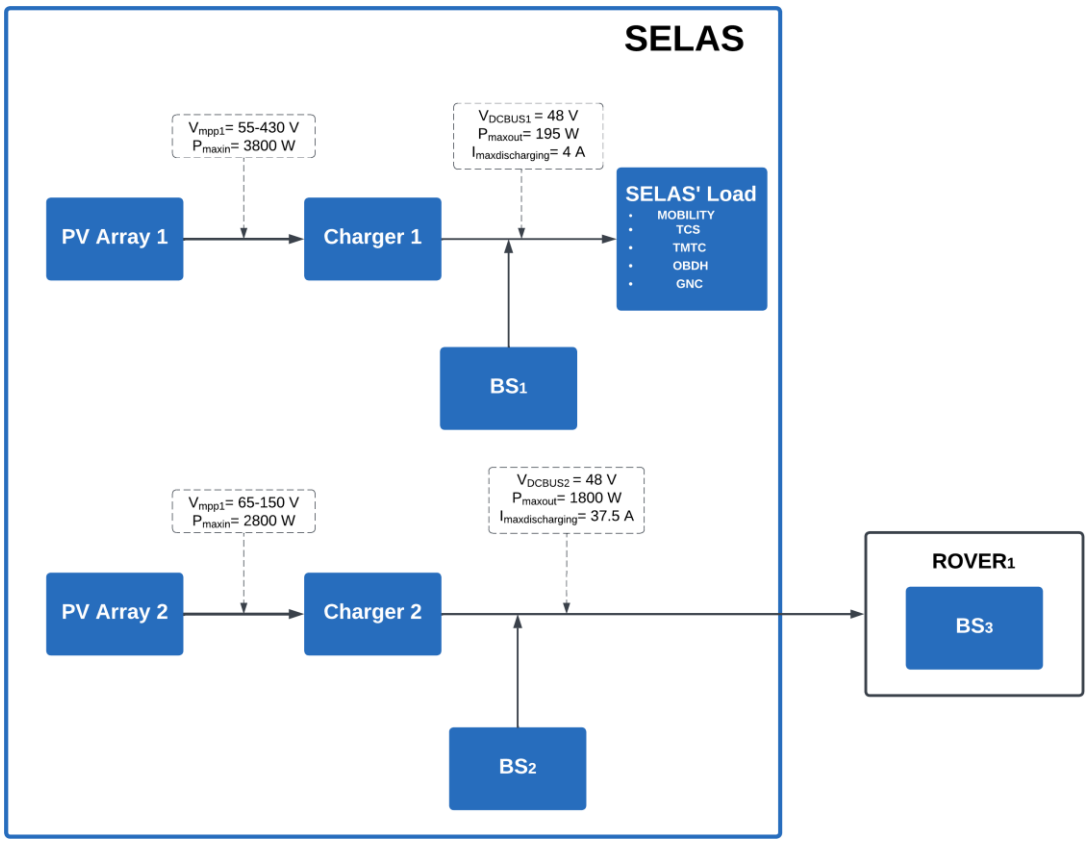

Figure 7-1. Power architecture of the system for Scenario 1. .

The total area needed for the photovoltaic arrays is 6.99 m^2 for PV array 1 and 5.24 m^2 for PV array 2. The power generated from the two photovoltaic arrays through the year, is presented in Figures 7-2 and 7-3.

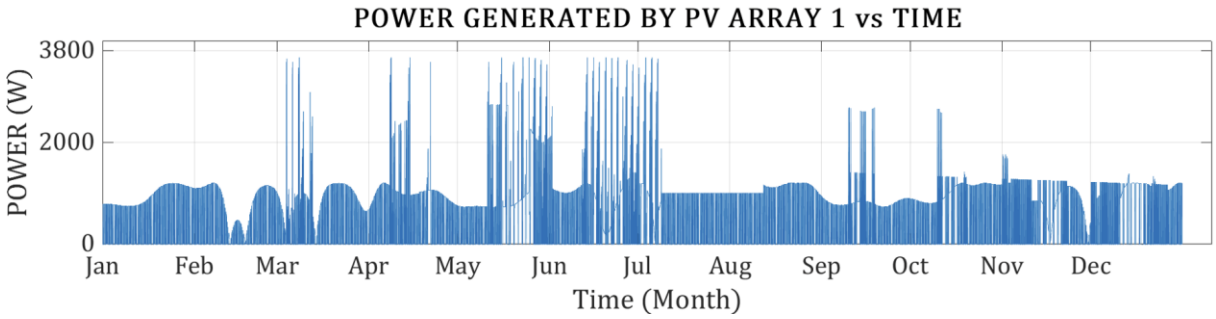

Figure 7-2. Power generated by PV Array 1 through a year in Scenario 1.

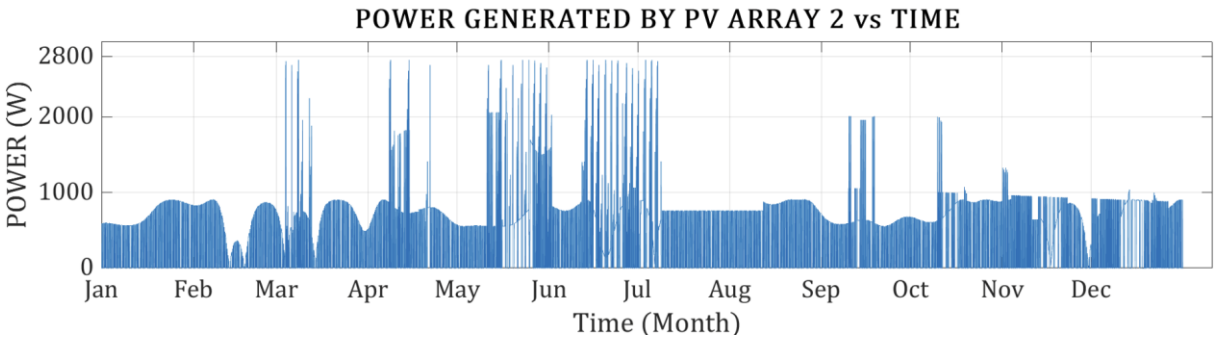

Figure 7-3. Power generated by PV Array 2 through a year for Scenario 1.

Based on commercially available chargers, the total weight of the chargers on SELAS is estimated to be 6.4 kg, contributing to a total system weight of 203.67 kg. According to the analysis in paragraph 2.3, achieving a lunar landing requires a launch vehicle with a minimum mass approximately 200 times the payload mass. For this power system only, the launch vehicle mass would amount to 40,734 kg. Additionally, with transportation costs of $80,000 per kilogram for delivering a payload from Earth to the lunar surface, the total cost for this mission would be approximately $ 16,293,600.

As for the mass of power system-to-average power consumed by the rover, based on the power analysis of paragraph 5.3, the average power consumed by the rover is 88.55 W, resulting in a ratio of 2.38 kg/W. The detailed values are presented in Table 7-3.

Table 7-3. Total masses of the payload, the launch vehicle and total cost of the mission for Scenario 1.

Characteristics of Scenario 1	Value
Payload Mass	203.67(kg)
Launch Vehicle Mass	40,734 (kg)
Total Cost	$ 16,293,600
Mass/P_{AVG}	2.38 kg/W

Additionally, the frequency of the charging was an outcome of the optimization algorithm, resulting to a specific charging schedule, depending on the charging point P_i. In this case, there are 4 different charging points and the outcome frequencies for the first three ones, f_1, f_2, f_3 are equal to 3 while for the fourth one, $f_4 = 1$, resulting in the schedules shown in Tables 7-4, 7-5, 7-6 and 7-7. The schedules are calculated with the equations of paragraph 4.4.

Table 7-4. Charging schedule of Scenario 1 for P_1.

J	$h_{1,j}$	$k_{1,j}$
1	1.00	22.00
2	09.00	06.00
3	17.00	14.00

Table 7-5 . Charging schedule of Scenario 1 for P_2.

j	$h_{2,j}$	$k_{2,j}$
1	1.00	23.00
2	07.00	05.00
3	13.00	11.00

Table 7-6 . Charging schedule of Scenario 1 for P_3.

j	$h_{1,j}$	$k_{1,j}$
1	1.00	21.00
2	11.00	07.00
3	21.00	17.00

Table 7-7. Charging schedule of Scenario 1 for P_4.

j	$h_{1,j}$	$k_{1,j}$
1	00.00	18.00
2	11.00	05.00
3	21.00	15.00

Although P_4 has a resulting frequency of f_4=1, its significant distance from P_0 (approximately 60 km) necessitated an adjustment in the charging schedule. The algorithm detailed in paragraph 4.4 generated three potential charging times based on the schedules of the other three charging points. From these options, the algorithm selects the charging hour closest to the current hour, ensuring efficient scheduling.

As outlined in Chapter 6, a candidate solution $\boldsymbol{X}$ is accepted only if the SoC of all battery stacks remains above the 20% minimum threshold. Figure 7-4 illustrates the SoC of BS_1, the battery stack dedicated to meeting SELAS' operational power needs. For most of the year, BS_1 maintains a charge level of approximately 80%, except during specific periods when SELAS must travel long distances to recharge at P_3 or P_4, as in the middle of June, or when illumination at the charging points is low, particularly during the winter months or completely dark (ex. December). During these intervals, the SoC approaches the 20% threshold, reaching a minimum value of 20.45 % in December.

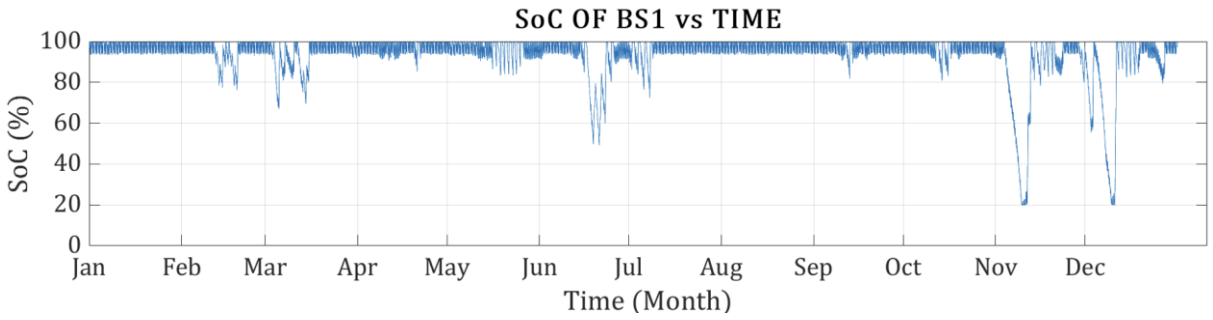

Figure 7-4. SoC of BS_1 through a year for Scenario 1.

Figure 7-5 presents the SoC of the second battery stack (BS_2), which is responsible for charging the rover (BS_3). Throughout the year, this battery stack cycles between full charge and the minimum threshold of 20%, as anticipated, given its critical role in maintaining the rover's functionality. While reaching the 20% minimum threshold poses no immediate operational issues as long as the battery is recharged and capable of supplying power to BS3, this repeated deep-cycling may have potential implications for the battery's lifetime.

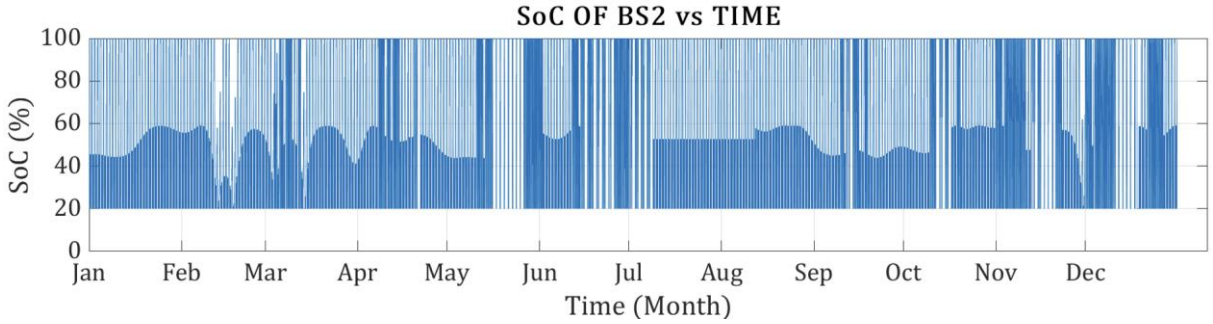

Figure 7-5. SoC of BS_2 through a year for Scenario 1.

Lastly, Figure 7-6 illustrates the SoC of the rover's internal battery stack (BS_3). As outlined in the mission objectives in Chapter 5, maintaining uninterrupted scientific activities within the PSR is critical. SELAS successfully ensures the rover's functionality, as the SoC of BS_3 remains within desirable levels throughout the mission. A notable similarity can be observed between Figures 7-2 and 7-4, where SoC drops occur during the same timeframes. These drops are attributed to the distance of the illuminated points or the seasonal decline in illumination levels.

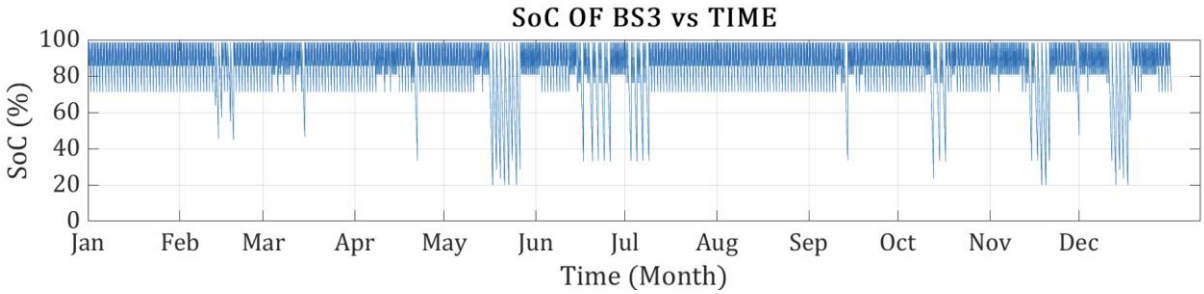

Figure 7-6. SoC of BS_3 through a year for Scenario 1.

As outlined in paragraph 4.4, if none of the available charging points P_i are illuminated, SELAS and the rover enter hibernation mode. Figures 7-5, 7-6 and 7-7 demonstrate the algorithm's functionality during hibernation mode. In the example provided, there is a 19-hour period (starting at 18:00 and ending at 14:00 of the next day) during which all available points are completely dark. Before this period, SELAS utilizes P_4 to recharge its batteries. SELAS stays at P_0 through this period and continues charging BS_3 as long as $SOC_{BS2} \geq 20\ \%$. Once SELAS detects illumination at any of the designated points, it promptly travels to that location, overriding the regular charging schedule.

1. At 12:00, SELAS arrives at P_4 as per its regular schedule. The SoC of BS_1 and BS_2 is increasing. While at P_4, SELAS operated in charging mode, which is characterized by a lower power consumption. Additionally, SELAS continued to charge its battery stacks while traversing the D_{04} path.
2. At 18:00, SELAS begins traveling back to P_0 through D_{40}. The SoC of BS_1 decreases as SELAS transitions to traversing mode, which involves higher power consumption. Additionally, the period of total darkness at the illuminated points begins at 18:00 but there is still light in the D_{40} path (Figure 7-10).
3. At 00:00, SELAS reaches P_0 following its regular charging schedule as outlined in Table 7-7. During this time, BS_2 discharges to recharge BS_3. As shown in Figure 7-6, the rover enters hibernation mode, resulting in reduced power consumption from 00:00 until 14:00 the following day (as indicated from the slope of the SoC curves during this period).
4. At 14:00 the next day, SELAS detects illumination conditions at P_2 and begins traveling toward it. The rover is no longer in hibernation mode.
5. At 16:00, SELAS reaches P_2 and recharges BS_1 and BS_2. At 17:00 it starts travelling back to P_0.

6. At 19:00, after two hours of travelling at the D_{02} path, SELAS reaches P_0, deviating from the regular charging schedule.
7. At 20:00, SELAS begins travelling back to P_2 to recharge BS_1 and BS_2.
8. Finally, at 01:00 SELAS goes back to P_0, it recharges BS_3 and resumes its regular charging schedule.

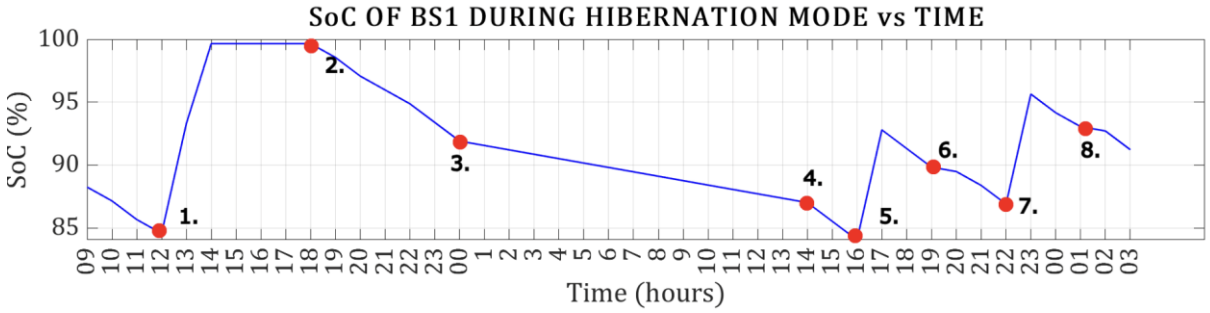

Figure 7-7. SoC of BS_1 during hibernation mode for Scenario 1.

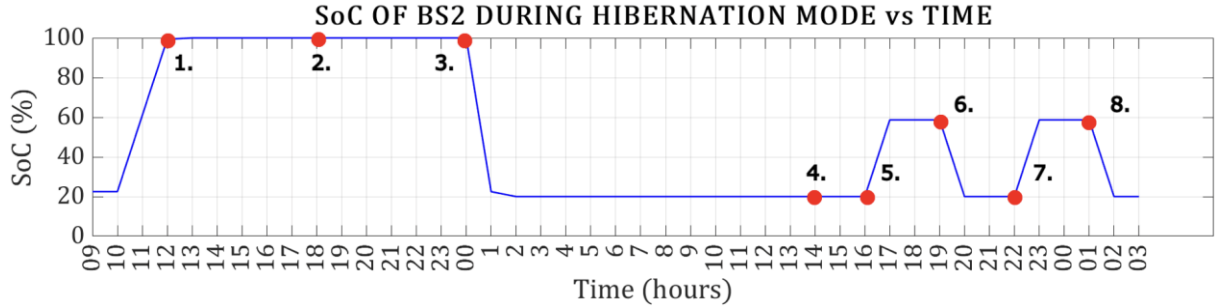

Figure 7-8. SoC of BS_2 during hibernation mode for Scenario 1.

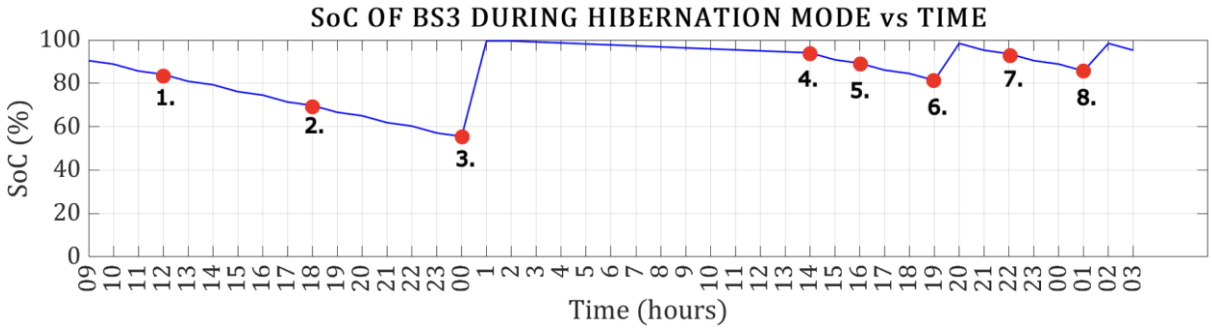

Figure 7-9. SoC of BS_3 during hibernation mode for Scenario 1.

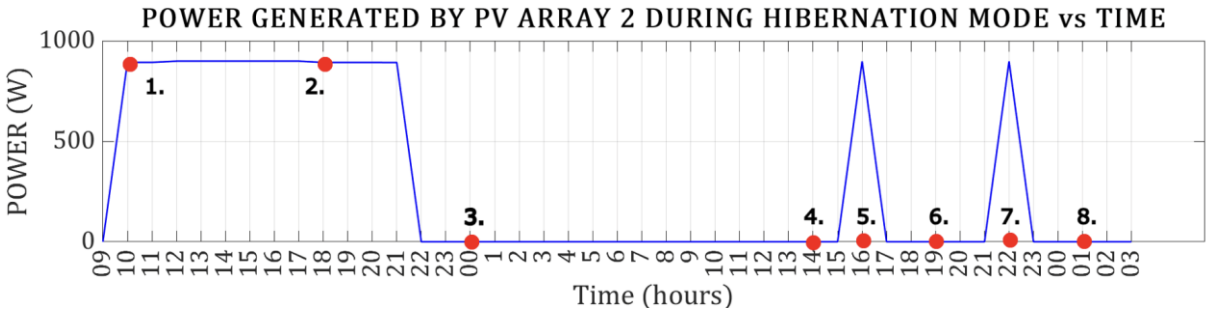

Figure 7-10. Power generated by PV Array 2 during a year for Scenario 1.

The output power of PV Array 1 mirrors the pattern observed in PV Array 2, as shown in Figure 7-10. Similarly, the hibernation mode operates under the same principles across subsequent scenarios, with minor variations reflected in the SoC figures and the power generated by the photovoltaic arrays.

7.2 Scenario 2 Results

In the second scenario, the rover's power consumption increases significantly due to its instruments operating continuously, enabling comprehensive data collection over 15.12 km per day and 5,518 km per year from a single rover. The sizes of all system components, as determined by the optimization algorithm, are detailed in Table 7-8.

Table 7-8. Results of the optimization algorithm for Scenario 2.

Parameter	Optimal value
$N_{s,PVsBS1}$	3
$N_{p,PVsBS1}$	8
$N_{s,PVsProsp}$	3
$N_{p,PVsProsp}$	8
$N_{bat,BS1}$	85
$N_{bat,Prosp}$	20
$N_{bat,Rover}$	35
f_1	3
f_2	3
f_3	3
f_4	1

Table 7-9. Optimized values of all the devices and their mass for Scenario 2.

Device	Optimized value	Weight (kg)
Battery Stack 1	85	107.95
Battery Stack 2	20	25.40
Photovoltaic Array 1	24 (N_s= 3, N_p=8)	27.84
Photovoltaic Array 2	24 (N_s= 3, N_p=8)	27.84
Battery Stack 3	35	44.45

For this scenario, the maximum energy requested $E_{req}(t)$ from BS_2 during a single-hour charging session is set to 2800 Wh. Consequently, the maximum discharge current of BS_2 is 58.3 A. The first battery stack and the first photovoltaic array, responsible for meeting SELAS energy requirements remain unchanged as expected, since SELAS power consumption remains consistent. In Figure 7-11 the power architecture of the system is presented.

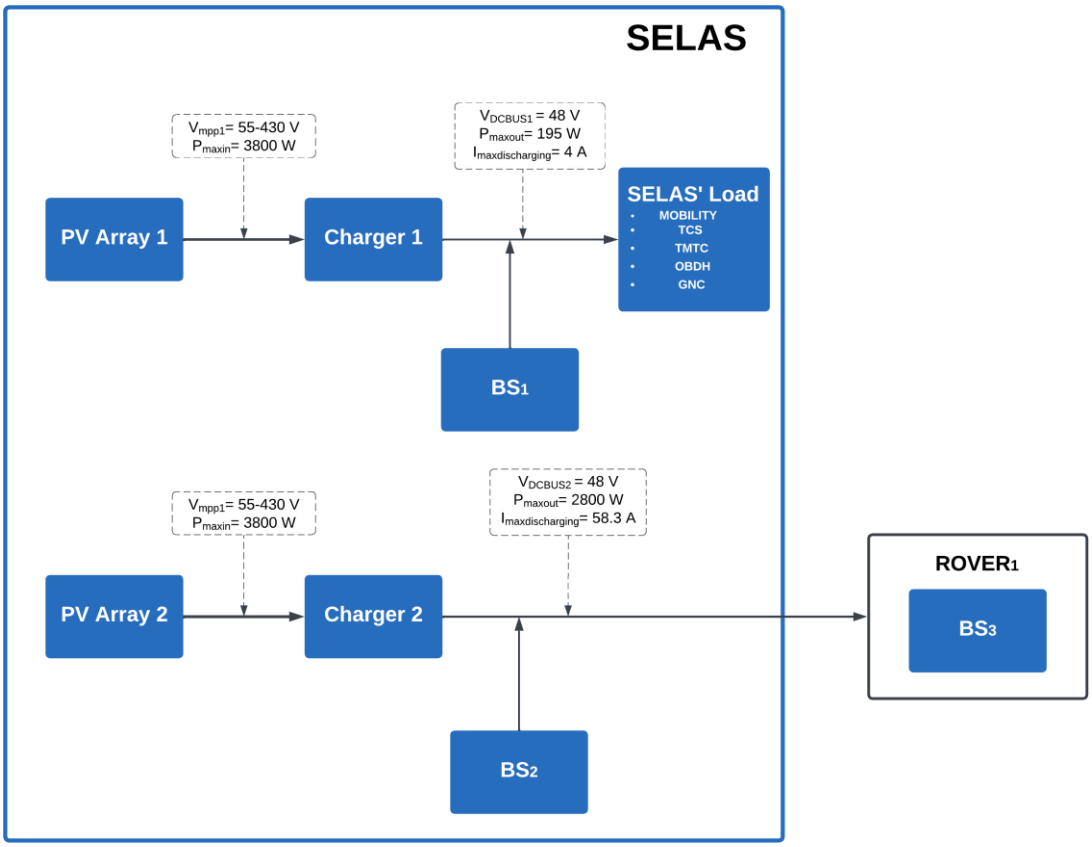

Figure 7-11. Power architecture of the system for Scenario 2.

The total area needed is 6.99 m^2 for PV array 1 and 8.748 m^2 for PV array 2. The power generated from the second photovoltaic array is presented in Figure 7-12. The output power of PV array 1 is the same as in Scenario 1.

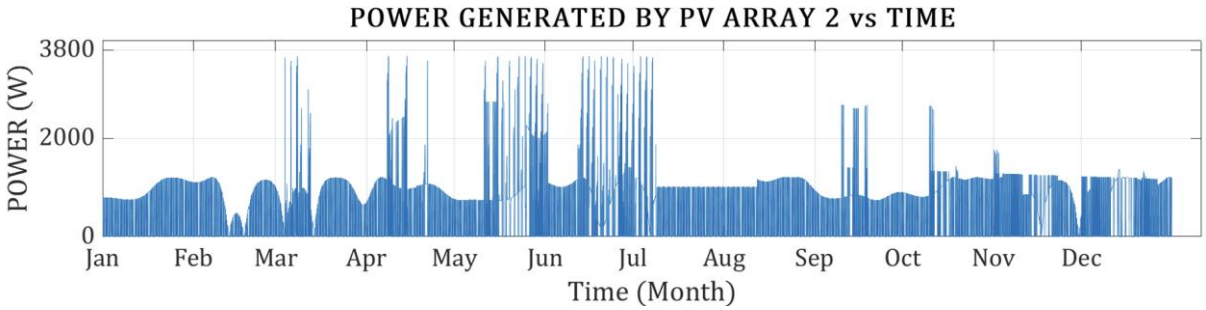

Figure 7-12. Power generated by PV array 2 during a year for Scenario 2.

The total system weight is 230,64 kg meaning that the launch vehicle mass for a power system like this would amount to at least 46,128 kg. Additionally, with transportation costs of $80,000 per kilogram for delivering a payload from Earth to the lunar surface, the total cost for this mission would be approximately $ 18,451,200. Additionally, the P_{avg} of the rover in Scenario 2, is 117.10 W, resulting in a power system-to-average power ratio of 1.96 kg/W. The detailed values are presented in Table 7-10.

Table 7-10. Total masses of the payload, the launch vehicle and total cost of the mission for Scenario 2.

Characteristic of Scenario 2	Value
System Mass	230.64 (kg)
Launch Vehicle Mass	46,128 (kg)
Total Cost	$ 18,451,200
Mass/P_{avg}	1.96 kg/W

The frequencies f_1, f_2, f_3 remain equal to 3, while f_4 remains equal to 1, resulting in the same charging schedule as expected. This is because the frequencies are determined by the geographical characteristics of the selected charging points rather than the power demands of the rover.

Similar to Scenario 1, the SoC of all battery stacks must remain higher than the 20% threshold. The SoC of BS_1 follows the same pattern as in Scenario 1, since there has been no change in

the battery sizing. Figure 7-13 depicts the SoC of BS_2, which consistently discharges to the 20% threshold to sustain BS_3, which remains predominantly fully charged (Figure 7-14). Exceptions occur during some winter months or periods of low illumination, exhibiting a pattern similar to that of BS_1.

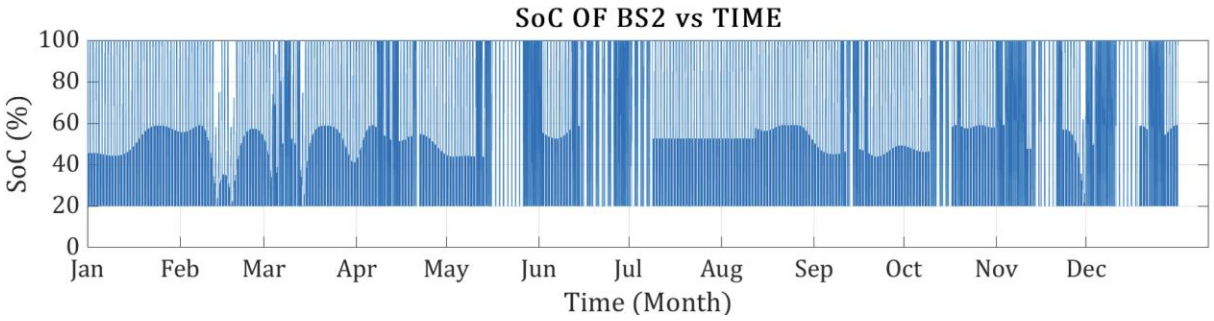

Figure 7-13. SoC of BS_2 during a year for Scenario 2.

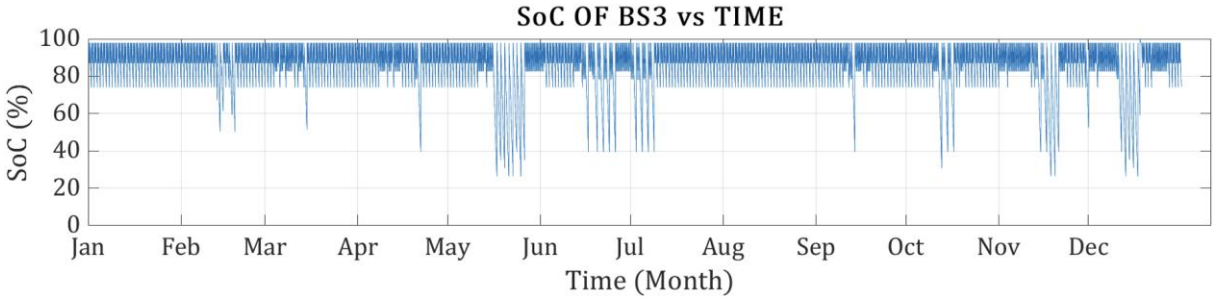

Figure 7-14. SoC of BS_3 during a year for Scenario 2.

7.3 Scenario 3 Results

Scenario 3 adopts a similar approach to Scenario 1, with the primary distinction being that the rover is additionally equipped with a drill, resulting in a significant increase in power consumption during the science phase. The outcome of the optimization algorithm is detailed in Table 7-11.

Table 7-11. Results of the optimization algorithm for Scenario 3.

Parameter	Optimal value
$N_{s,PVsBS1}$	3
$N_{p,PVsBS1}$	8
$N_{s,PVsProsp}$	3
$N_{p,PVsProsp}$	8
$N_{bat,BS1}$	85
$N_{bat,Prosp}$	18
$N_{bat,Rover}$	42
f_1	3
f_2	3
f_3	3
f_4	1

Table 7-12. Optimized values of all the devices and their mass for Scenario 3.

Device	Optimized value	Weight (kg)
Battery Stack 1	85	107.95
Battery Stack 2	18	22.86
Photovoltaic Array 1	24 (N_s= 3, N_p=8)	27.84
Photovoltaic Array 2	24 (N_s= 3, N_p=8)	27.84
Battery Stack 3	42	53.34

For this scenario, the maximum energy requested $E_{req}(t)$ from BS_2 during a single-hour charging session is also set to 2800 Wh. The first battery stack and the first photovoltaic array, responsible for meeting SELAS energy requirements, remain unchanged in this scenario as well. The power architecture of the system remains the same as in Scenario 2.

As in the two previous scenarios, the launch vehicle mass, the total cost, the mass of power system-to-power have been calculated and the corresponding results are presented in Table 7-13.

Table 7-13. Total masses of the payload, the launch vehicle and total cost of the mission for Scenario 3.

Characteristic of Scenario 3	Value
Payload Mass	237.53 (kg)
Launch Vehicle Mass	47,506 (kg)
Total Cost	$ 19,002,400
Mass/P_{avg}	1.81 kg/W

The SoC of all battery stacks was calculated and required to remain above the 20% threshold to validate the solution $\boldsymbol{X}$ as optimal. The SoC of BS_1 remains consistent with the two previous scenarios, while the SoC of BS_2 and BS_3 are illustrated in Figures 7-15 and 7-16, respectively. The SoC of BS_3 drops to its lowest value of approximately 30% briefly at the end of February. For the remainder of the year, the minimum SoC remains close to 40%.

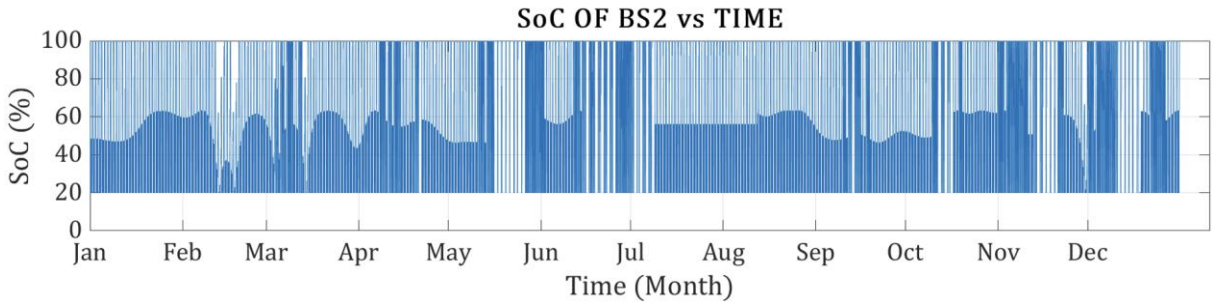

Figure 7-15. SoC of BS_2 during a year for Scenario 3.

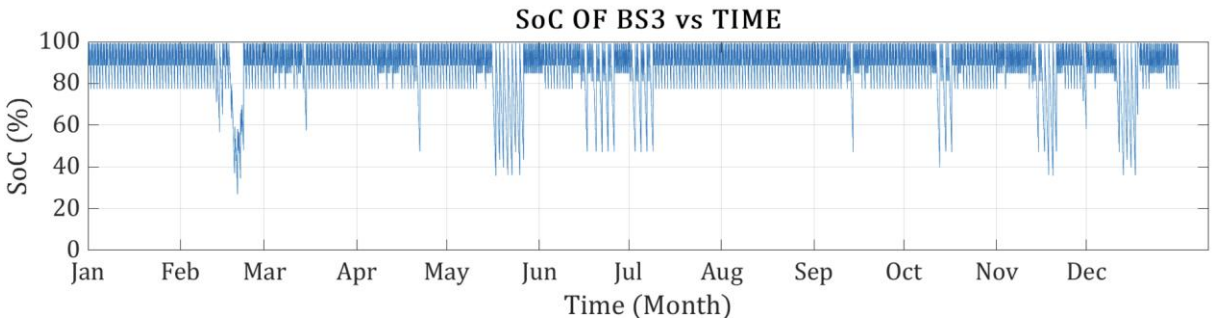

Figure 7-16. SoC of BS_3 during a year for Scenario 3.

7.4 Scenario 4 Results

Scenario 4 mirrors Scenario 3, with the inclusion of an additional 40 W heater integrated into the drill to measure downhole temperatures and assess thermal conductivity. This enhancement led to the addition of extra battery cells in both BS_2 and BS_3, while the photovoltaic arrays remained unchanged, along with the number of batteries in BS_1. The detailed outcomes of the optimization process are presented in Table 7-14.

Table 7-14. Results of the optimization algorithm for Scenario 4.

Parameter	Optimal value
$N_{s,PVsBS1}$	3
$N_{p,PVsBS1}$	8
$N_{s,PVsProsp}$	3
$N_{p,PVsProsp}$	8
$N_{bat,BS1}$	85
$N_{bat,Prosp}$	27
$N_{bat,Rover}$	52
f_1	3
f_2	3
f_3	3
f_4	1

Table 7-15. Optimized values of all the devices and their mass for Scenario 4.

Device	Optimized value	Weight (kg)
Battery Stack 1	85	107.95
Battery Stack 2	27	34.29
Photovoltaic Array 1	24 (N_s= 3, N_p=8)	27.84
Photovoltaic Array 2	24 (N_s= 3, N_p=8)	27.84
Battery Stack 3	52	66.04

For this scenario, the maximum energy requested $E_{req}(t)$ from BS_2 during a single-hour charging session is set to 2800 Wh. The power architecture of the system remains the same as in Scenarios 2 and 3.

Similar to the previous scenarios, the launch vehicle mass, total mission cost, and a mass of power system-to-power ratio were calculated. The detailed outcome is outlined in Table 7-16.

Table 7-16. Total masses of the payload, the launch vehicle and total cost of the mission for Scenario 4.

Characteristic of Scenario 2	Value
Payload Mass	259.23 (kg)
Launch Vehicle Mass	51,846 (kg)
Total Cost	$ 20,738,400
Mass/P_{avg}	1.681 kg/ W

The SoC of BS_2 and BS_3 are presented in Figures 7-17 and 7-18. Compared to the previous scenarios, the SoC of BS_2 exhibits slight differences, as it does not come as close to the 20% minimum threshold.

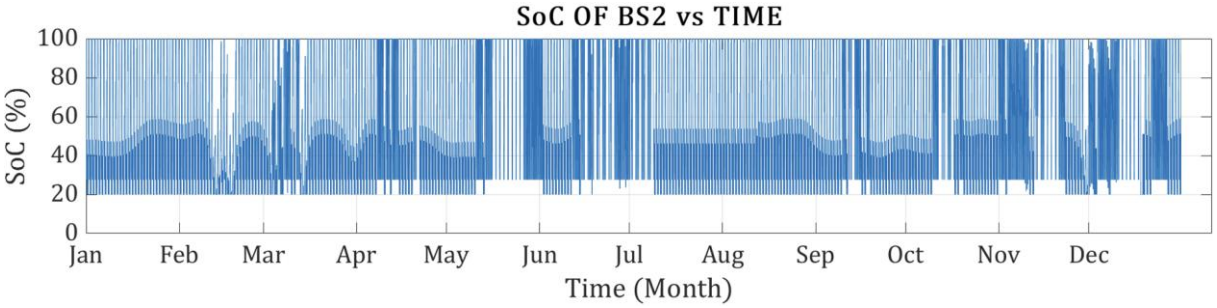

Figure 7-17. SoC of BS_2 during a year for Scenario 4.

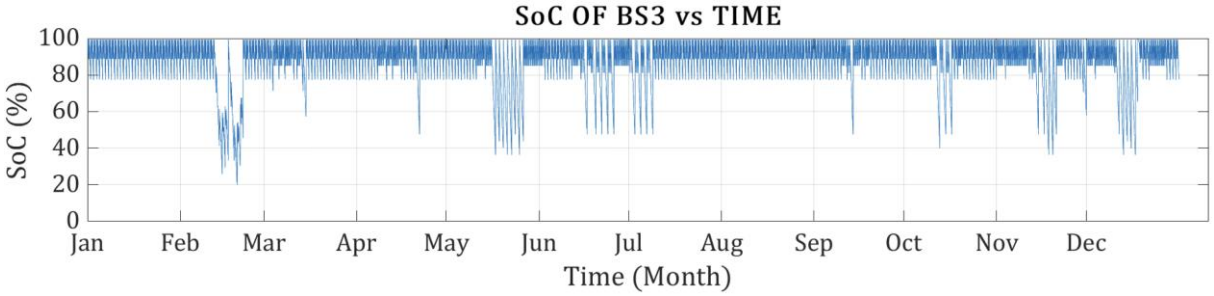

Figure 7-18. SoC of BS_3 during a year for Scenario 4.

7.5 Scenario 5 Results

In this scenario, the rover alternates between one hour of traversing with the NSS, NIRVSS, and MSolo instruments activated for route mapping, and one hour of drilling with all instruments fully operational. The heater has not been added in this case. Considering this schedule, the rover can traverse and map 8.64 km per day. Over a year, this translates to approximately 3,153 km covered and data collected from 4,380 drilling points.

The results of the optimization process are presented in Table 7-17

Table 7-17. Results of the optimization algorithm for Scenario 5.

Parameter	Optimal value
$N_{s,PVsBS1}$	3
$N_{p,PVsBS1}$	8
$N_{s,PVsProsp}$	3
$N_{p,PVsProsp}$	8
$N_{bat,BS1}$	85
$N_{bat,Prosp}$	26
$N_{bat,Rover}$	85
f_1	3
f_2	3
f_3	3
f_4	1

Table 7-18. Optimized values of all the device and their mass for Scenario 5.

Device	Optimized value	Weight (kg)
Battery Stack 1	85	107.95
Battery Stack 2	26	33.02
Photovoltaic Array 1	24 (N_s= 3, N_p=8)	27.84
Photovoltaic Array 2	24 (N_s= 3, N_p=8)	27.84
Battery Stack 3	85	107.95

For this scenario, the maximum energy requested $E_{req}(t)$ from BS_2 during a single-hour charging session is set to 2800 Wh. Consequently, the maximum discharge current of BS_2 is

58.3 A. The power architecture of the system remains consistent with that of Scenarios 2, 3, and 4. Additionally, the same charging schedule is implemented in this scenario.
The overall weight of the system is 300.14 kg, resulting in a launch vehicle mass of 60,028 kg and a total cost of $ 24,011,200. The mass-to-power ratio is 1.86 kg/W.

Table 7-19. Total masses of the payload, the launch vehicle and total cost of the mission for Scenario 5.

Characteristic of Scenario 2	Value
Payload Mass	300.14 (kg)
Launch Vehicle Mass	60,028(kg)
Total Cost	$ 24,011,200
Mass/P_{avg}	1.86 kg/ W

The SoC of BS_2 and BS_3 is depicted in Figures 7-19 and 7-20. Notably, the SoC of BS_3 remains above 60% for the majority of the time. The significant increase in the number of batteries in BS_3 compared to previous scenarios can be attributed to the extended period at the end of February when the only available charging points are the distant P_3 and P_4, requiring a considerable amount of time for traversal.

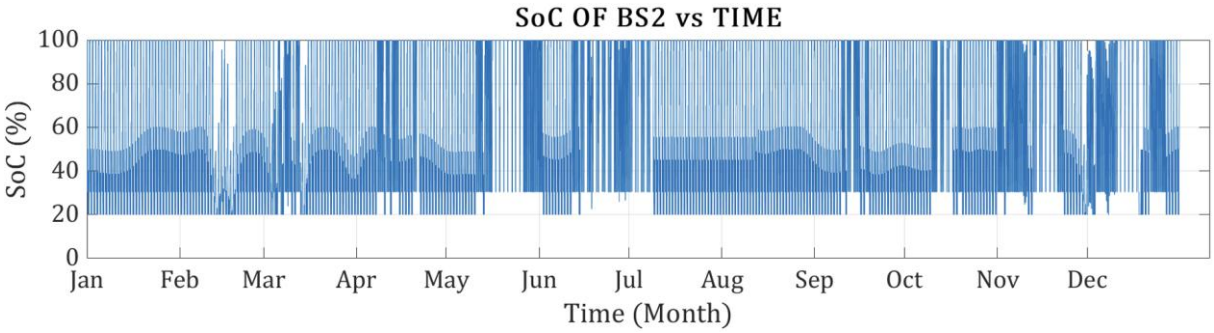

Figure 7-19. SoC of BS_2 during a year for Scenario 5.

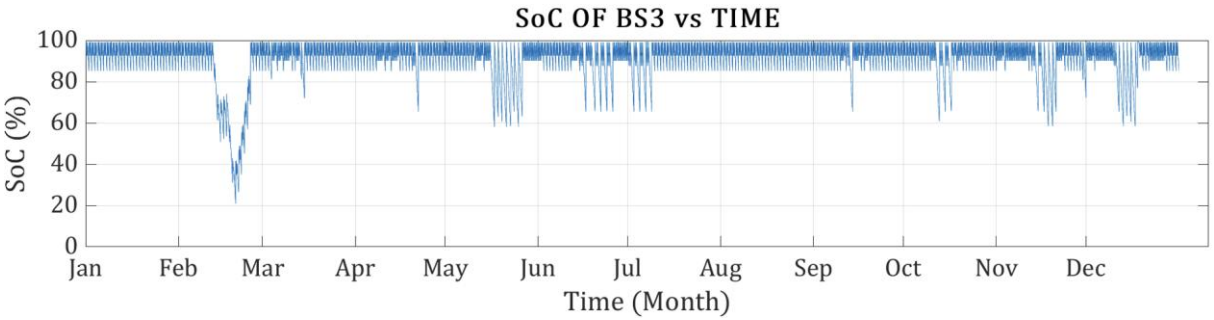

Figure 7-20. SoC of BS_4 during a year for Scenario 5.

7.6 Scenario 6 Results

In Scenario 6, SELAS is tasked with charging two rovers instead of one. The power consumption, instrumentation, and scheduling for both rovers, as well as for SELAS, are assumed to be identical to those described in Scenario 1. To enable simultaneous charging, the rovers may need to make minor adjustments to their planned paths to align with SELAS for recharging. Additionally, it is assumed that the battery stacks used in each rover (BS_3 and BS_5) are identical. Similarly, the battery stacks in SELAS designated for charging the rovers (BS_2 and BS_4), along with the photovoltaic arrays charging these battery stacks, are identical, as outlined in previous chapters. The results of the optimization process are detailed in Table 7-20.

Table 7-20. Results of the optimization algorithm for Scenario 6.

Parameter	Optimal value
$N_{s,PVsBS1}$	3
$N_{p,PVsBS1}$	8
$N_{s,PVsProsp}$	3
$N_{p,PVsProsp}$	6
$N_{bat,BS1}$	85
$N_{bat,Prosp}$	13
$N_{bat,Rover}$	24
f_1	3
f_2	3
f_3	3
f_4	1

Table 7-21. Optimized values of all the devices and their mass for Scenario 6.

Device	Optimized value	Weight (kg)
Battery Stack 1	85	107.95
Battery Stack 2	13	16.51
Battery Stack 4	13	16.51
Photovoltaic Array 1	24 (N_s= 3, N_p=8)	27.84
Photovoltaic Array 2	18(N_s= 3, N_p=6)	20.88
Photovoltaic Array 3	18 (N_s= 3, N_p=6)	20.88
Battery Stack 3	24	30. 48
Battery Stack 5	24	30. 48

For this scenario, the maximum energy requested $E_{req}(t)$ from BS_2 and BS_4 during a single-hour charging session is set to 1800 Wh. Consequently, the maximum discharge current of the batteries is 37.5 A. The power architecture of the system is presented in Figure 7-21.

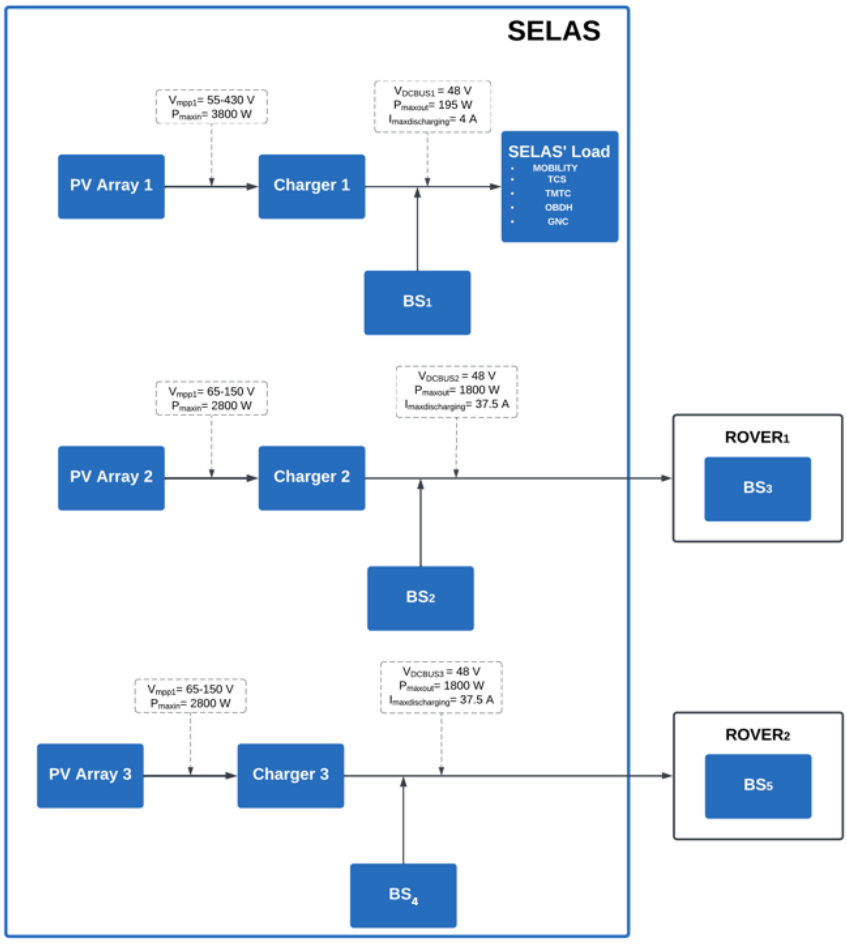

Figure 7-21. Power architecture of the system for Scenario 6.

The charging schedule for the rovers remains consistent with the previous scenarios. The total area of the first photovoltaic array is 6.16 m², while the second and third arrays each cover an

area of 5.24 m². In Figure 7-22 the power generated by the second photovoltaic array is presented. The power generated by the third PV array is identical.

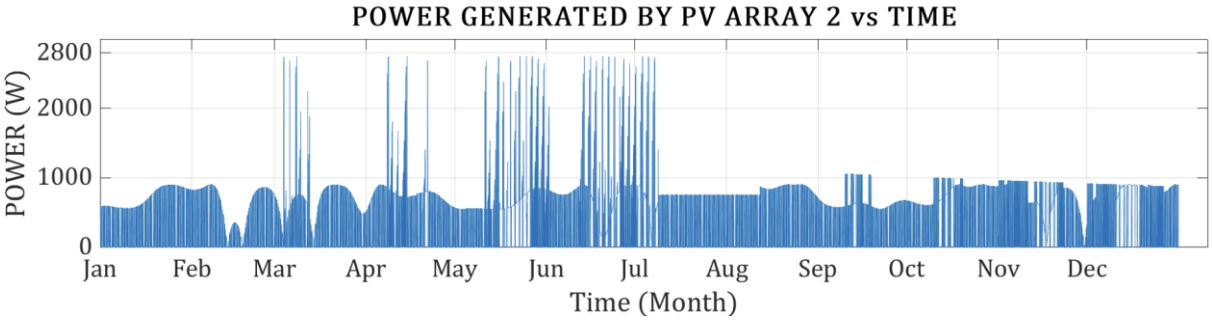

Figure 7-22. Power generated by PV array 2 during a year for Scenario 6.

The system's total weight has been calculated to be 268.35 kg, which requires a minimum launch vehicle mass of 53,670 kg. Consequently, the total mission cost is estimated at $21,468,00 Additionally, the average power that both of the rovers consume is 177.1 W that gives a mass-to-power ratio of 1.51 kg/W.

Table 7-22. Total masses of the payload, the launch vehicle and total cost of the mission for Scenario 6.

Characteristic of Scenario 6	Value
Payload Mass	268.35 (kg)
Launch Vehicle Mass	53,670 (kg)
Total Cost	$ 21,468,00
Mass/P_{avg}	1.51 kg/W

The SoC of BS_2 and BS_3 are presented in Figures 7-23 and 7-24. They are identical to those in Scenario 1, as expected, as the power consumption and the sizing is the same. Same goes with BS_4 and BS_5.

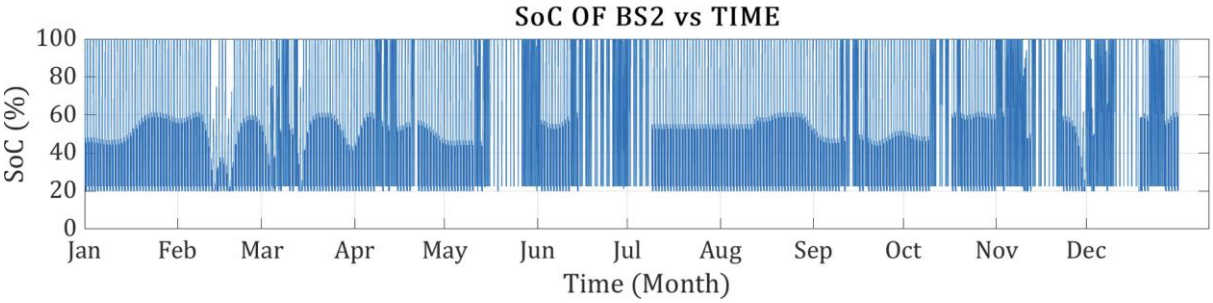

Figure 7-23. SoC of BS_2 during a year for Scenario 6.

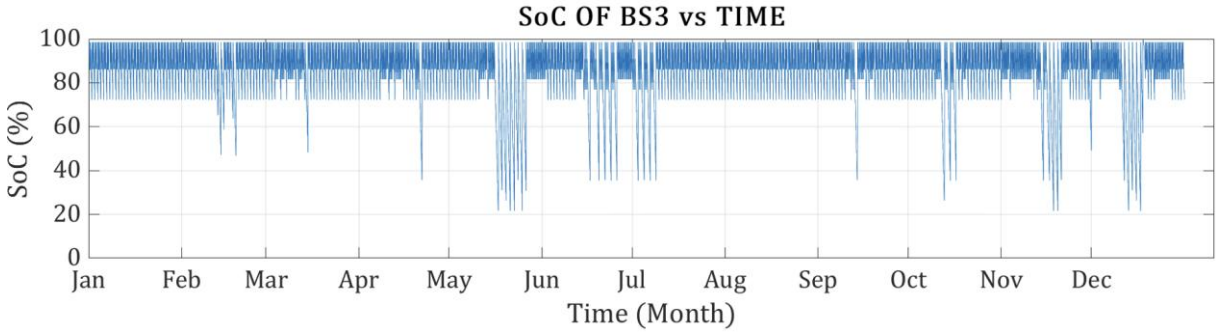

Figure 7-24. SoC of BS_3 during a year for Scenario 6.

7.7 Scenario 7 Results

In this scenario, SELAS is charging two rovers, that both have the same instrumentation, power consumption and scheduling as described in Scenario 2. The instruments are operating continuously, even during the charging phase enabling comprehensive data collection over 30.24 km per day and 11,036 km per year with a system that includes one SELAS and two rovers.

The results of the optimization process are shown in Table 7-23.

Table 7-23. Results of the optimization algorithm for Scenario 7.

Parameter	Optimal value
$N_{s,PVsBS1}$	3
$N_{p,PVsBS1}$	8
$N_{s,PVsProsp}$	3
$N_{p,PVsProsp}$	8
$N_{bat,BS1}$	85
$N_{bat,Prosp}$	20
$N_{bat,Rover}$	35
f_1	3
f_2	3
f_3	3
f_4	1

Table 7-24. Optimized values of all the devices and their mass for Scenario 7.

Device	Optimized value	Weight (kg)
Battery Stack 1	85	107.95
Battery Stack 2	20	25.40
Battery Stack 4	20	25.40
Photovoltaic Array 1	24 (N_s= 3, N_p=8)	27.84
Photovoltaic Array 2	24 (N_s= 3, N_p=8)	27.84
Photovoltaic Array 3	24 (N_s= 3, N_p=8)	27.84
Battery Stack 3	35	44.45
Battery Stack 5	35	44.45

For this scenario, the maximum energy requested $E_{req}(t)$ from BS_2 and BS_3 during a single-hour charging session is set to 2800 Wh. Consequently, the maximum discharge current of the battery stacks is 58.3 A. The power architecture of the system is presented in Figure 7-25.

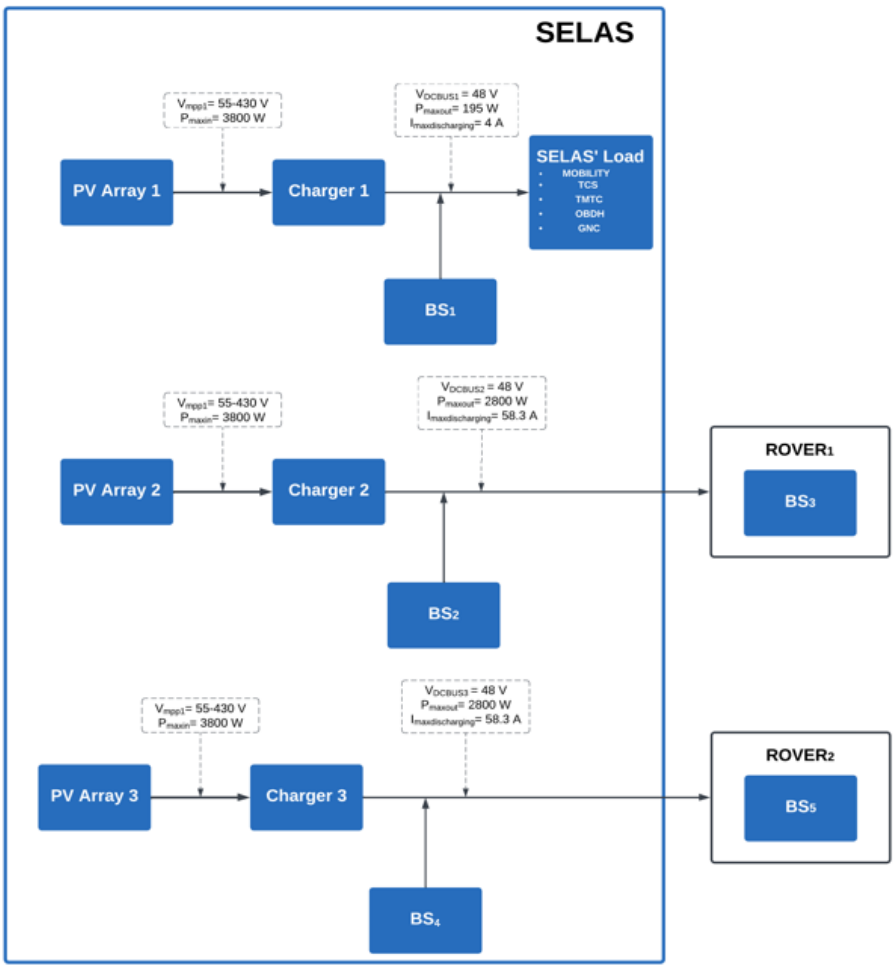

Figure 7-25. Power architecture of the system for Scenario 7.

The charging schedule for the rovers remains consistent with the previous scenarios. The total area of the first photovoltaic array is 6.99 m², while the second and third arrays each cover an area of 6.99 m². In Figure 7-26 the power generated by the second photovoltaic array is presented. The power generated by the third PV array is identical.

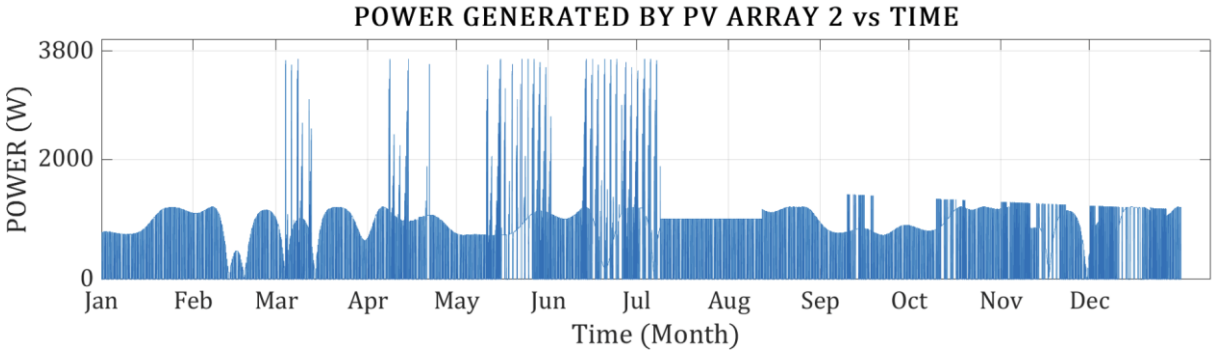

Figure 7-26. Power generated by PV array 2 during a year for Scenario 7.

The total mass of the system is 322.29 kg, the minimum mass of the launch vehicle would be 64,458 kg while the total cost of the mission would be $ 25,783,200. The results are summarized in Table 7-25.

Table 7-25. Total masses of the payload, the launch vehicle and total cost of the mission for Scenario 7.

Characteristic of Scenario 7	Value
Payload Mass	322.29 (kg)
Launch Vehicle Mass	64,458 (kg)
Total Cost	$ 25,783,200
Mass/P_{avg}	1.37 kg/W

The SoC of BS_2 and BS_3 are presented in Figures 7-27 and 7-28. They are identical to those in Scenario 2, as expected, as the power consumption and the sizing is the same. The same applies to BS_4 and BS_5, respectively.

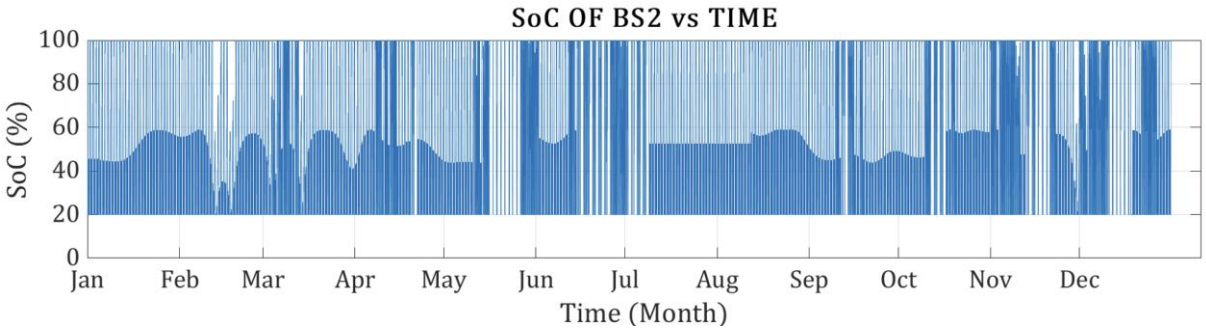

Figure 7-27. SoC of BS_2 during a year for Scenario 7.

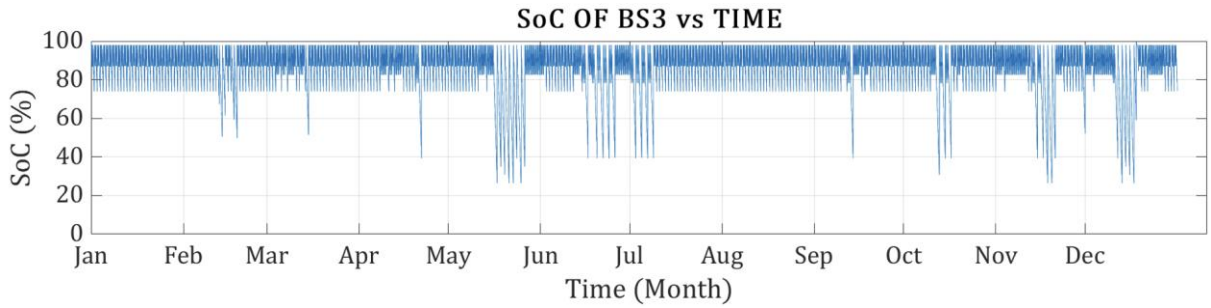

Figure 7-28. SoC of BS_3 during a year for Scenario 7.

9.8 Scenario 8 Results

In the last scenario examined, SELAS is charging two rovers with the same instrumentation, power consumption and scheduling as in Scenario 5. Each rover is alternating modes every one hour, between traversing for one hour with the NSS, NIRVSS, and MSolo instruments activated for route mapping, and one hour of drilling with all instruments fully operational. The heater has not been added in this case. Considering this schedule, both rovers can traverse and map 17.28 km per day. Over a year, this translates to approximately 6,307 km covered and data collected from 8,760 drilling points.

Table 7-26. Results of the optimization algorithm for Scenario 8.

Parameter	Optimal value
$N_{s,PVsBS1}$	3
$N_{p,PVsBS1}$	8
$N_{s,PVsProsp}$	3
$N_{p,PVsProsp}$	8
$N_{bat,BS1}$	85
$N_{bat,Prosp}$	26
$N_{bat,Rover}$	85
f_1	3
f_2	3
f_3	3
f_4	1

Table 7-27. Optimized values of all the devices and their mass for Scenario 8.

Device	Optimized value	Weight (kg)
Battery Stack 1	85	107.95
Battery Stack 2	26	33.02
Battery Stack 4	26	33.02
Photovoltaic Array 1	24 (N_s= 3, N_p=8)	27.84
Photovoltaic Array 2	24 (N_s= 3, N_p=8)	27.84
Photovoltaic Array 3	24 (N_s= 3, N_p=8)	27.84
Battery Stack 3	85	107.95
Battery Stack 5	85	107.95

The maximum energy requested $E_{req}(t)$ from BS_2 and BS_3 during a single-hour charging session is set to 2800 Wh with the maximum discharge current to be 58.3 A. The power architecture of the system is identical to the one presented in Scenario 7. The power produced by the photovoltaic arrays has been the same as well, as there is no change in the sizing compared to Scenario 7. No changes have been made to the charging schedule as well.

The overall mass of the system is 461.29 kg, the minimum mass of the launch vehicle would be 92,258 kg while the total cost of the mission would be $ 36,903,200. The results are presented in Table 7-28.

Table 7-28. Total masses of the payload, the launch vehicle and total cost of the mission for Scenario 8.

Characteristic of Scenario 8	Value
Payload Mass	461.29 (kg)
Launch Vehicle Mass	92,258 (kg)
Total Cost	$ 36,903,200
Mass/P_{avg}	1.43 kg/W

The SoC of BS_2 and BS_3 are presented in Figures 7-28 and 7-29. They are identical to those in Scenario 5, as expected, since the power consumption and the sizing is the same. The same applies to BS_4 and BS_5, respectively.

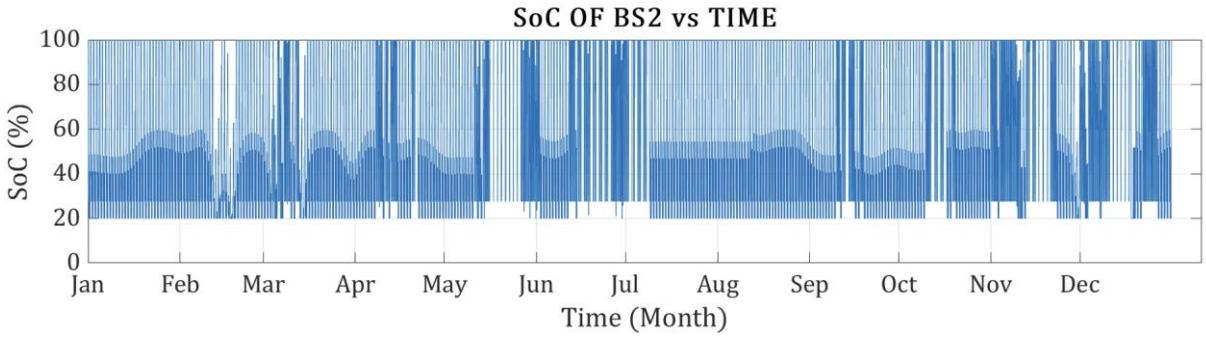

Figure 7-29. SoC of BS_2 during a year for Scenario 8.

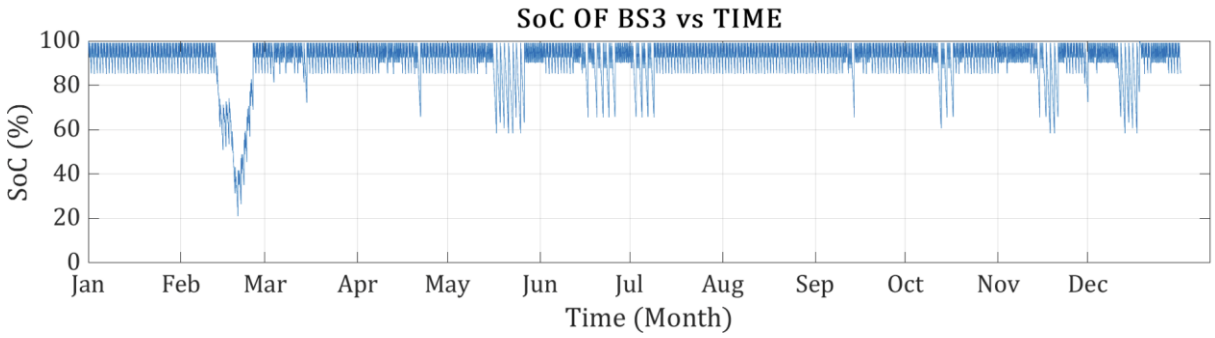

Figure 7-30. SoC of BS_3 during a year for Scenario 8.

8

Discussion of the Results & Conclusions

8.1 Interpretation of the Results

The simulations performed have delivered an in depth review of SELAS performance in various scenarios that vary in instrumentation, scheduling, science outcome and power consumption. SELAS has managed in each case to keep the rover operational inside a PSR for a year, with the SoC of the rover's battery stack to remain mostly above 40% or even 60 % in some cases, increasing the system's redundancy and life duration. Additionally, this is achieved with high TRL technologies and off-the shelf devices keeping the concept realistic.

Based on the optimization results in Chapter 7, the considerable battery size of SELAS is a direct consequence of the high energy demands imposed by the required 10 km/h speed, which is essential for the fast charging of the rover but leads to substantial power consumption during the traverse phase. Additionally, it is notable that the number of photovoltaic panels remains relatively consistent across the different scenarios, with the primary variation being in the size of the battery stacks. This is likely due to the limitations of the selected chargers MPPT voltage range, as increasing the power output would necessitate adding more photovoltaic panels in series to elevate the voltage level.

Lastly, the calculated launch cost is based on conventional technologies rather than novel approaches like the reusable SpaceX Starship. This suggests that the actual cost of deploying SELAS could potentially be much lower with advancements in launch technology.

Based on the previous analysis from Chapter 7, the total mass of the power system-to-average power consumed by the rovers will be used as an indicator to compare the various scenarios and determine the conditions under which a power system like SELAS would yield the best results. The results of all scenarios are presented in Table 8-1.

The most efficient system in the analyzed scenarios is identified as the one with the lowest ratio value, as a lighter system is advantageous for supporting higher power consumption. Scenario 7 emerges as the most efficient with a ratio of 1.37 kg/W, followed by Scenario 8 at 1.43 kg/W, and Scenario 6 at 1.51 kg/W. The remaining scenarios exhibit less favorable outcomes, with ratios ranging from 1.68 to 2.38, with Scenario 1 yielding the least efficient result. These findings underscore that SELAS is more suitable for facilitating multiple rovers rather than a single one, proving SELAS potentials on swarm missions. This conclusion is expected, as the addition of a PV array, a battery stack, and a charger can support an additional rover without the need for an entirely new SELAS system. Additionally, SELAS would prove to be more effective in supporting long-duration missions that extend beyond a lunar day, thereby necessitating external charging. This capability would be essential for missions operating in permanently shadowed regions (PSRs) or in lunar locations subjected to a period of total darkness for at least 14 days due to the lunar night. For missions, shorter than a lunar day, a mounted power system on the rover itself would be more cost-effective.

From the state of charge figures of the batteries, SELAS successfully kept both itself and the rover operational under all scenarios, regardless of whether the $\text{Total Mass}/P_{avg}$ was optimal, during a year. As demonstrated in paragraph 7.1, SELAS could endure and maintain functionality during 17 hours of total darkness, without any charging point available, although not at full operational capacity. If the challenges of photovoltaic degradation due to radiation and the limited battery lifetime (particularly of the secondary battery stack) are addressed, SELAS has the potential to operate for significantly longer durations, beyond a single year.

Table 8-1. Total Mass/P_{avg} ratio for all scenarios.

Scenario	$Total\ Mass/P_{avg}\ (\frac{kg}{W})$	Total Power System Mass (kg)	$P_{avg}\ (W)$
1	2.38	203.67	88.55
2	1.96	230.64	117.10
3	1.81	237.53	131.05
4	1.68	259.23	153.55
5	1.86	300.14	161.10
6	**1.51**	**268.35**	**177.10**
7	**1.37**	**322.29**	**234.20**
8	**1.43**	**461.29**	**322.20**

For comparison, NASA's VIPER rover could operate in PSRs for only 6 hours using photovoltaics, or potentially for up to 18 months with a radioisotope power source [117] covering over 100 km during that time. However, in that case, VIPER would face challenges associated with nuclear power, as discussed in paragraph 2.3.2. Based on the results of this thesis, SELAS demonstrates the ability to outperform traditional PV-battery systems for rovers engaged in prospecting missions. Furthermore, SELAS offers a safer and more technologically mature alternative to nuclear power sources. A compliance matrix comparing all available technologies against SELAS is presented in Table 8-2, based on the analysis in Chapter 2.

Table 8-2. Compliance matrix for different lunar power systems compared to SELAS.

Power System	Lunar Night Coverage	Redundancy	Pollution	Cost	Feasibility	Safety
PVs + Fuel Cells	×	×	✓	×	×	✓
PVs + Batteries	×	×	✓	✓	✓	✓
RTGs	✓	✓	×	×	×	×
SELAS	✓	✓	✓	✓	✓	✓

8.2 Future Work

SELAS is capable of delivering an innovative solution for supporting long-duration rover missions in PSR regions, offering flexibility, adaptability and cost-effectiveness to overcome the harsh lunar environment. This thesis lays the groundwork and emphasizes the need for further research in this area. One avenue for improvement involves adapting the power architecture used in Scenarios 6, 7, and 8 (with 3 PV arrays and 3 battery stacks) for Scenarios 1–5, where SELAS charges only one rover. The additional photovoltaic array and battery could serve as a redundancy system, ensuring continued operation in case of a system fault or complete loss of one photovoltaic array or battery stack. Although this would increase the $\mathrm{Mass}/\mathrm{P}_{\mathrm{avg}}$ ratio, the enhanced reliability could offset this trade-off. Additionally, a more sophisticated power architecture should be considered, including more converters and DC buses to support loads with lower voltage levels.

To address potential size constraints with more than two PV arrays on a single SELAS, foldable structures could be considered, though mitigating dust-related issues in mechanical parts would be critical. Exploring more advanced PV configurations, such as elevating PV arrays mechanically to heights of up to 10 meters, could significantly improve illumination conditions and reduce night duration in some locations [25]. A more comprehensive thermal analysis of SELAS is also necessary to evaluate the impact of extreme temperature fluctuations and ensure system survivability.

The traverse algorithm could be enhanced using AI or real-time data retrieval from the lunar surface to dynamically identify illuminated points and paths, addressing the challenge of SoC

drops when SELAS travels long distances to recharge. The Mass/Power ratios demonstrate that SELAS is most efficient when charging multiple rovers, providing a foundation for future studies on swarm operations with integrated SELAS vehicles. Developing algorithms to coordinate multiple SELAS units would further optimize the system's performance.

Expanding SELAS' capabilities to more demanding environments, such as high slopes or rocky terrains, could involve rethinking its robotic configuration. Simulations in challenging locations, like Malapert Mountain or Shackleton Crater, should be performed to test SELAS robustness under extreme conditions. Additionally, SELAS could be adapted for exploring lunar lava tubes or caves, which offer stability, minimal temperature variations, and micrometeorite protection—ideal conditions for human bases. While conventional PV systems are unsuitable for these settings, SELAS could serve as an efficient alternative to RTGs.

Finally, SELAS' concept could be extended to missions on other celestial bodies, including Mars, Io, Europa, or Titan, where similar challenges in energy management and autonomy exist. Such adaptability positions SELAS as a versatile solution for future space exploration missions.

Literature

[1] NASA, “NASA’s Lunar Exploration Program Overview,” September 2020.

[2] Y. Lin, W. Yang, H. Zhang, H. Hui, S. Hu, L. Xiao, J. Liu, Z. Xiao, Z. Yue, J. Zhang, et al., “Return to the Moon: New perspectives on lunar exploration,” Science Bulletin, vol. 69, no. 13, pp. 2136-2148, 2024. DOI: 10.1016/j.scib.2024.04.051.

[3] N. J. Bennett, D. Ellender, and A. G. Dempster, “Commercial viability of lunar In-Situ Resource Utilization (ISRU),” Planetary and Space Science, vol. 182, p. 104842, 2020. DOI: 10.1016/j.pss.2020.104842.

[4] L. Schlüter and A. Cowley, “Review of techniques for In-Situ oxygen extraction on the moon,” Planetary and Space Science, vol. 181, p. 104753, 2020. DOI: 10.1016/j.pss.2019.104753.

[5] J. Biswas, P. Q. Malzone, and F. Rößler, “Energy storage selection and operation for night-time survival of small lunar surface systems,” Acta Astronautica, vol. 185, pp. 308-318, 2021. DOI: 10.1016/j.actaastro.2021.04.042.

[6] A. Petro, “Surviving and Operating Through the Lunar Night,” in 2020 IEEE Aerospace Conference, Big Sky, MT, USA, 2020, pp. 1-6. DOI: 10.1109/AERO47225.2020.9172730.

[7] S. Ulamec, J. Biele, and E. Trollope, “How to Survive a Lunar Night,” *Planetary and Space Science*, vol. 58, pp. 1985–1995, 2010. DOI: 10.1016/j.pss.2010.09.024.

[8] J. F. Clawson, “Thermal Environments,” *JPL D-8160*, 1991.

[9] S. Huang, “Surface Temperatures at the Nearside of the Moon as a Record of the Radiation Budget of Earth’s Climate System,” *Advances in Space Research*, vol. 41, pp. 1853–1860, 2008.

[10] M. Harrell, G. Schroeder, and S. Daire, “Lunar Environment, Overview,” Handbook of Life Support Systems for Spacecraft and Extraterrestrial Habitats, May 2021. DOI: 10.1007/978-3-319-09575-2_15-1.

[11] S. A. Stern, “The Lunar Atmosphere: History, Status, Current Problems, and Context,” *Reviews in Geophysics*, vol. 37, no. 4, pp. 453–491, 1999. DOI: 10.1029/1999RG900005.

[12] H. Hiesinger and R. Jaumann, “The Moon,” in *Encyclopedia of the Solar System*, 3rd ed., T. Spohn, D. Breuer, and T. V. Johnson, Eds., Elsevier, 2014, pp. 493–538. DOI: 10.1016/B978-0-12-415845-0.00023-2.

[13] P. Eckart, *The Lunar Base Handbook*, 2nd ed., Space Technology Series, 2006.

[14] J. D. Carpenter, R. Fisackerly, D. De Rosa, and B. Houdou, “Scientific Preparations for Lunar Exploration with the European Lunar Lander,” *Planetary and Space Science*, vol. 74, pp. 208–223, 2012.

[15] M. Kruijff, “The Peaks of Eternal Light on the Lunar South Pole: How They Were Found and What They Look Like,” *Fourth International Conference on Exploration and Utilisation of the Moon (ICEUM 4)*, July 2000.

[16] V. Maiwald, “Being Selene’s Guest: Analysis of the Lunar Environment and Its Impact on Base Location Selection,” *Proceedings of the International Astronautical Congress (IAC)*, vol. 3, 2013.

[17] G. Reitz, T. Berger, and D. Matthiae, “Radiation Exposure in the Moon Environment,” *Planetary and Space Science*, vol. 74, pp. 78–83, 2012.

[18] J. W. Howard, D. M. Hardage, “Space Radiation and Its Effects on Electronic Systems,” NASA Technical Report NASA/TP-1999-209373, 1999.

[19] C. J. Ahrens and N. E. Petro, “Mapping Thermal Flux Boundaries Surrounding Permanently Shadowed Regions (PSRs) at the Lunar South Pole,” *Lunar Polar Volatiles Workshop*, NASA Goddard Space Flight Center, Greenbelt, MD, 2022.

[20] J. Feng and M. A. Siegler, “Reconciling the Infrared and Microwave Observations of the Lunar South Pole: A Study on Subsurface Temperature and Regolith Density,” *Journal of Geophysical Research: Planets*, vol. 126, 2021. DOI: 10.1029/2020JE006623.

[21] D. Ivanov and D. Fernandes, “Thermal Control of a Lightweight Rover System in the Permanently Shadowed Regions of the Lunar South Pole,” Ispace Europe, Luxembourg, 2020.

[22] P. Berkelman, M. Chen, J. Easudes, J. Hancock, M. Martin, A. Mor, E. Rollins, A. Sharf, J. Silberman, T. Warren, and D. Bapna, “Design of a Day/Night Lunar Rover,” 1998.

[23] E. Mazarico, M. K. Barker, A. M. Jagge, et al., “Sunlit pathways between south pole sites of interest for lunar exploration,” *Acta Astronautica*, vol. 204, pp. 49-57, 2023. DOI: 10.1016/j.actaastro.2022.12.023.

[24] Y. Huang et al., “Slope Stability Analysis and Soil Mechanical Properties of Impact Craters Around the Lunar South Pole,” *Remote Sensing*, vol. 16, no. 2, 2024. DOI: 10.3390/rs16020371.

[25] E. Mazarico et al., “Illumination Conditions of the Lunar Polar Regions Using LOLA Topography,” *Icarus*, vol. 211, no. 2, pp. 1066–1081, 2011. DOI: 10.1016/j.icarus.2010.10.030.

[26] J. Martin, C. Hanner, N. Bolatto, and D. L. Akin, “TRAVELS: A Multimodal Mobility Concept for Highly Capable Planetary Traverses,” *AIAA 2022-4397, Session: Lunar Surface Operations VIII: Traverses*, Oct. 15, 2022. DOI: 10.2514/6.2022-4397..

[27] M. Kaufmann et al., “CopilotMIKE: An Autonomous Assistant for Multi-Robot Operations in Cave Exploration,” in *2021 IEEE Aerospace Conference*, 2021. DOI: 10.1109/AERO50100.2021.9438530.

[28] P. Fankhauser and M. Hutter, “ANYmal: A Unique Quadruped Robot Conquering Harsh Environments,” *Research Features*, no. 126, pp. 54–57, 2018.

[29] D. S. McKay et al., “The Lunar Regolith,” in *Lunar Sourcebook: A User’s Guide to the Moon*, Cambridge University Press, 1991, pp. 285–356.

[30] D. Budzyń, E. Tuohy, N. Garrivier, T. Schild, A. Cowley, R. Cruise, M. Adachi, H. Zare-Behtash, and A. Cammarano, “Lunar dust: Its impact on hardware and mitigation technologies,” in *Proceedings of the 46th Aerospace Mechanism Symposium*, E. A. Boesiger and J. P. Wood, Eds., 2022, pp. 287–300.

[31] M. Z. Yousaf, “The Importance of DC Grid Protection in Lunar Microgrids: Overcoming Environmental Challenges,” *TechRxiv*, Dec. 2024. DOI: 10.36227/techrxiv.173385674.47262042/v1.

[32] P. B. Abel, M. D. Anderson, E. T. Blom, C. Calle, P. H. Dunlap, P. S. Greenberg, D. G. Fischer, S. A. Howard, K. M. Hurlbert, J. L. Jordan, et al., *Lunar Dust Mitigation: A Guide and Reference (First Edition)*, NASA Glenn Research Center, 2023. (NASA/TP-20220018746).

[33] J. Herman, S. Sadick, M. Maksymuk, and P. Chu, “Dust-Tolerant Connector Development for Lunar Surface Systems,” 2009. DOI: 10.2514/6.2009-6583.

[34] S. Sadick, J. Herman, and D. Roberts, “Dust-Tolerant Electrical Connector,” U.S. Patent Application, US 2010/0233895 A1, Sept. 2010.

[35] M. Brown, A. K. Boyd, B. W. Denevi, M. R. Henriksen, M. R. Manheim, M. S. Robinson, E. J. Speyerer, and R. V. Wagner, “Resource potential of lunar permanently shadowed regions,” *Icarus*, vol. 377, p. 114874, 2022. DOI: 10.1016/j.icarus.2021.114874.

[36] Jia, Yutong & Liu, Lei & Wang, Xingchen & Guo, Ningbo & Wan, Gang. (2022). Selection of Lunar South Pole Landing Site Based on Constructing and Analyzing Fuzzy Cognitive Maps. *Remote Sensing*. 14. 4863. 10.3390/rs14194863.

[37] J. Haruyama, M. Ohtake, T. Matsunaga, T. Morota, C. Honda, Y. Yokota, et al., “Lack of exposed ice inside lunar south pole Shackleton crater,” *Science*, vol. 322, no. 5903, pp. 938–939, 2008. DOI: 10.1126/science.1164020.

[38] P. D. Spudis, B. Bussey, J. Plescia, J. Josset, and S. Beauvivre, “Geology of Shackleton crater and the south pole of the Moon,” *Geophysical Research Letters*, vol. 35, 2008. DOI: 10.1029/2008GL034468.

[39] S. Halim, N. Barrett, S. Boazman, A. Gawronska, C. Gilmour, K. McCanaan, A. V. Satyakumar, J. Shah, and D. Kring, “Numerical modeling of the formation of Shackleton crater at the lunar south pole,” *Icarus*, vol. 354, 2020. DOI: 10.1016/j.icarus.2020.113992.

[40] J.-P. Williams, P. Mahanti, M. S. Robinson, R. V. Wagner, M. Chertok, N. Schörghofer, E. Mazarico, B. W. Denevi, S. Li, and D. A. Paige, “The Faustini Permanently Shadowed Region on the Moon,” *The Planetary Science Journal*, vol. 5, no. 9, 2024. DOI: 10.3847/PSJ/ad6f0d.

[41] E. A. Kozlova and E. N. Lazarev, “Crater Cabeus as Possible Cold Trap for Volatiles Near South Pole of the Moon,” *41st Lunar and Planetary Science Conference*, The Woodlands, Texas, Mar. 2010. .

[42] G. Leone, C. Ahrens, J. Korteniemi, D. Gasparri, A. Kereszturi, A. Martynov, G. W. Schmidt, G. Calabrese, and J. Joutsenvaara, “Sverdrup-Henson crater: A candidate location for the first lunar South Pole settlement,” *iScience*, vol. 26, no. 10, p. 107853, 2023. DOI: 10.1016/j.isci.2023.107853.

[43] L.-J. Burtz, F. Dubois, and O. Gasquez, “Finding the North on a Lunar Microrover: A Lunar Surface Environment Simulator for the Development of Vision-Based Navigation Pipelines,” *69th International Astronautical Congress (IAC)*, Bremen, Germany, Oct. 2018

[44] A. Calzada Diaz, D. Bolan, and M. Puntar, "Mission Planning for a Lunar Polar Mission: ISPACE's Polar Ice Explorer," *1st Lunar and Planetary Science Conference*, ispace Europe, Luxembourg, 2020.

[45] T. Oikawa, A. Almujahed, R. Rolley, T. Whitaker, C. Fuente, T. Arbuckle, K. Quinn, A. Davis, C. Rampolla, J. Spoto, G. Purnell, J. Landrenaeu, and M. Provenzano, "Plan and Progression of the Technology Readiness Level of the CubeRover," *74th International Astronautical Congress (IAC)*, Baku, Azerbaijan, Oct. 2023.

[46] G. Tsakyridis, C. Lange, S. S. Jahnke, L. Witte, N. Toth, M. Scharringhausen, and N. I. Xiros, "Power System Analysis and Optimization of a Modular Experiment Carrier During an Analog Lunar Demo Mission on a Volcanic Environment," *Acta Astronautica*, vol. 155, pp. 200–210, 2019. DOI: 10.1016/j.actaastro.2018.11.034.

[47] R. A. Beyer, A. Colaprete, M. Shirley, E. Balaban, M. Siegler, and J. MartinezCamacho, "VIPER Site Selection," *3rd Lunar and Planetary Science Conference*, NASA Ames Research Center, Moffett Field, CA, 2022.

[48] A. Colaprete, D. Lim, and K. Ennico-Smith, "Volatiles Investigating Polar Exploration Rover Proposal Information Package (PIP)," NASA, Jan. 2020.

[49] K. Ennico-Smith, A. Colaprete, R. Elphic, J. Captain, J. Quinn, and K. Zachny, "The Volatiles Investigating Polar Exploration Rover Payload," NASA Ames Research Center, Moffett Field, CA, 2020.

[50] P. N. Peplowski, R. C. Elphic, E. L. Fritzler, and J. T. Wilson, "Calibration of NASA's Neutron Spectrometer System (NSS) for landed measurements of hydrogen content of the lunar subsurface," *Nuclear Instruments and Methods in Physics Research Section A: Accelerators, Spectrometers, Detectors and Associated Equipment*, vol. 1049, p. 168063, 2023. DOI: 10.1016/j.nima.2023.168063.

[51] T. L. Roush, A. Colaprete, A. Cook, R. Bielawski, K. Ennico-Smith, et al., "The Volatiles Investigating Polar Exploration Rover (VIPER) Near Infrared Volatile Spectrometer System (NIRVSS)," NASA Ames Research Center, 2023.

[52] K. Zacny, P. Chu, V. Vendiola, K. Bywaters, S. Goldman, et al., "TRIDENT Drill for VIPER and PRIME1 Missions to the Moon – 2023 Update," *Honeybee Robotics*, 2023.

[53] C. Li, Z. Wei, W. Wen, X. Zeng, X. Gao, et al., "Overview of the Chang'e-4 Mission: Opening the Frontier of Scientific Exploration of the Lunar Far Side," *Space Science Reviews*, vol. 217, 2021. DOI: 10.1007/s11214-021-00793-z.

[54] NASA Space Science Coordination Archive, "NSSDCA/COSPAR ID: 2018-103A," NASA Goddard Space Flight Center, Accessed Jan. 1, 2025. [Online]. Available: https://nssdc.gsfc.nasa.gov/.

[55] Y. Jia, Y. Zou, J. Ping, C. Xue, J. Yan, and Y. Ning, "The scientific objectives and payloads of Chang'E−4 mission," *Planetary and Space Science*, vol. 162, 2018. DOI: 10.1016/j.pss.2018.02.011.

[56] G. Meng, Y. Z. Zhu, J. S. Ping, Q. Huang, Z. C. Cai, et al., "Landing Site Selection and Prospective Scientific Objectives of Von Kármán Crater within South Pole-Aitken Basin," *49th Lunar and Planetary Science Conference*, LPI Contribution No. 2083, 2018.

[57] J.-F. Yang, C. Li, B. Xue, P. Ruan, W. Gao, et al., “Panoramic camera on the Yutu lunar rover of the Chang’e-3 mission,” *Research in Astronomy and Astrophysics*, vol. 15, pp. 1867–1880, 2015. DOI: 10.1088/1674-4527/15/11/009.

[58] S. X. Shen, X. L. Hua, B. Zhou, Y. X. Li, W. Lu, et al., “Lunar Regolith Penetrating Radar on the Lander for Chang’E-5 Mission,” *IEEE International Conference on Ground Penetrating Radar (GPR)*, 2018. DOI: 10.1109/ICGPR.2018.8441614.

[59] Z. He, R. Xu, C. Li, G. Lv, L. Yuan, B. Wang, R. Shu, and J. Wang, “Visible and Near-Infrared Imaging Spectrometer (VNIS) for In-Situ Lunar Surface Measurements,” *Proceedings of the SPIE*, vol. 9639, id. 96391S, Oct. 2015. DOI: 10.1117/12.2194526. .

[60] H. Lin, Y. Lin, Y. Wei, R. Xu, Y. Liu, et al., “Estimation of Noise in the In Situ Hyperspectral Data Acquired by Chang’E-4 and Its Effects on Spectral Analysis of Regolith,” *Remote Sensing*, vol. 12, p. 1603, 2020. DOI: 10.3390/rs12101603.

[61] N. J. Kanu, E. Gupta, and G. C. Verma, “An insight into India's Moon mission – Chandrayaan-3: The first nation to land on the southernmost polar region of the Moon,” *Planetary and Space Science*, vol. 242, p. 105864, 2024. DOI: 10.1016/j.pss.2024.105864.

[62] K. Durga, M. Bhatt, A. Amitabh, G. Ambily, et al., “Contextual Characterisation Study of Chandrayaan-3 Primary Landing Site,” *Monthly Notices of the Royal Astronomical society: Letters*, vol. 526, 2023. DOI: 10.1093/mnrasl/slad106.

[63] K. B. Vijayan, A. Chavan, R. Aditi, U. Thahira, V. Rama Subramanian, et al., “Chandrayaan-3 landing site evolution by South Pole-Aitken basin and other impact craters,” *Icarus*, vol. 425, 2025. DOI: 10.1016/j.icarus.2025.116329.

[64] ISRO, “Chandrayaan-3 Details,” Aug. 5, 2023. [Online]. Available: https://www.isro.gov.in/. Accessed Dec. 3, 2024.

[65] A. S. Laxmi, R. V. L. N. Sridhar, A. Goswami, K. A. Lohar, et al., “Laser Induced Breakdown Spectroscope on Chandrayaan-2 Rover: A Miniaturized Mid-UV to Visible Active Spectrometer for Lunar Surface Chemistry Studies,” *Current Science*, vol. 118, pp. 573–581, 2020. DOI: 10.18520/cs/v118/i4/573-581.

[66] S. Munuswamy, S. Vadawale, A. Patel, N. P. S. Mithun, et al., “Alpha Particle X-ray Spectrometer onboard Chandrayaan-2 Rover,” *Current Science*, vol. 118, pp. 53–61, 2020. DOI: 10.18520/cs/v118/i1/53-61.

[67] T. S. Bálint, “Comparison of Power System Options Between Future Lunar and Mars Missions,” *International Lunar Conference*, 2005

[68] T. S. Bálint and J. F. Jordan, “RPS strategies to enable NASA’s next decade robotic Mars missions,” *Acta Astronautica*, vol. 60, no. 12, pp. 992–1001, 2007. DOI: 10.1016/j.actaastro.2006.12.003.

[69] J. R. Wertz and W. J. Larson (Eds.), *Space Mission Analysis and Design*, 3rd ed., Microcosm Press and Kluwer Academic Publishers, El Segundo, CA, USA, 1999.

[70] J. Li, A. Abuduwayiti, Y. Liu, Y. Zhuang, X. Yang, et al., “A Brief Review of High Efficiency III-V Solar Cells for Space Application,” *Frontiers in Physics*, vol. 8, 2021. DOI: 10.3389/fphy.2020.631925.

[71] C. Weisbin, J. H. Smith, T. Houten, R. Moeller, et al., "Technical Feasibility and Relative Productivity of Alternate NASA Robotic Missions to a Lunar Dark Crater," *IEEE Systems Journal*, vol. 2, pp. 120–128, 2008. DOI: 10.1109/JSYST.2007.908171.

[72] J. Biswas, P. Malzone, and F. Rößler, "Energy storage selection and operation for night-time survival of small lunar surface systems," *Acta Astronautica*, vol. 185, pp. 1–10, 2021. https://doi.org/10.1016/j.actaastro.2021.04.042.

[73] M.C. Smart, B.V. Ratnakumar, and S. Surampudi, "Electrolytes for low-temperature lithium batteries based on ternary mixtures of aliphatic carbonates," *Journal of The Electrochemical society*, vol. 146, no. 2, pp. 486–492, 1999. https://doi.org/10.1149/1.1391633.

[74] M.C. Smart, B.V. Ratnakumar, L. Whitcanack, S. Surampudi, J. Byers, and R. Marsh, "Performance characteristics of lithium-ion cells for NASA's Mars 2001 Lander application," *IEEE Aerospace and Electronic Systems Magazine*, vol. 14, no. 11, pp. 36–42, 1999. https://doi.org/10.1109/62.809207.

[75] M.C. Smart, B.V. Ratnakumar, L.D. Whitcanack, K.B. Chin, S. Surampudi, R. Gitzendanner, F. Puglia, and J. Byers, "Lithium-ion batteries for aerospace," *IEEE Aerospace and Electronic Systems Magazine*, vol. 19, no. 1, pp. 18–25, 2004. https://doi.org/10.1109/MAES.2004.1263988.

[76] J. Marquardt, J. Keller, G. Mills, and J. Schmidt, "An overview of Ball Aerospace cryogen storage and delivery systems," *IOP Conference Series: Materials Science and Engineering*, vol. 101, no. 1, p. 012086, 2015. https://doi.org/10.1088/1757-899X/101/1/012086.

[77] IntelligentEnergy, "IE-soar 650 - 800 - 2400W - Product Datasheets," 2020. [Online]. Available: https://www.intelligent-energy.com/our-products/uavs/. [Accessed: 4 January 2025].

[78] M.C. Guzik, R.P. Gilligan, P.J. Smith, and I.J. Jakupca, "Regenerative fuel cell-based energy storage systems for lunar surface exploration," *Survive the Lunar Night Workshop*, 2018. [Online]. Available: https://www.hou.usra.edu/meetings/survive thenight2018/pdf/7024.pdf.

[79] Vincent L. Pisacane, Spacecraft Systems Design and Engineering, Editor(s): Robert A. Meyers, Encyclopedia of Physical Science and Technology (Third Edition), Academic Press, 2003, Pages 463-483, ISBN 9780122274107, https://doi.org/10.1016/B0-12-227410-5/00888-7.

[80] Book Section,A Gary Gordon,Space Exploration: Mass Ratios for Different Missions,AIAA SPACE 2007 Conference & Exposition, 10.2514/6.2007-6278, https://arc.aiaa.org/doi/abs/10.2514/6.2007-6278

[81] A.G. Gordon, "Space Exploration: Mass Ratios for Different Missions," in *AIAA SPACE 2007 Conference & Exposition*, 2007, pp. 1–5. https://doi.org/10.2514/6.2007-6278.

[82] A. Engelbrecht, "Computational Intelligence: An Introduction", Wiley New York, 2007.

[83] B. S, S. S. Sathya, "A survey of bio inspired optimization algorithms", *International journal of soft computing and engineering*, vol. 2, no. 2, pp. 137-151, 2012.

[84] E. Elbeltagi, T. Hegazy, D. Grierson, “Comparison among five evolutionary-based optimization algorithms”, *Advanced Engineering Informatics*, vol. 19, no. 1, pp. 43-53, 2005.

[85] Π. Σ. Α. Γεωργιλάκης, «Εφαρμογή Γενετικών Αλγορίθμων στην Παραγωγή Ηλεκτρικής Ενέργειας», *Τεχν. Χρον. Επιστ. Εκδ. ΤΕΕ*, vol. 111, no. 1-2, pp. 41–50, 2004.

[86] H. Yang, D. Kong, Z. Yang, Y. Yang, D. Dong, and L. Zhang, “An improved particle swarm optimization algorithm,” *Applied Mathematics and Computation*, vol. 193, no. 1, pp. 231–239, 2007.

[87] X.S. Yang, “Optimization and Metaheuristic Algorithms in Engineering,” in *Metaheuristics in Water, Geotechnical and Transport Engineering*, 2013, pp. 1–23.

[88] F. Zhou and Z. Liao, “A particle swarm optimization algorithm,” *Applied Mechanics and Materials*, vols. 303–306, pp. 1369–1372, 2013.

[89] R.C. Eberhart and Y. Shi, “Particle swarm optimization: developments, applications and resources,” *Proceedings of the 2001 Congress on Evolutionary Computation*, vol. 1, pp. 81–86, 2001.

[90] PSO Tutorial, [Online]. Available: http://www.swarmintelligence.org/tutorials.php. [Accessed: 4 January 2025].

[91] Y. Zhang, S. Wang, and G. Ji, “A comprehensive survey on particle swarm optimization algorithm and its applications,” *Mathematical Problems in Engineering*, vol. 2015, pp. 1–38, 2015.

[92] W. Zhang, D. Ma, J. Wei, and H. Liang, “A parameter selection strategy for particle swarm optimization based on particle positions,” *Expert Systems with Applications*, vol. 41, no. 7, pp. 3576–3584, 2014.

[93] Q. Bai, “Analysis of particle swarm optimization algorithm,” *Computer and Information Science*, vol. 3, no. 1, pp. 180–184, 2010.

[94] R. C. Eberhart, Y. Shi, "Particle swarm optimization: developments, applications and resources," *Proceedings of the 2001 Congress on Evolutionary Computation*, vol. 1, pp. 81-86, 2001.

[95] A.J. Gemer, J.A. Cyrus, and J.B. Cyrus, “Lunar science mobility as a service: The Lunar Outpost Mobile Autonomous Prospecting Platform (MAPP) rover,” *Lunar Surface Science Workshop 2020 (LPI Contrib. No. 2241)*, Lunar Outpost, Inc., Golden, CO, USA, 2020.

[96] Lunar Outpost, “Lunar Outpost rovers,” [Online]. Available: https://www.lunaroutpost.com/rovers. [Accessed: 4 January 2025].

[97] X. Zeng et al., "An Inductive Power Transfer System for Lunar Rovers," IEEE 7th International Electrical and Energy Conference (CIEEC), Harbin, China, 2024, pp. 5148-5152, doi: 10.1109/CIEEC60922.2024.10583195.

[98] W.K. Hofstetter, S.B. Hong, J.A. Hoffman, and E.F. Crawley, “Analysis of architectures for long-range crewed Moon and Mars surface mobility,” *AIAA Space Conference*, 2008.

[99] W.J. Larson and L.K. Pranke (editors), *Human Spaceflight–Mission Analysis and Design*, Space Technology Series, McGraw-Hill, New York, 2000.

[100] J. Matijevic, “Sojourner: The Mars Pathfinder Microrover Flight Experiment,” *JPL Open Repository*, Santa Monica, CA, USA, 1997. Available: https://hdl.handle.net/2014/21704.

[101] S. Oleson, E. Turnbull, P. Schmitz, et al., “Use of a dynamic radioisotope power source for a long duration lunar science rover,” *Nuclear and Emerging Technologies for Space*, American Nuclear society, Cleveland, OH, May 8–12, 2022.

[102] A. Della Torre, A.E. Finzi, G. Genta, et al., “AMALIA mission lunar rover: The conceptual design of the team ITALIA rover, candidate for the Google Lunar X Prize Challenge,” *Acta Astronautica*, vol. 67, no. 7–8, pp. 961–978, 2010. https://doi.org/10.1016/j.actaastro.2010.05.023.

[103] NASA, “Moon Map - Lunar South Pole,” Available: https://trek.nasa.gov/moon/.

[104] J. Silva-Rodriguez and X. Li, “Solar Power Generation Profile Estimation for Lunar Surface Solar PV Systems,” arXiv preprint, 2024. Available: https://arxiv.org/abs/2402.14783.

[105] P. Gläser, A. Sanin, J. P. Williams, I. Mitrofanov, and J. Oberst, “Temperatures Near the Lunar Poles and Their Correlation With Hydrogen Predicted by LEND,” *Journal of Geophysical Research: Planets*, vol. 126, no. 9, 2021.

[106] W. Farrell, J. Halekas, M. Horanyi, R. Killen, C. Grava, J. Szalay, M. Benna, P. Clark, M. Collier, A. Colaprete, J. Deca, R. Elphic, S. Fatemi, Y. Futaana, M. Holmström, D. Hurley, G. Kramer, P. Mahaffy, M. Nishino, and S. Yokota, “The Dust, Atmosphere, and Plasma at the Moon,” *Reviews in Mineralogy and Geochemistry*, vol. 89, pp. 563–609, 2023. DOI: 10.2138/rmg.2023.89.13.

[107] SpectroLab, "32.2% XTE-SF (Standard Fluence) Space Qualified Triple Junction Solar Cell," Datasheet, *XTE-SF Data Sheet*, July 27, 2022. Available: www.spectrolab.com.

[108] SpaceTech, "Datasheet, Solar Arrays," TI-DS-03-20229-191_Solar-Arrays, [Online]. Available: www.spacetech-i.com. [Accessed: 23 January 2025].

[109] Sparkwing, "Datasheet," SSAP-TN-ADSN-0011 i2, [Online]. Available: www.sparkwing.space. [Accessed: 23 January 2025].

[110] E. Lorenzo, Solar Electricity—Engineering of Photovoltaic Systems, 1st ed., Sevilla, Spain: Progensa, 1994.

[111] EaglePicher, "43 Ah high-energy, long-cycle-life, low-maintenance Li-Ion cells," Datasheet, *LP33450 43 Ah Space Cell*, February 2023. Available: https://www.eaglepicher.com/.

[112] ACT, "Lunar QuickMap," [Online]. Available: https://quickmap.lroc.asu.edu/. [Accessed: Jan. 7, 2025].

[113] Man, K. & Ting, T. & Krilavičius, Tomas & Wan, Kaiyu & Chen, C. & Chang, J. & Poon, Benedict Sheung Hung. (2012). Towards a hybrid approach to SoC estimation for a smart Battery Management System (BMS) and battery supported Cyber-Physical Systems (CPS). *2012 2nd Baltic Congress on Future Internet Communications*, BCFIC 2012. 10.1109/BCFIC.2012.6217989.

[114] D. B. J. Bussey, J. A. McGovern, P. D. Spudis, et al., “Illumination conditions of the south pole of the Moon derived using Kaguya topography,” *Icarus*, vol. 208, no. 2, pp. 558-564, 2010. DOI: 10.1016/j.icarus.2010.03.028.

[115] NASA Jet Propulsion Laboratory (JPL), "Moon Trek," [Online]. Available: https://trek.nasa.gov/. [Accessed: Jan. 7, 2025].

[116] M. Shirley, E. Balaban, A. Colaprete, R. C. Elphic, H. Sanchez, L. Falcone, R. Beyer, S. Banerjee, and K. Bradner, "VIPER Traverse Planning," *3rd Lunar and Planetary Science Conference*, NASA Ames Research Center, Moffet Field, CA, 2022.

[117] S. Oleson, E. Turnbull, P. Schmitz, et al., "Use of a dynamic radioisotope power source for a long duration lunar science rover," *Nuclear and Emerging Technologies for Space*, American Nuclear Society, Cleveland, OH, May 8–12, 2022.